Thermal and Current-Induced Magnetization Switching of Fe/W(110) Nanoislands Investigated by Spin-Polarized Scanning Tunneling Microscopy

Dissertation
zur Erlangung des Doktorgrades
am Department Physik
der Universität Hamburg

vorgelegt von
Dipl.-Phys. Stefan Krause
aus Hamburg

Hamburg
2008

Gutachter der Dissertation:
    Prof. Dr. R. Wiesendanger
    Prof. Dr. R. L. Johnson

Gutachter der Disputation:
    Prof. Dr. R. Wiesendanger
    Prof. Dr. H. P. Oepen

Datum der Disputation:
    18.12.2008

Vorsitzender des Prüfungsausschusses:
    Prof. Dr. J. Bartels

Vorsitzender des Promotionsausschusses:
    Prof. Dr. R. Klanner

Dekan der MIN-Fakultät:
    Prof. Dr. A. Frühwald

Abstract

Future high-density magnetic data storage demands both, a detailed understanding of the magnetic reversal processes as well as a basic concept of local magnetization switching by the injection of a spin-polarized current.

Within this work, the intrinsic thermal switching behavior of magnetic iron nanoislands with uniaxial anisotropy is investigated by means of spin-polarized scanning tunneling microscopy (SP-STM). The islands typically contain about 100 iron atoms on a clean tungsten(110) substrate. The experiments reveal that magnetization reversal takes place via the nucleation and diffusion of a domain wall. Atoms on the rim of the islands have a significantly higher anisotropy energy than center atoms.

The thermal switching behavior of individual nanoislands has been influenced using high spin-polarized tunnel currents in the µA range. Analysis of the thermal switching behavior as a function of the applied tunnel current shows an increased lifetime asymmetry of the two otherwise degenerate magnetic orientations with increasing tunnel current. Spatially-resolved data permit the three fundamental contributions involved in magnetization switching to be identified and quantified, i.e. pure spin torque, Joule heating of the island by the tunnel current, and Oersted field effects. The magnetization of quasistable islands has been reversed using manually triggered high tunnel current pulses.

The experiments demonstrate nanoscale magnetic manipulation using an SP-STM probe tip. Combined current-induced magnetization reversal across a vacuum barrier and the ultimate resolution of SP-STM provide an improved understanding of the magnetization switching mechanisms.

Inhaltsangabe

Eine grundlegende Voraussetzung für die Entwicklung zukünftiger Datenspeichertechnologien ist das detaillierte Verständnis des thermischen und spinstrominduzierten Schaltens von nanoskaligen Magneten.

In dieser Arbeit wird das thermische Schaltverhalten von magnetischen Nanoinseln uniaxialer Anisotropie mittels spinpolarisierter Rastertunnelmikroskopie (Spin-Polarized Scanning Tunneling Microscopy, SP-STM) untersucht. Dabei besteht jede der Nanoinseln aus ca. 100 Eisenatomen, die sich auf einer reinen Wolfram(110)-Oberfläche befinden. Die hier vorgestellten Experimente zeigen, dass die thermisch aktivierte Magnetisierungsumkehr durch die Nukleation und anschließende Diffusion einer Domänenwand innerhalb einer Nanoinsel hervorgerufen wird. Atome am Rand der Insel haben dabei eine im Vergleich zum Zentrum deutlich erhöhte magnetische Anisotropie.

Das thermische Schaltverhalten der Magnetisierung einzelner Nanoinseln wird mittels hoher spin-polarisierter Tunnelströme im µA-Bereich gezielt beeinflusst. Während bei niedrigem Tunnelstrom beide Magnetisierungszustände die gleiche mittlere Lebenszeit zeigen, bildet sich mit zunehmendem Tunnelstrom eine Asymmetrie der Lebenszeiten aus. Die Kombination mit ortsaufgelösten Daten ermöglicht dabei die Trenung und quantitative Bestimmung von drei fundamentalen Effekten, die zum strominduzierten Schalten beitragen: Das reine Spinstromschalten durch Spinübertrag, das Joule'sches Aufheizen der Nanoinsel durch den Tunnelstrom, und Einflüsse des Oersted-Feldes. In einem Temperaturbereich, in dem die Magnetisierung der Nanoinseln quasistabil ist, werden manuell ausgelöste spin-polarisierte Strompulse genutzt, um die Magnetisierung einer Nanoinsel zu schalten.

In diesen Experimenten wird die magnetische Manipulation nanoskaliger Objekte mittels SP-STM demonstriert. Das strominduzierte Schalten über eine Vakuumbarriere in Kombination mit der hohen Ortsauflösung von SP-STM ermöglicht es dabei, ein vertieftes Verständnis der Prozesse zu gewinnen, die zum Schalten der Magnetisierung beitragen.

Contents

Chapter 1

Introduction

Information storage on individual atoms still remains a dream for our information society. Today's commercial applications require magnetic storage devices with bit densities unimaginable over 50 years ago, and this development still continues. Advances in technology led to smaller and cheaper computers using data storage technologies at much higher density. In today's commercial hard disks, one bit has the size of about $3600\,\text{nm}^2$, thereby allowing the storage of more than one TeraByte (10^6 MB) in a conventional 3.5" slot device.

The discovery of the *giant magnetoresistance* (GMR) effect in 1987 enabled to decrease the bit sizes down to today's dimensions. In 2007, Peter Grünberg and Albert Fert received the Nobel prize for their discovery of the GMR effect. When passed by a current, the conductance of a device consisting of two magnetic layers separated by a non-magnetic layer depends on the relative magnetization directions of the two magnets. To readout the magnetization at high lateral resolution, one magnetization is fixed whereas the other is affected by the strayfield of the sample. Depending on the magnetization of the sample, the conductance of the device is high or low, and this is decoded to the bit state "1" or "0".

One technique did not change over the past decades: Magnetization reversal is still based on the application of an external magnetic field that is generated by the Oersted field of an electric current. But the electrons that contribute to the current are not only charge carriers—they also have a spin and therefore a magnetic moment. Inside a non-magnetic metal, the spin of the electrons has no preferential orientation and therefore cancels on average. In 1996, Slonczewski[1] and Berger[2] predicted that the current flowing through magnetic multilayers could have a more direct effect on the magnetic state than the Oersted field: When the current passes through a ferromagnet, it becomes partially spin-polarized, aligning the electron spins along the magnetization direction of the ferromagnet. The current carries a net angular momentum, and if the thickness of a non-magnetic layer between two ferromagnets is small enough, the current can interact with the magnetization of the subsequent magnetic layer. The spin current exerts
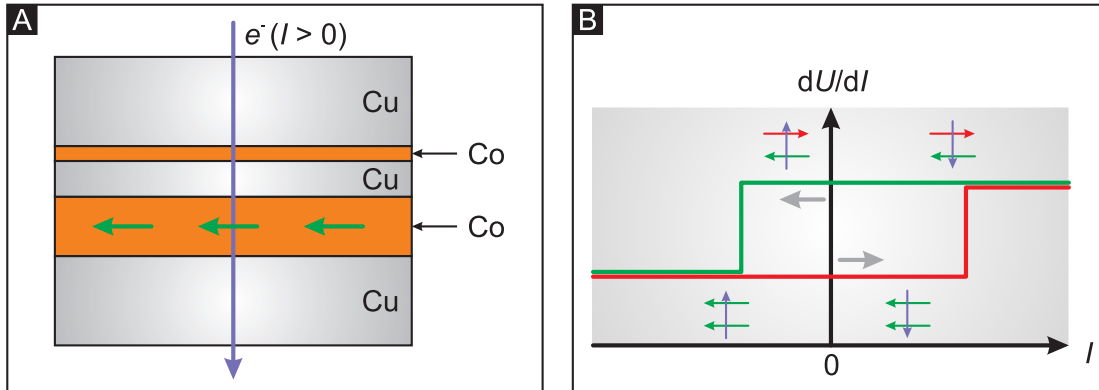
Figure 1.1: (**A**) Schematic of a pillar device used in the experiments by Katine *et al.* with two Co layers separated by a thin Cu layer [3]. (**B**) Ideal dU/dI signal of differential resistance of a pillar device exhibiting hysteretic jumps as the current is swept. The current sweeps begin at zero; red and green lines indicate increasing and decreasing current, respectively. Depending on the current direction, the magnetization of the thin Co layer switches to the parallel or antiparallel configuration.

a spin transfer torque on the magnetizations inside the multilayer device, and for large enough currents this torque leads to magnetic precession or even reversal. This is the basic concept of current-induced magnetization switching.

Since this prediction, many experiments have been performed that investigate spin transfer induced magnetization dynamics [3–17], using different device geometries like mechanical or lithographically fabricated point contacts, nanopillars or tunnel junctions. The first clear experimental verification of the spin-torque driven magnetization reversal has been published by Katine *et al.* [3]. They investigated the current-driven magnetization reversal in pillars containing two Co layers of different thickness separated by a Cu spacer, as depicted in Fig. 1.1A. When applying a low magnetic field to fix the magnetization of the thick layer in a one-domain state, spin-polarized electrons flowing from the thick to the thin layer can switch the magnetic moment of the thin layer parallel to that of the thick layer, while a reversed current leads to a switching into the antiparallel configuration, as illustrated in Fig. 1.1B. In general, the switching process can be described within a simple macro-spin model where all the magnetic moments within a particle rotate coherently. However, it was found that in some cases this model fails and has to be extended to the combined action of spin injection and the Oersted field that is induced by the current [18].

Although the lithographic fabrication of layered systems has been significantly improved, it is very hard to realize multilayer devices with atomically sharp interfaces without any intermixing of the different materials. Consequently, it is not clear where *exactly* the current flows that interacts with the magnetic electrodes, and due to the structure of the devices the role of tunnel barrier imperfections in-

side a magnetic tunnel junction is basically unknown. Furthermore, the influence of Oersted field effects on magnetic switching processes is still an open question. To exclude any interfacial imperfections, leakage channels or intermixings, one could think of a magnetic tunnel junction where the magnetic electrodes are separated by vacuum. However, this kind of magnetic tunnel junctions has not yet been realized for experiments using high spin-polarized currents. Consequently, it remains an open question if current-induced magnetization switching across a vacuum barrier is possible.

Spin-polarized scanning tunneling microscopy (SP-STM) opens the perspective for a new class of experiments that provide a deeper insight into the microscopic processes due to spin torque effects. SP-STM is a powerful tool to image the magnetic structure of surfaces at a lateral resolution down to the atomic scale [19, 20]. Here, a magnetic tip approaches a magnetic sample. When a bias voltage is applied to the electrodes, a spin-polarized tunnel current starts to flow between tip and sample at small distances. In this configuration the spin-polarized tunnel conductance between a magnetic tip and a magnetic sample is measured to determine the magnetic state of the sample. Besides, SP-STM realizes the model of a "perfect" magnetic tunnel junction, with vacuum serving as the barrier separating the two magnetic electrodes, namely the tip and the sample. Since the tunnel current exponentially depends on the distance between tip and sample, the same tip that determines the magnetic state at low current may be used for the manipulation of magnetism when tunneling at decreased distance, acting as a source of high spin-polarized currents. The torque exerted by the electrons switches the magnetization in a direction to align it parallel to the spin-polarization of the current. However, whereas SP-STM already provides established reading capabilities at ultimate resolution, it has not yet been shown experimentally that SP-STM may also be used for applications to manipulate magnetism at that scale.

Using devices that provide reading *and* writing capabilities at ultimate lateral resolution could lead to a further increase of data density in storage media. However, with decreasing particle size the so-called superparamagnetic limit will be reached in the near future. For particles having a size less than a critical size, thermally induced magnetization reversal processes can occur that destroy the information stored in the particle [21]. In theoretical elaborations by Néel [22] and Brown [23] the switching rate has been determined under the assumption of the magnetization being coherent at any time—even during the switching process. In this model the switching rate is exponentially dependent on the temperature and the size of the particle. A detailed understanding of the microscopic processes involved in the switching behavior could help to engineer materials that exhibit a stable magnetization at small sizes and therefore may enable the realization of new types of ultra-high data density storage devices.

Due to the limited lateral sensitivity, most of the experiments in the past have been performed on ensembles of assumedly identical objects, and not on a single

particle. Consequently, effects that are related to the shape or the size of individual particles are not detectable in the averaged signal. Only recently the switching behavior of individual nanoparticles has been investigated experimentally [24–27]. It has been shown that for compact particles the Néel-Brown theory applies very well, while for particles with a distinct elongation a transition from a coherent rotation of all magnetic moments to the nucleation and propagation of a domain wall occurs.

For the experiments that have been performed within this work, ferromagnetic nanoislands with uniaxial anisotropy and consisting of about 100 atoms on a W(110) substrate were prepared that switch their magnetization due to thermal activation. To get a deeper understanding of the switching processes involved in magnetization reversal, the switching behavior of the nanoislands as a function of temperature and size has been investigated systematically. After that, the possibility of current-induced magnetization switching using SP-STM has been tested. Before trying to reverse the magnetization of stable nanoislands, experiments on the current-induced magnetization switching have been performed using a sample system of thermally switching nanoislands. In contrast to a stable magnetic particle, where a minimum threshold current would have to be applied to excite a magnetic reversal, even small spin torque effects should already significantly influence the switching behavior of nanoislands that reverse their magnetization due to thermal activation, and these effects should lead to a modification of the state-dependent mean lifetime between two switching events. Furthermore, the high spatial resolution of current-induced magnetization switching with SP-STM could provide new insight into the details of the processes involved in the magnetization reversal that are inaccessible in experiments with buried interfaces.

In this thesis the switching behavior of magnetic nanoparticles and the question whether SP-STM could also serve as a tool to manipulate the magnetism of nanostructures at the atomic scale are investigated. After introducing the theory of current-induced magnetization switching in Ch. 2, the working principles of STM and SP-STM are covered in Ch. 3, followed by the experimental setup and the preparation of tips and samples in Ch. 4. The results of the investigations of thermally switching magnetic nanoislands are presented in Ch. 5, whereas the results of the experiments regarding the current-induced magnetization switching with SP-STM using are presented in Ch. 6 for the system of thermally switching nanoislands and in Ch. 7 for quasistable nanoislands. Finally, a summary and outlook are given in Ch. 8.

Chapter 2

# Theory of Current-Induced Magnetization Switching

The magnetization orientation in a metallic ferromagnetic system affects the electron transport properties of the system. For example, the resistance of a magnetic layer depends on the angle θ between its magnetization direction and the direction of the flowing current. An angle of $\theta = 0°$ or $\theta = 180°$ results in maximum resistance, and this effect is called the *anisotropic magnetoresistance effect* (AMR). If two magnetic layers are separated by a nonmagnetic metallic thin film, the resistance of a current flowing through this device depends on the relative magnetic orientation of the two layers. The change in resistance is known as the *giant magnetoresistance effect* (GMR) [28, 29]. If the spacer is an insulating layer or vacuum, the effect is called *tunneling magnetoresistance* (TMR) [30].

Since a magnetic system affects a current, the reversed effect may also occur: a spin-polarized current injected into a magnetic material can influence its magnetization. Spin-transfer induced magnetization reversal is a relatively new phenomenon and has been observed in studies on lithographically fabricated layered systems with structures typically smaller than $0.1\,\mu m$ in size. The spin torque is driven by the exchange of angular momentum between a spin-polarized current and the magnetization.

In the following sections, the basic theory of spin filtering and spin torque generation are described for all-metallic devices and systems where an insulating barrier separates two ferromagnets.

2.1   Spin filtering and spin torque generation

Whenever an electron flows through a conducting magnetic material, the spin of the electron and the magnetic moments affect each other due to exchange interaction, resulting in an effective torque due to conservation of angular momentum. Both the electron spin and the magnet experience this torque: Whereas an elec-
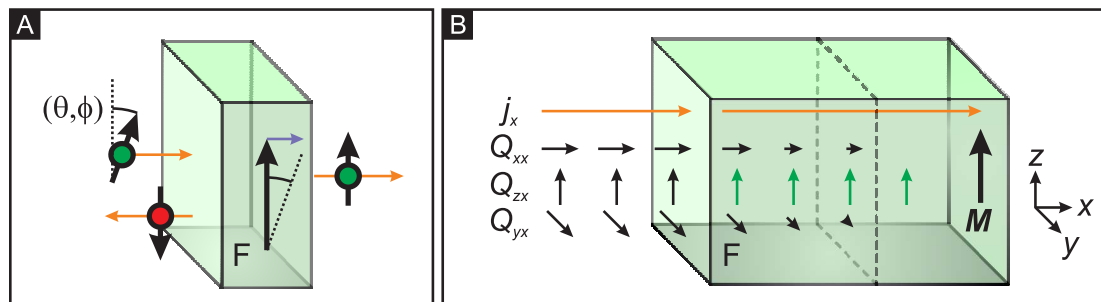
Figure 2.1: Principles of spin transfer. (**A**) Details of the spin-filtering process. An electron current with the spins aligned parallel to the magnetization of the layer is generated from the passing electrons, whereas the spin of reflected eletrons is antiparallel with respect to the magnetization of the layer. (**B**) Current density (j_x) and spin current densities (Q_{xx},Q_{yx},Q_{zx}) of the electron flow. Due to the spin-filtering process at the interface, only the component Q_{zx} parallel to $\vec{M}$ is transmitted.

tron gets spin-filtered when passing the magnet, the response of the magnet on the electron flow depends on the current density and spin-polarization. For a sufficiently high spin-polarized current the spin-torque acting on the magnet is high enough to reverse its magnetization.

Principle of spin filtering and spin torque

In the following the basic principle of polarization and spin-torque generation for an all-metallic device will be summarized, based on a publication by Stiles and Zangwill[31]. The detailed polarization process is sketched in Fig. 2.1A. An electron is considered moving along the x direction towards a ferromagnet with magnetization $\vec{M}$, with the electron spin pointing in the direction (θ, ϕ) with respect to $\vec{M}$. The current density is given by j_x, whereas the spin current density is described by Q_{xx}, Q_{yx} and Q_{zx}, as depicted in Fig. 2.1B. The left index of Q is in spin space, denoting the respective component along the x, y and z direction, and the right index is in real space. Q_{zx} is assumed to be parallel to the magnetization of the magnet.

The state of the incoming electron can be described by a wave function ψ_{in}, combined of orthogonal spin-up ($\uparrow$) and spin-down ($\downarrow$) components:

$$\psi_{\text{in}} = \left[\cos\frac{\theta}{2}e^{-i\frac{\phi}{2}}\left|\uparrow\right\rangle + \sin\frac{\theta}{2}e^{i\frac{\phi}{2}}\left|\downarrow\right\rangle\right] e^{ik_x x}e^{i\vec{q}\cdot\vec{R}}. \tag{2.1}$$

Here, the spatial variable is $\vec{r} = (x, \vec{R})$, and the wave vector is given by $\vec{k} = (k_x, \vec{q})$. $\vec{R}$ and $\vec{q}$ are two-dimensional vectors and denote the components in the plane of the interface. The real space angle θ is transformed to $\theta/2$ when changing into spin space: In real space, spin-up and spin-down states are enclosing an angle of

180°. In spin space, spin-up and spin-down states are orthogonal and consequently enclose an angle of 90°. Hence, θ has to be transformed to $\theta' = \frac{\theta}{2}$ in spin space.

At the interface to the magnet, the electron will be either reflected or transmitted. Solving the Schrödinger equation separately for the spin-up and spin-down components leads to the complete scattered state, again written as a combination of spin-up and spin-down wave functions, $\psi_{\text{scatter}} = \psi_\uparrow + \psi_\downarrow$, with

$$
\psi_\uparrow = \cos\frac{\theta}{2}\, \mathrm{e}^{-\mathrm{i}\frac{\phi}{2}}\, \mathrm{e}^{\mathrm{i}\vec{q}\cdot\vec{R}}\, |\uparrow\rangle
\begin{cases}
\left(\mathrm{e}^{\mathrm{i}k_x x} + R_\uparrow \mathrm{e}^{-\mathrm{i}k_x x}\right) & ; \quad x < 0, \\
T_\uparrow \mathrm{e}^{\mathrm{i}k_x^\uparrow x} & ; \quad x > 0,
\end{cases}
\tag{2.2}
$$

$$
\psi_\downarrow = \sin\frac{\theta}{2}\, \mathrm{e}^{+\mathrm{i}\frac{\phi}{2}}\, \mathrm{e}^{\mathrm{i}\vec{q}\cdot\vec{R}}\, |\downarrow\rangle
\begin{cases}
\left(\mathrm{e}^{\mathrm{i}k_x x} + R_\downarrow \mathrm{e}^{-\mathrm{i}k_x x}\right) & ; \quad x < 0, \\
T_\downarrow \mathrm{e}^{\mathrm{i}k_x^\downarrow x} & ; \quad x > 0.
\end{cases}
\tag{2.3}
$$

Here, $R_\uparrow, R_\downarrow, T_\uparrow,$ and $T_\downarrow$ are the reflection and transmission amplitudes for up and down spin electrons. For $x > 0$, the wave vectors $k_x^\uparrow$ and $k_x^\downarrow$ differ due to band splitting effects inside the ferromagnet. Note that the wave vector component parallel to the surface is conserved, as expressed by the common factor $\mathrm{e}^{\mathrm{i}\vec{q}\cdot\vec{R}}$.

The magnitude of the potential step at the interface determines the transmission (T_σ) and reflection (R_σ) amplitudes ($\sigma = \uparrow, \downarrow$). Electrons in front of the magnet are parametrized by k, whereas minority and majority electrons inside the ferromagnet have different wave vectors $k^\uparrow$ and $k^\downarrow < k^\uparrow$. The transmission amplitudes can be derived by the usual quantum mechanical matching conditions:

$$
T_\sigma(q) = \frac{2k_x(q)}{k_x(q) + k_x^\sigma(q)},
\tag{2.4}
$$

where $k_x(q) = \sqrt{k^2 - q^2}$ and $k_x^\sigma = \sqrt{(k^\sigma)^2 - q^2}$ denote the respective x component of the wave vector perpendicular to the interface plane, and $q = |\vec{q}|$.

Whereas the transition amplitude $T_\sigma(q)$ is real, the reflection amplitudes $R_\sigma(q)$ can be real or complex, depending on the magnitude q of the wave vector in the plane of the interface:

$$
R_\sigma(q) = \frac{k_x(q) - k_x^\sigma(q)}{k_x(q) + k_x^\sigma(q)}; \quad q^2 \le (k^\sigma)^2,
\tag{2.5}
$$

$$
R_\sigma(q) = \frac{k_x(q) - \mathrm{i}\kappa_x^\sigma(q)}{k_x(q) + \mathrm{i}\kappa_x^\sigma(q)}; \quad q^2 > (k^\sigma)^2,
\tag{2.6}
$$

where $\kappa^\sigma(q) = \sqrt{q^2 - (k^\sigma)^2}$.

The current densities j_x and spin current densities Q for the incident, reflected and transmitted states are listed in Tab. 2.1. Here, $v_x = \frac{\hbar k_x}{m_\mathrm{e}}$ denotes the velocity of the electron, with m_e being its effective mass.

When the electron flows into the magnet, the (initally equal) magnitudes of its spin component wave vectors are modified from k_x to $k^\downarrow$ and $k^\uparrow$ with $k^\downarrow < k^\uparrow$. As

	incident	reflected
j_x	v_x	$-|v_x|\left(\cos^2\frac{\theta}{2}|R_\uparrow|^2 + \sin^2\frac{\theta}{2}|R_\downarrow|^2\right)$
Q_{zx}	$\frac{\hbar}{2}v_x\cos\theta$	$-\frac{\hbar}{2}|v_x|\left(\cos^2\frac{\theta}{2}|R_\uparrow|^2 - \sin^2\frac{\theta}{2}|R_\downarrow|^2\right)$
Q_{xx}	$\frac{\hbar}{2}v_x\sin\theta\cos\phi$	$-\frac{\hbar}{4}|v_x|\sin\theta\,\mathrm{Re}\left[R_\uparrow^* R_\downarrow \mathrm{e}^{\mathrm{i}\phi}\right]$
Q_{yx}	$\frac{\hbar}{2}v_x\sin\theta\sin\phi$	$-\frac{\hbar}{4}|v_x|\sin\theta\,\mathrm{Im}\left[R_\uparrow^* R_\downarrow \mathrm{e}^{\mathrm{i}\phi}\right]$
		transmitted
j_x		$v_x^\uparrow\cos^2\frac{\theta}{2}|T_\uparrow|^2 + v_x^\downarrow\sin^2\frac{\theta}{2}|T_\downarrow|^2$
Q_{zx}		$\frac{\hbar}{2}v_x^\uparrow\cos^2\frac{\theta}{2}|T_\uparrow|^2 - \frac{\hbar}{2}v_x^\downarrow\sin^2\frac{\theta}{2}|T_\downarrow|^2$
Q_{xx}		$\frac{\hbar}{4}\frac{v_x^\uparrow+v_x^\downarrow}{2}\sin\theta\,\mathrm{Re}\left[T_\uparrow^* T_\downarrow \mathrm{e}^{\mathrm{i}\phi}\mathrm{e}^{\mathrm{i}(k_x^\downarrow-k_x^\uparrow)x}\right]$
Q_{yx}		$\frac{\hbar}{4}\frac{v_x^\uparrow+v_x^\downarrow}{2}\sin\theta\,\mathrm{Im}\left[T_\uparrow^* T_\downarrow \mathrm{e}^{\mathrm{i}\phi}\mathrm{e}^{\mathrm{i}(k_x^\downarrow-k_x^\uparrow)x}\right]$

Table 2.1: Current densities for incident, reflected and transmitted states of a free electron with spin initially pointed in the direction (θ,ϕ) when interacting with a ferromagnetic interface. The electron propagates along the x direction (results taken from [31]).

stated above, the incident electron can be described as a superposition of orthogonal spin-up and spin-down components. The scattered state is a combination of the scattered spin components, and each spin component is separately affected by the interface. Since both the reflection and the transmission amplitudes are spin-dependent, the spin-up and spin-down components of the scattered state differ from one another. Consequently, this results in different transverse spin components and therefore in spin-filtering because of a discontinuity in the transverse spin current.

The discontinuity of the transverse spin current gives rise to a spin torque acting on the magnet. Imagine a pillbox that includes the interface of area A between the non-magnetic metal and the magnet. The current is flowing along the $\hat{x}$ direction normal to the interface. The incoming spin flux $\vec{Q}_\mathrm{in} \cdot A\hat{x}$ minus the outgoing spin flux $\vec{Q}_\mathrm{tr} \cdot A\hat{x} + \vec{Q}_\mathrm{ref} \cdot (-A\hat{x})$ equals the torque $\vec{N}$ on the magnetization inside the pillbox. Obviously, $\vec{N}$ is proportional to the transverse part of $\vec{Q}_\mathrm{in}$ since the discontinuity of the transverse spin current is proportional to the transverse part of $\vec{Q}_\mathrm{in}$. Consequently, the transverse spin component of a passing electron is completely absorbed by the magnet within a few lattice constants. The spin of reflected electrons are aligned antiparallel to the magnetization $\vec{M}$ of the ferromagnet, whereas the spin of the transmitted electrons is aligned parallel to $\vec{M}$, as can be seen from Tab. 2.1.

To summarize, the angular momentum of the incoming electrons is imparted to the ferromagnet moments and exerts a torque on them. Consequently, a spin
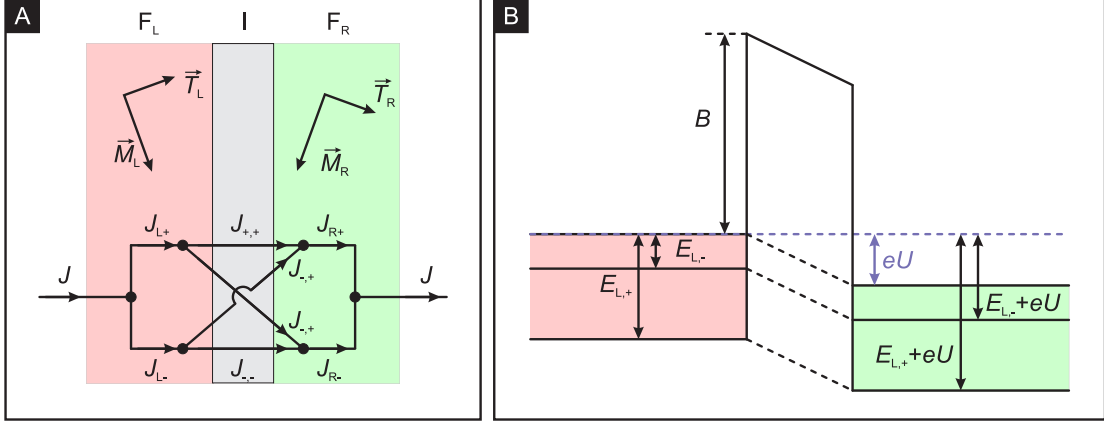
Figure 2.2: (**A**) Scheme of a magnetic tunnel junction. An insulating barrier (I) separates two ferromagnets (F_L,F_R). An equivalent circuit for spin-channel currents is shown in the bottom. (**C**) Schematic junction potential for finite bias voltage U. The blue dotted line indicates the energy of most of the tunneling electrons.

current with polarization parallel to the magnetization of the ferromagnet is generated from the passing electrons, whereas reflected electrons are polarized antiparallel. The spin torque is in the direction to align the magnetization of the ferromagnet with the polarization of the incident spin current.

Spin torque in magnetic tunnel junctions

Slonczewski [32, 33] treated spin torque generation in a magnetic tunnel junctions from a theoretical point of view. His basic ideas are summarized in the following.

Consider a device consisting of an insulating barrier separating two ferromagnetic electrodes, as depicted in Fig. 2.2A. The left and the right electrodes have magnetizations $\vec{M}_{L,R}$ pointing along the respective unit vectors $\vec{l}$ and $\vec{r}$. The total current density $J = J_0[1 + \iota \cos\theta]$ passes through the device, with J_0 being the unpolarized spin current and θ the angle between the magnetic moments of the left and right electrode, and ι is a dimensionless coefficient of magnetoconduction related to the polarization of each magnet. The magnetic tunnel junction can be described by an equivalent circuit for spin-channel currents where the incoming current J separates into J_{L+},J_{L-} in the left magnet and J_{R+},J_{R-} in the right magnet. Inside the tunneling barrier, elastic channels (with conserved spin, $J_{+,+}$, $J_{-,-}$) as well as inelastic channels (including spin excitations, $J_{+,-}$, $J_{-,+}$) contribute to the tunnel current. In the absence of an external bias voltage, the spin torque vector $\vec{T}_R$ induced on the right ferromagnet due to exchange coupling is given by

$$\vec{T}_R = \frac{\hbar}{2e} \tau_R \cdot J_0 \, \vec{r} \times (\vec{l} \times \vec{r}), \tag{2.7}$$

where the torque coefficient of the right electrode τ_R equals the tunneling polarization parameter P_L of the left electrode. P_i ($i =$L,R) of each electrode depends on the spin-dependent state densities $\Omega_{i,\sigma}$ at the Fermi energy: $P_i = \frac{\Omega_{i,+}-\Omega_{i,-}}{\Omega_{i,+}+\Omega_{i,-}}$. This expression for $\vec{T}_\mathrm{R}$ is only applicable if the inelastic channels of the tunneling process $J_{+,-}$, $J_{-,+}$ can be separated into left- and right-dependent factors. In analogy, the spin torque vector acting on the left magnet is given by

$$\vec{T}_\mathrm{L} = \frac{\hbar}{2e}\tau_\mathrm{L} \cdot J_0 \; \vec{l} \times (\vec{r} \times \vec{l})\,, \tag{2.8}$$

with $\tau_\mathrm{L} = P_\mathrm{R}$ being the torque coefficient of the left electrode. The respective wave vectors $k_{\mathrm{i},\sigma}$ inside the magnets and κ inside the tunnel barrier are given by

$$k_{i,\sigma}^2 = \frac{2m_\mathrm{e}}{\hbar^2}E_{i,\sigma} \quad \text{and} \quad \kappa^2 = \frac{2m_\mathrm{e}}{\hbar^2}B\,. \tag{2.9}$$

Here, $E_{i,\sigma}$ is the kinetic energy at the Fermi level and B is the barrier potential measured from the Fermi level (m_e denotes the electron mass).

The tunneling polarization parameter is then given by

$$P_i = \frac{k_{i,+} - k_{i,-}}{k_{i,+} + k_{i,-}} \cdot \frac{\kappa^2 - k_{i,+}k_{i,-}}{\kappa^2 - k_{i,+}k_{i,-}}\,. \tag{2.10}$$

When applying a finite bias voltage U to the right ferromagnet and neglecting the slope of the barrier potential, the respective wave vectors are modified to (see Fig. 2.2B):

$$k_{\mathrm{R},\sigma}^2 = \frac{2m_\mathrm{e}}{\hbar^2}(E_{\mathrm{R},\sigma} + eU) \quad \text{and} \quad \kappa^2 = \frac{2m_\mathrm{e}}{\hbar^2}(B - eU)\,. \tag{2.11}$$

Considering a symmetric tunnel junction with the polarization $P_\mathrm{L} = P_\mathrm{R}$ in the absence of bias voltage, the respective spin torque coefficients $\tau_{\mathrm{L,R}}$ can be determined as a function of bias voltage U. It turns out $\tau_{\mathrm{L,R}}(U)$ are not symmetric with respect to $U = 0\,\mathrm{V}$, which can be attributed to the nonohmic resistance of a tunneling barrier (in contrast to a metal junction).

2.2   Magnetization reversal due to spin-torque effects

An all-metal device for current-induced magnetization switching is shown in Fig. 2.3. A nonmagnetic spacer separates a thick ferromagnet (which serves as a spin-filter) from a thinner ferromagnet with antiparallel (A) or parallel (B) magnetization.

As shown in Fig. 2.3A, an unpolarized current is injected into the device from the left and gets spin-polarized when passing through the thick ferromagnetic layer. As long as the thickness of the nonmagnetic spacer is thinner than the
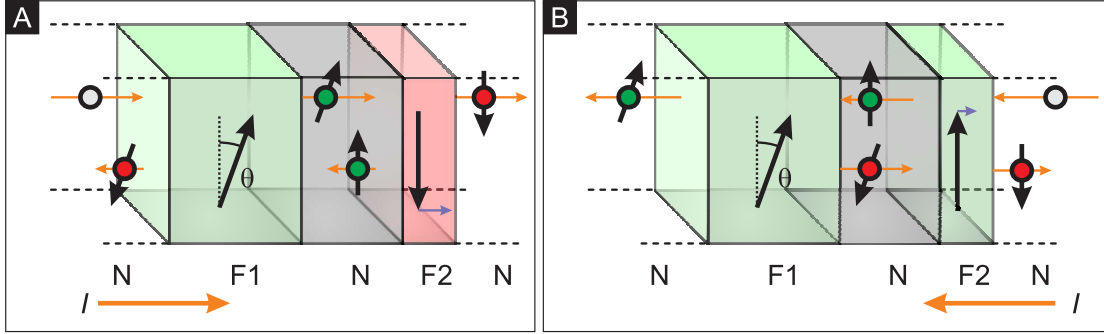
Figure 2.3: A device for current-induced magnetization switching. A non-magnetic region (N) separates a thick ferromagnet (F1) from a thin ferromagnet (F2). (**A**) When an unpolarized current is injected from the left, it gets spin-polarized when passing F1. This spin current affects the magnetization of F2 in a direction so as to align F2 parallel with F1. (**B**) If the current is injected from the right, the spin-polarized electrons try to align F1 parallel with F2. Due to anisotropy forces the magnetization of F1 is fixed, and reflected electrons from F1 exert a spin torque on F2 in a direction so as to align the magnetic moment of the thin ferromagnet antiparallel to F1.

spin-diffusion length, this current will remain spin-polarized when it impinges on the second ferromagnetic layer. Electrons that are reflected from the thin layer are aligned antiparallel to its magnetization, and exert a torque on the magnetic moment of the thick layer to align it parallel to that of the thin layer. In the absence of anisotropy forces, the magnetic moments of both layers would rotate in the same direction [1]. However, due to the high anisotropy of the thick layer, its magnetization is fixed against the spin torque exerted by the reflected electrons. In contrast, the spin torque acting on the thin ferromagnetic layer can be high enough to overcome the anisotropy forces, leading to a magnetization reversal that results in a parallel magnetization configuration of both layers.

When the current is injected from the right, as depicted in Fig. 2.3B, the directions of the torques are reversed due to the symmetry of the system: Now the flow of electrons exerts a torque on the thick layer trying to align its moment parallel to that of the thin layer. But the magnetization of the thick ferromagnet remains stable, and therefore reflected electrons are polarized antiparallel, thereby exerting a torque on the magnetization of the thinner ferromagnet. Consequently, its moment is forced to align antiparallel to the magnetization of the thicker layer and flips at high enough current.

After the reversal, spin-torque, anisotropy and magnetic damping act in the same direction to stabilize the magnetic moment. For weakly interacting layers, either orientation can be stable in the absence of an applied current, so the devices can function as simple current-controlled memory elements.
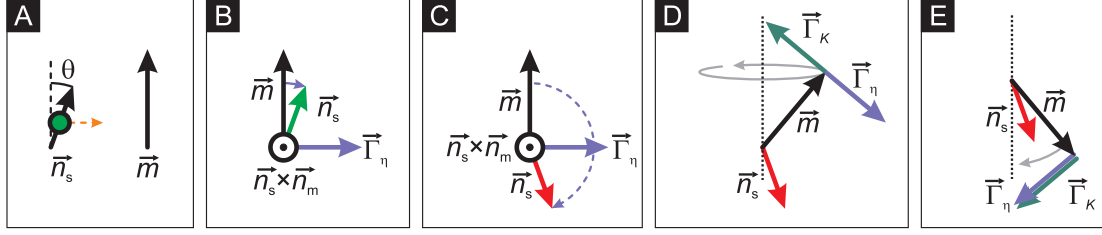
Figure 2.4: Basic principle of spin-torque generation in a macro-spin model. (**A**) Initial configuration. A current with spin polarization along $\vec{n}_s$ passes a ferromagnet with magnetic moment $\vec{m}$ from left to right. (**B**) During spin transfer, a torque $\vec{\Gamma}_\eta$ is generated accordingly to Eq. 2.12. As a result $\vec{m}$ is forced to rotate into a direction lying parallel with the polarization of the incoming spin current. (**C**) To reverse the magnetization, a current with spin polarization antiparallel with $\vec{m}$ is injected. (**D**) This leads to an increase of the precession angle of $\vec{m}$ around its equilibrium position until the spin-angular-momentum transfer torque $\vec{\Gamma}_\eta$ is compensated by the opposing torque $\vec{\Gamma}_K$ originating from the anisotropy field $\vec{H}_K$. (**E**) If the spin current is large enough to overcome $\vec{H}_K$, $\vec{m}$ crosses the equator. Now $\vec{\Gamma}_\eta$ and $\vec{\Gamma}_K$ both stabilize $\vec{m}$ in the reversed orientation.

Macro-spin model and dynamics

Within the so-called Macro-spin model a magnetic particle is assumed to be homogeneously magnetized with all magnetic moments aligned parallel to each other. Then the nanomagnet can be treated as one single macrospin with a total magnetic moment $\vec{m}$ given by the sum of the individual magnetic moments $\vec{m}_i$.

In Fig. 2.4A, the initial configuration is sketched: In the absence of a spin-polarized current, the magnetic moment $\vec{m}$ of the macrospin aligns along the magnetic easy axis due to magnetic anisotropy. Then a spin-polarized current flows through the macrospin from left to the right. The spin-polarization unit vector of the incoming current is denoted $\vec{n}_s$, and the angle enclosed by $\vec{m}$ and $\vec{n}_s$ is called θ.

In analogy to the single electron case described in the previous section, the spin-torque $\vec{\Gamma}_\eta$ affecting the macrospin due to the exchange interaction is given by

$$\vec{\Gamma}_\eta = -g(\vec{n}_m, \vec{n}_s) \cdot \frac{\hbar}{2e} \cdot \eta I \left(\vec{n}_s \times \vec{n}_m \right) \times \vec{n}_m \,, \tag{2.12}$$

where $\vec{n}_m$ is the unit vector of the magnetization of the nanomagnet, I is the spin-integrated current of electrons with charge e, and $\eta = \frac{I_\uparrow - I_\downarrow}{I_\uparrow + I_\downarrow}$ is the spin-polarization factor, where $I_\uparrow$ and $I_\downarrow$ are the spin-polarized currents with their polarization axis defined by the polarizing magnet [1]. The term $g(\vec{n}_m, \vec{n}_s)$ is a numerical prefactor that describes the angular dependence of the efficiency of spin-angular momentum transfer, originating from the quantum-mechanical nature of the interaction between the spin-polarized current and the macro-spin. For simplicity, however, a constant $g(\vec{n}_m, \vec{n}_s) \equiv 1$ is assumed, corresponding to complete absorption of the

transverse angular momentum by the macro-spin.

The spin torque tries to align the macrospin parallel to the polarization direction of the incoming current, as depicted in Fig. 2.4B, showing the cross product $\vec{n}_s \times \vec{n}_m$ and the resulting spin torque $\vec{\Gamma}_\eta$. If the incoming spin current is polarized antiparallel with respect to the macrospin ($90° < \theta < 270°$), $\vec{\Gamma}_\eta$ can lead to reversal of the macrospin, as shown in Fig. 2.4C.

The spin torque $\vec{\Gamma}_\eta$ is the basic interaction that enters the magneto-dynamics equation for the motion of the macro-spin. In the absence of an external magnetic field, the macro-spin dynamics of a magnet with uniaxial anisotropy can be described by the Landau-Lifshitz-Gilbert (LLG) equation in the form

$$\frac{1}{\gamma}\frac{\mathrm{d}\vec{m}}{\mathrm{d}t} = \vec{m} \times \left[\vec{H}_K - \alpha\frac{\vec{m}}{m} \times \left(\vec{H}_K + \vec{H}_\eta \right) \right] , \tag{2.13}$$

where m denotes the magnitude of the magnetic moment $\vec{m}$, γ is the gyromagnetic ratio, $\gamma = g\frac{\mu_B}{\hbar}$ ($g \approx 2$, μ_B is the Bohr magneton), α is the LLG damping coefficient, and $\vec{H}_K$ is the anisotropy field. The spin-angular-momentum transfer term $\vec{H}_\eta$ originating from the spin torque (Eq. 2.12) is given by

$$\vec{H}_\eta = \frac{\hbar}{2e}\frac{\eta}{\alpha m} \cdot I \cdot \vec{n}_s . \tag{2.14}$$

Note that the sign of $\vec{H}_\eta$ depends on the current direction and the sign of η. When a spin-polarized current is injected to the macrospin, the precession angle of $\vec{m}$ around its equilibrium position is increased until the spin torque $\vec{\Gamma}_\eta$ is compensated by the torque $\vec{\Gamma}_K$ of the opposing anisotropy field $\vec{H}_K$, as shown in Fig. 2.4D. If the current is large enough to overcome the anisotropy field, $\vec{m}$ flips to the reversed state. Now both the spin torque and the anisotropy field stabilize the macrospin in the reversed orientation, as shown in Fig. 2.4E.

The critical current I_c that is needed to compensate the anisotropy field is given by the condition $H_\eta(I_c) + H_K = 0$ [1, 9, 34], and a threshold current of

$$I_c = \frac{2e}{\hbar}\frac{\alpha}{\eta}mH_K \tag{2.15}$$

is obtained. For currents above I_c the macrospin becomes unstable over time and a reversal of the magnetic moment occurs.

2.3 Finite-temperature effects

Thermal activation in the absence of a spin torque

At finite temperatures the average precession motion of the macro-spin is affected by the thermal excitations leading to finite probabilities for magnetization reversal.

To describe the temporal evolution of the macro-spin $\vec{m}$ in a first approach, no spin torque contributions are considered, and no external magnetic field is applied. Following the approach of Brown [23], the rapidly fluctuating random forces due to thermal agitation are described by a random field $\vec{H}_L$ which can be added to the anisotropy field term $\vec{H}_K$ in Eq. 2.13. Each component $H_{L,i}$ ($i = x, y, z$) of the field $\vec{H}_L$ is related to the temperature T by

$$H_{L,i}(t) = \sqrt{2\gamma \frac{\alpha}{m} k_B T} \cdot I_{\text{ran},i}(t) \,, \tag{2.16}$$

where $I_{\text{ran}}(t)$ is a gaussian random function with the first two moments of $\langle I_{\text{ran}}(t) \rangle = 0$ and $\langle I_{\text{ran}}^2(t) \rangle = 1$. Hence, the finite-temperature LLG equation is given by

$$\frac{1}{\gamma} \frac{d\vec{m}}{dt} = \vec{m} \times \left[\vec{H}_K + \vec{H}_L - \alpha \frac{\vec{m}}{m} \times \vec{H}_K \right] \,. \tag{2.17}$$

From this equation, both the thermally activated motion of the macro-spin as well as the mean lifetime $\bar{\tau}$ remaining in the potential well described by $\vec{H}_K$ can be determined. Following Boltzmann statistics, $\bar{\tau}$ is given by

$$\bar{\tau} = \tau_0 \cdot \exp\left[\frac{E_b}{k_B T} \right] \,, \tag{2.18}$$

where E_b is the anisotropy energy as seen from the local minimum around which $\vec{m}$ fluctuates, and $\tau_0 \sim (\gamma H_K)^{-1}$ is the reciprocal attempt frequency. Equation 2.17 applies when $E_b \gg k_B T$. This situation is shown in Fig. 2.5A: The energy levels of the spin "down" and spin "up" states are degenerate, and the macro-spin fluctuates between these states. Consequently, when averaging over a long period, the mean lifetime of the macro-spin in the "up" state is equal to that in the "down" state.

Thermal activation including spin torque effects

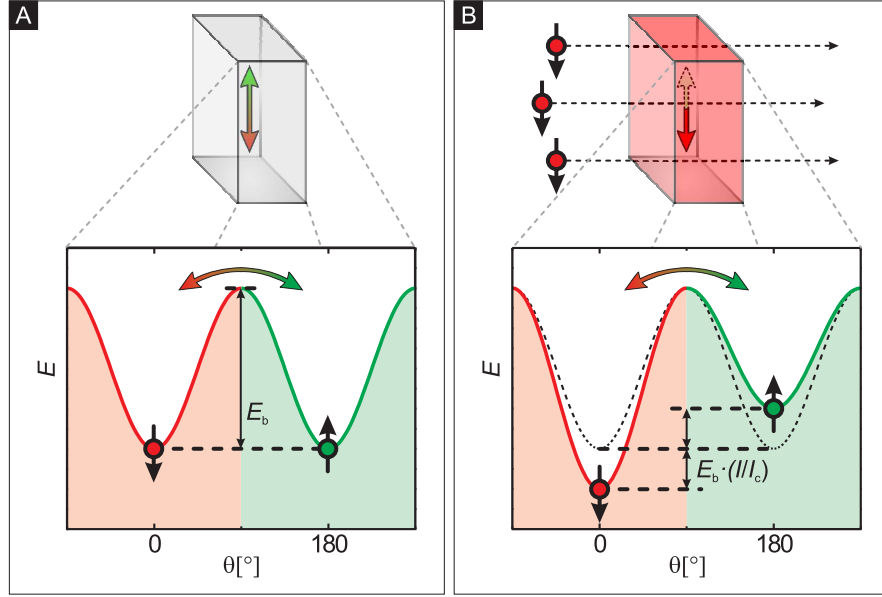In analogy to Eq. 2.13, spin-transfer excitation adds an additional torque term $\vec{H}_\eta$ to Eq. 2.17:

$$\frac{1}{\gamma} \frac{d\vec{m}}{dt} = \vec{m} \times \left[\vec{H}_K + \vec{H}_L - \alpha \frac{\vec{m}}{m} \times \left(\vec{H}_K + \vec{H}_\eta \right) \right] \,. \tag{2.19}$$

If $\vec{H}_\eta$ is collinear to the easy axis of the uniaxial anisotropy term $\vec{H}_K$, then Eq. 2.19 can be rewritten in the form of Eq. 2.17:

$$\frac{1}{\gamma} \frac{d\vec{m}}{dt} = \vec{m} \times \left[\vec{H}_K + \vec{H}_L - \tilde{\alpha} \frac{\vec{m}}{m} \times \vec{H}_K \right] \,, \tag{2.20}$$

with the modified damping coefficient $\tilde{\alpha}$

$$\tilde{\alpha} = \left(1 + \frac{H_\eta}{H_K} \right) \alpha = \left(1 - \frac{I}{I_c} \right) \alpha \,. \tag{2.21}$$

Figure 2.5: (**A**) Intrinsic potential barrier for an uniaxial magnet. Due to thermal activation the magnetization may switch between the two energy minima at $\theta = 0°$ and $\theta = 180°$. Each switch has to overcome the potential barrier E_b, and no orientation is preferred. Consequently, the net magnetization averaged over a long period of time is zero. (**B**) When a spin-polarized current passes the magnet, a spin-torque is generated, leading to an effective modification of the potential barrier inside the magnet. The potential of the magnetic state that is parallel to the spin-polarization of the current is decreased by $E_\mathrm{b} \cdot (I/I_\mathrm{c})$, favoring a parallel orientation of the macro-spin with the incoming spin-current polarization, whereas the potential of the antiparallel state is increased by $E_\mathrm{b} \cdot (I/I_\mathrm{c})$. The net magnetization averaged over a longer period of time is not zero and parallel to the spin-polarization of the current.

Consequently, a spin-polarized current I modifies the effective damping coefficient of the nanomagnet. In this notation, $I < 0$ stabilizes the macrospin in its initial state, whereas $I > 0$ leads to a spin torque that opposes the magnetic anisotropy field. A negative damping coefficient ($\tilde{\alpha} < 0$, which implies $H_\eta > -H_K$) results in magnetic instability and finally to a magnetic reversal of the macro-spin.

Obviously, the macro-spin dynamics including spin-torque effects can be described by Eq. 2.17, with α replaced by $\tilde{\alpha}$. The random field $\vec{H}_\mathrm{L}$ (Eq. 2.16) depends on α and has to be modified. This can be done by introducing a fictitious temperature $\tilde{T}$, such that $\tilde{\alpha}\tilde{T} = \alpha T$. Equation 2.20 then describes the situation for a macro-spin at temperature $\tilde{T}$ with damping $\tilde{\alpha}$. Consequently, the mean thermal

activation lifetime $\bar{\tau}$ of the system is given by

$$
\begin{aligned}
\bar{\tau} &= \tau_0 \cdot \exp\left[\frac{E_{\mathrm{b}}}{k_{\mathrm{B}}\tilde{T}}\right] \\
&= \tau_0 \cdot \exp\left[\frac{E_{\mathrm{b}}}{k_{\mathrm{B}}T}\left(1 - \frac{I}{I_{\mathrm{c}}}\right)\right] ,
\end{aligned}
\tag{2.22}
$$

according to Eq. 2.18. Hence, the potential barrier E_{b} is effectively reduced or increased by the spin-torque effects, and this modification is directly proportional to the spin current I.

A uniaxial magnetic system that thermally reverses its magnetization with an intrinsic mean lifetime $\bar{\tau}$ between two switching events will effectively experience a spin-torque due to a spin-polarized current, thereby adding a preferential alignment to the magnetic moment $\vec{m}$ of the thermally switching magnet. According to Eq. 2.22, the potential barrier E_{b} for switching $\vec{m}$ from antiparallel (AP) to parallel (P) configurations is lowered, whereas the potential barrier for the reversed switching process is increased:

$$
\bar{\tau}_{\mathrm{AP}\to\mathrm{P}} = \tau_0 \cdot \exp\left[\frac{E_{\mathrm{b}}}{k_{\mathrm{B}}T}\left(1 - \frac{I}{I_{\mathrm{c}}}\right)\right]
\tag{2.23}
$$

$$
\bar{\tau}_{\mathrm{P}\to\mathrm{AP}} = \tau_0 \cdot \exp\left[\frac{E_{\mathrm{b}}}{k_{\mathrm{B}}T}\left(1 + \frac{I}{I_{\mathrm{c}}}\right)\right] .
\tag{2.24}
$$

This situation is shown in Fig. 2.5B. Due to the spin-torque effects, a lifetime asymmetry for the two switching processes evolves, and dependent on the current direction, the mean lifetime for the parallel or antiparallel configuration of $\vec{m}$ and $\vec{n}_{\mathrm{s}}$ is increased.

Chapter 3

Scanning Tunneling Microscopy

Scanning tunneling microscopy (STM) and spectroscopy (STS) provides insight into structural and electronic properties of surfaces and nanoparticles on surfaces at a resolution down to the atomic scale. The working principle of STM is based on the quantum mechanical tunneling effect: When an atomically sharp metallic tip approaches an electrically conducting sample at a certain bias voltage, a current starts to flow (at a distance of typically 5 to 15 Å) even before the tip mechanically touches the sample surface.
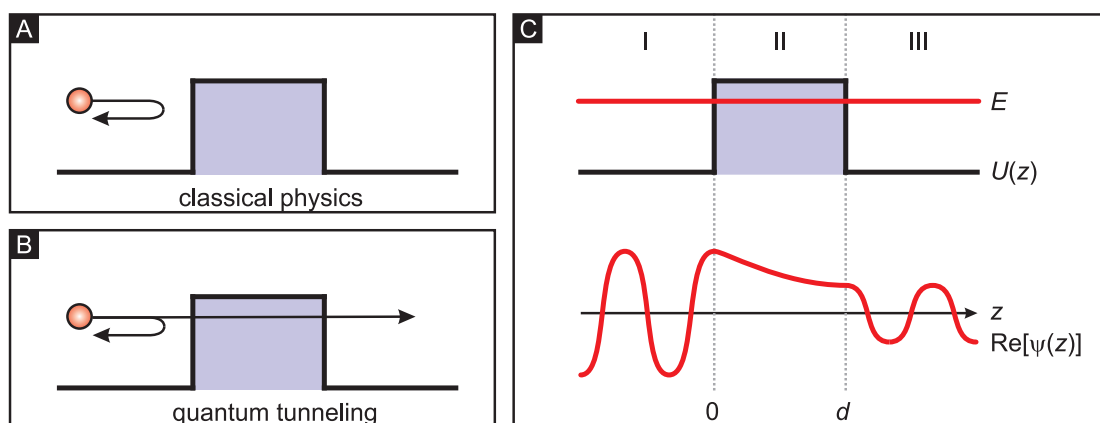
Figure 3.1: (**A**) In classical theory, an electron moving in a potential will be reflected at a potential barrier if its energy is less than the height of the barrier. (**B**) In quantum mechanics, however, the electron has a nonzero probability of tunneling through the barrier of finite height. (**C**) In quantum mechanics, the electron can be described by a wave function $\psi(z)$ that has to fulfill continuity conditions within the three different regions (I,II,III) to solve the time-dependent Schrödinger equation.

3.1   The tunneling effect

In classical mechanics, an electron with energy E moving in a potential $U(z)$ can overcome a potential barrier U_0 only if $E > U_0$—otherwise it is reflected as shown in Fig. 3.1A. In quantum mechanics, the electron is described by a wave function $\psi(z)$ and has a nonzero probability of tunneling through a potential barrier as long as $U_0 < \infty$, as depicted in Fig. 3.1B for an electron approaching a potential barrier of height U_0 and width d. The potential $U(z)$ is constant within each of the three regions shown Fig. 3.1C:

region I: $z < 0$, $U(z) = 0$,   in front of the barrier,
region II: $0 \leq z \leq d$, $U(z) = U_0$,   inside the barrier,
region III: $d < z$, $U(z) = 0$,   behind the barrier.

In each region the quantum mechanical wave function describing the electron satisfies the time-dependent Schrödinger equation,

$$\left(-\frac{\hbar^2}{2m_\mathrm{e}}\frac{\mathrm{d}^2}{\mathrm{d}z^2} + U(z) \right) \psi(z) = E\psi(z), \tag{3.1}$$

where m_e is the electron mass and $\hbar$ is Planck's constant divided by 2π. The respective solutions for the different regions are:

region I: $\psi_1 = \mathrm{e}^{\mathrm{i}kz} + A\mathrm{e}^{-\mathrm{i}kz}$
region II: $\psi_2 = B\mathrm{e}^{-\kappa z} + C\mathrm{e}^{\kappa z}$
region III: $\psi_3 = D\mathrm{e}^{\mathrm{i}kz}$,

where $k^2 = 2m_\mathrm{e}E/\hbar^2$ and $\kappa^2 = 2m_\mathrm{e}(U_0 - E)/\hbar^2$. The incident current density j_i and the transmitted current density j_t can be described by

$$j_\mathrm{i} \;\; = \;\; \frac{\hbar k}{m_\mathrm{e}} \tag{3.2}$$

$$j_\mathrm{t} \;\; = \;\; -\frac{\mathrm{i}\hbar}{2m_\mathrm{e}} \left(\psi_3^*(z)\frac{\mathrm{d}\psi_3(z)}{\mathrm{d}z} - \psi_3(z)\frac{\mathrm{d}\psi_3^*(z)}{\mathrm{d}z} \right) = \frac{\hbar k}{m_\mathrm{e}}|D|^2 \tag{3.3}$$

and the transmission coefficient T is given by the transmitted current density divided by the incident current density:

$$T = \frac{j_\mathrm{t}}{j_\mathrm{i}} = |D|^2 . \tag{3.4}$$

Using the *wave-matching method*, i.e. the continuity of the wave function and its derivative at the discontinuities of the potential, the overall wave function is obtained. The transmission coefficient is then given by

$$T = |D|^2 = \frac{1}{1 + \frac{(k^2+\kappa^2)^2}{4k^2\kappa^2}\sinh(\kappa d)}. \tag{3.5}$$

In the limit of $\kappa d \gg 1$ the transmission coefficient can be approximated by

$$T \approx \frac{16k^2\kappa^2}{(k^2 + \kappa^2)^2} \cdot \mathrm{e}^{-2\kappa d}. \tag{3.6}$$

with $\kappa = \frac{\sqrt{2m_\mathrm{e}(U_0-E)}}{\hbar}$. As T is dominated by the exponential factor $\exp[-2\kappa d]$, tunneling in this model depends exponentially on the barrier width d times the square root of the effective barrier height $U_0 - E$. This explains the high sensitivity of the tunneling current to the tip-sample distance in STM.

3.2 Experimental aspects

On increasing the tip-sample distance by about an Å the tunneling current decreases by about a factor of 10. Therefore, the current is localized at the tip apex where the tip and sample are closest. This explains the high lateral resolution of the STM. However, the tip positioning has to be very accurate. This is accomplished using piezoelectric actuators to control the tip-sample distance as well as the lateral position of the tip above the sample surface. By keeping the tunneling current constant while scanning the tip laterally above the sample the surface topography can be imaged with atomic resolution [35].

A schematic set-up of a STM system is shown in Fig. 3.2. The working principle of the piezoelectric effect is the following: When a voltage is applied to a piezoelectric material, it elongates or contracts, depending on the polarity. In many STM systems, a piezoelectric tube scanner is used with the outer side of the tube scanner covered by four electrode segments (x_+, y_+, x_-, y_-), whereas the inner side is completely contacted by one single electrode (z). When applying a dc voltage between the inner and all outer electrodes, the whole tube scanner elongates or contracts depending on the polarity. This effect moves the tip in the z direction. When the voltage is applied between the two opposite outer electrodes x_+ and x_-, the piezoelectric material is elongated at one electrode and contracts at the other, thereby bending the tube. Consequently, the tip can be moved along the x direction. The same principle is used to control the motion of the tip along the y direction.

To record an image, the z-component of the tip position is adjusted by a feedback loop to keep a constant tunnel current between the tip and the sample while a raster scan generator moves the tip across the surface. In this "topography mode", the z component of the tip position is recorded at every point and thereby provides a measure of the surface contours. Color coding the $z(x, y)$ signal helps to get an impression of the sample surface topography.
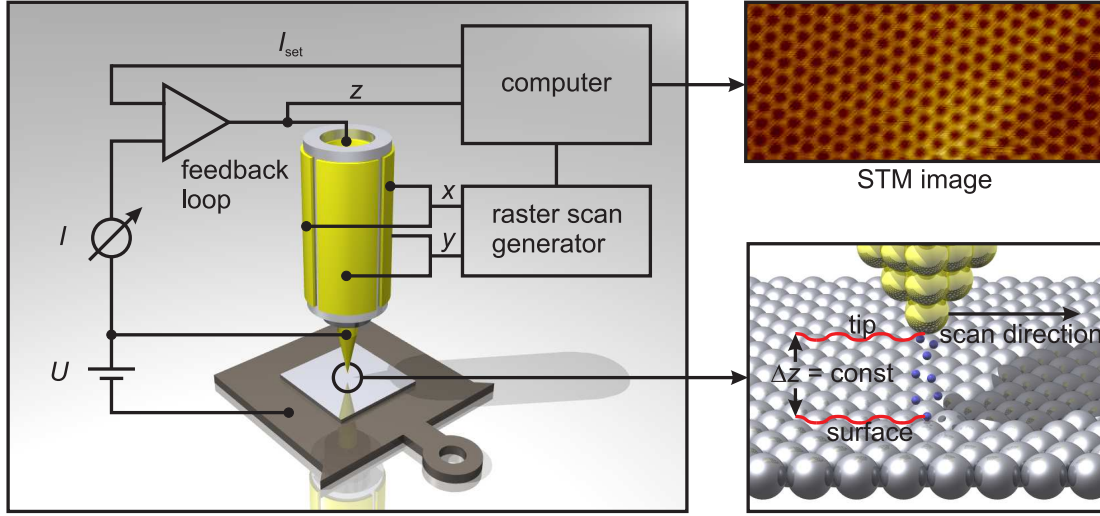
Figure 3.2: Principle of STM in the topography (or constant current) mode. While the tip laterally scans across the surface (controlled by the raster scan generator), the tunneling current is kept constant at a tunnel current setpoint I_{set}. This is done by the feedback loop adjusting the z position of the tip. The respective tip displacement in z is then recorded as a function of the lateral position (x, y) (see inset in the bottom right). STM images are obtained by plotting $z(x, y)$ in a color code (see inset in the top right).

3.3 Surface topography

Although the simple model introduced in Sec. 3.1 contains the inherent exponential dependence of the tunneling current on the tip-sample distance, it fails to explain any dependence of the current on the electronic structure of tip or sample.

To explain the electron tunneling between two weakly coupled electrodes, Bardeen used first-order time-dependent perturbation theory [36]. Tersoff and Hamann applied Bardeen's formalism to the STM geometry in order to appropriately describe the tunneling process in STM [37, 38]. In their work, the tip is approximated by a sphere, and only s-type wave functions contribute to the tunneling matrix elements. The tunneling geometry in the Tersoff-Hamann model is shown in Fig. 3.3, where R is the effective tip radius, $\vec{r}_0$ is the center of curvature of the tip, and d is the tip-sample distance. For low temperatures and small bias voltages U ($\approx 10\,\text{meV}$ for metals), the current can be described by

$$I \propto U \cdot n_{\text{t}}(E_{\text{F}}) \cdot \text{e}^{-2\kappa d} \cdot \sum_{\nu} |\psi_{\nu}(\vec{r}_0)|^2 \cdot \delta(E_{\nu} - E_{\text{F}}) \tag{3.7}$$

where E_{F} is the Fermi energy and $n_{\text{t}}(E_{\text{F}})$ is the density of states at the Fermi level of the tip. The decay rate κ is proportional to the effective local potential barrier height ϕ, which is to a good approximation equal to the average of the tip
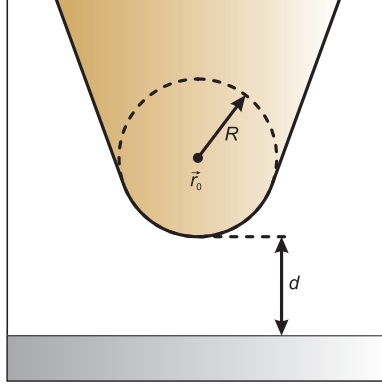
Figure 3.3: Schematic picture of the tunneling geometry between a tip and a sample, as treated in the Tersoff-Hamann model: d denotes the tip-sample distance, R the effective tip radius, and $\vec{r}_0$ is the center of curvature of the tip.

and sample work functions. The quantity

$$n_{\mathrm{s}} = \sum_{\nu} |\psi_{\nu}(\vec{r}_0)|^2 \cdot \delta(E_{\nu} - E_{\mathrm{F}}) \tag{3.8}$$

can be identified with the surface local density of states (LDOS) at the Fermi level, evaluated at $\vec{r}_0$. The tip wave functions ψ_{ν} decay exponentially into the vacuum—hence, the current depends exponentially on the tip-sample distance:

$$I \propto \mathrm{e}^{-2\kappa d} \tag{3.9}$$

Using these approximations the topographic STM data, which are obtained by recording the z component as a function of the lateral position (x, y) while scanning with the tip across a sample surface at a fixed tunnel current I, is interpreted as follows: According to Eq. 3.7, the area $z(x, y)|_{I=\mathrm{const.}}$ is a trace of constant LDOS at E_{F} above the surface at the location of the tip. In this simple model, the LDOS follows the topography to a good approximation and the constant current images can be interpreted as the topography of the surface.

3.4 Electronic properties

In the previous section the tunneling process was described using the Tersoff-Hamann model in the limit of low bias voltage U. When U is increased, this model can be extended to a tunneling current weighted over a range of energies

$$I \propto \int_0^{eU} n_{\mathrm{s}}(E) \cdot n_{\mathrm{t}}(E, eU) \cdot T(E, eU) \mathrm{d}E \tag{3.10}$$
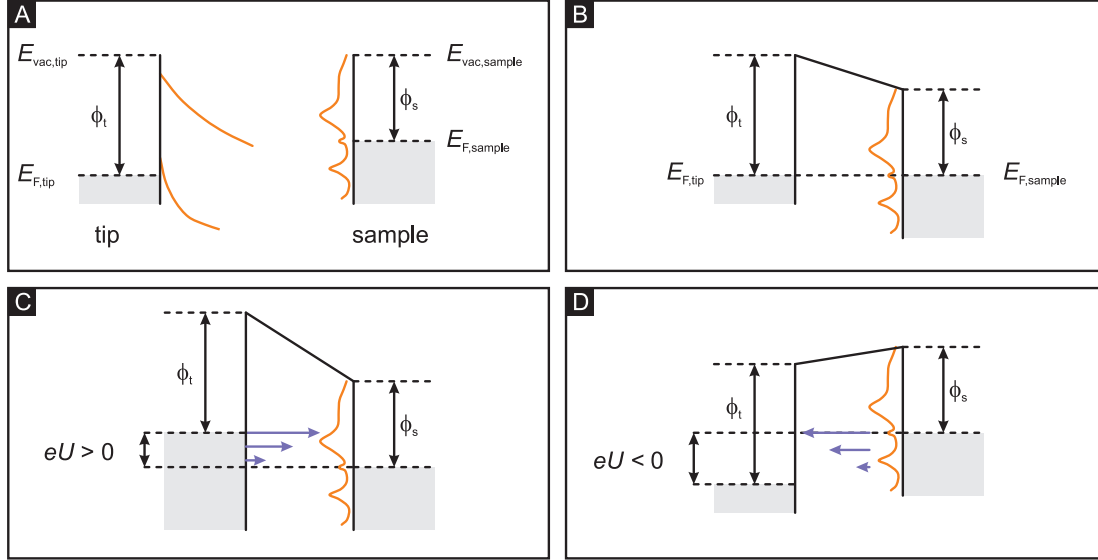
Figure 3.4: Energy level diagrams for sample and tip. (**A**) Independent tip and sample. (**B**) Tip and sample separated by a small vacuum gap in electronic equilibrium ($E_{\mathrm{F,tip}} = E_{\mathrm{F,sample}}$). (**C**) Positive sample bias: electrons tunnel from the tip into the sample. (**D**) Negative sample bias: electrons tunnel from the sample into the tip.

with a transmission factor

$$T(E, eU) = \exp\left[-d \cdot \sqrt{\frac{4m}{\hbar^2}\phi_{\mathrm{t}} + (\phi_{\mathrm{s}} + eU - 2E)}\right], \qquad (3.11)$$

ϕ_{t} and ϕ_{s} beeing the work functions of tip and sample, respectively.

A schematic representation of the tunneling process as introduced in Eq. 3.10 is shown in Fig. 3.4 [39]. The left and right electrodes represent the tip and sample, and the shaded regions indicate the occupied states below the Fermi level E_{F} (A). In the equilibrium state ($U = 0$) the Fermi energies of the tip and sample are at the same level and the net tunneling current is zero (B). Applying a bias voltage leads to a shift of the Fermi levels by eU. When $U > 0$, electrons from occupied states of the tip in the energy interval from $E_{\mathrm{F}} - eU$ to E_{F} tunnel into unoccupied states of the sample (C). For $U < 0$ the situation is reversed and electrons from occupied sample states tunnel into unoccupied states of the tip (D). The current mainly originates from electrons tunneling from the Fermi level E_{F} since they experience the lowest energy barrier.

Assuming n_{t} being constant, differentiation of Eq. 3.10 results in

$$\frac{\mathrm{d}I}{\mathrm{d}U}(U) \propto n_{\mathrm{t}}(0) \cdot n_{\mathrm{s}}(eU) \cdot T(E, eU) + \int_0^{eU} n_{\mathrm{s}}(E) \cdot n_{\mathrm{t}}(eU - E) \cdot \frac{\mathrm{d}T(E, eU)}{\mathrm{d}U} \mathrm{d}E \quad (3.12)$$

Often the second term of Eq. 3.12 can be neglected. Assuming T varies monotonically with U, the differential tunneling conductance dI/dU is a good measure of n_s at an energy equal to eU [40].

Experimentally, $dI/dU(U)$ is measured by stabilizing the tip above the surface at I_{stab} and U_{stab}. To fix the tip-sample distance, the feedback loop is then switched off. While the voltage is ramped from the initial to a final voltage, the tunneling current is measured. By numerical differentiation of $I(U)$ curves the respective dI/dU signal can be obtained. In this work the lock-in technique was used to determine dI/dU. Here, a small ac modulation is added to the bias voltage at a high reference frequency f_{ref} of several kHz, and the respective response in the I signal at f_{ref} is analyzed with a lock-in amplifier.

To investigate the electronic structure of a sample with lateral resolution, so-called dI/dU *spectroscopy maps* can be obtained. In this case a spectrum is taken at every position (x, y) on the surface. This technique enables topographic $z(x, y)$ and spectroscopic properties $dI/dU(x, y, eU)$ of the sample to be correlated directly.

If only the electronic structure at one particular energy eU_0 is of interest, the acquisition of dI/dU-maps with fixed bias voltage U_0 is a time-saving alternative to full dI/dU spectroscopy maps. In contrast to the full dI/dU spectra, where the feedback loop is switched off during voltage ramping, the dI/dU signal at fixed bias U_0 can be recorded with the feedback loop on. Simultaneously to the topographic measurement, a lock-in technique derives the dI/dU signal at the voltage U_0 while the tip is scanned under constant current conditions.

3.5 Spin-polarized scanning tunneling microscopy

So far the electrons were only regarded as charge carriers. However, an electron also carries spin. This section deals with the dependence of the tunneling current on the spin. Slonczewski treated the problem of tunneling between two spin-polarized electrodes theoretically [32]. In the limit of vanishing bias voltage U and under the assumption of a free-electron behavior of the conduction electrons, the spin-polarized tunneling current I_{sp} between two spin-polarized electrodes can be described by

$$I_{sp}(U_0) = I_0[1 + P_1 \cdot P_2 \cdot \cos(\angle(\vec{m}_1, \vec{m}_2))], \tag{3.13}$$

where I_0 is the spin-averaged current, $P_i = \frac{\Omega_{i,\uparrow} - \Omega_{i,\downarrow}}{\Omega_{i,\uparrow} + \Omega_{i,\downarrow}}$ is the spin polarization ($\Omega_{i,\uparrow}$ and $\Omega_{i,\downarrow}$ denote the respective pure spin $\uparrow$ and spin $\downarrow$ density of states of electrode i), and $\vec{m}_i$ is the magnetic moment of the electrodes [32]. The $\cos\theta$ dependence of tunneling conductance on the angle θ between the magnetic moments of two electrodes has been first verified experimentally by Julliere in 1975 [30], and this principle is also used in SP-STM experiments where a magnetic probe tip scans across
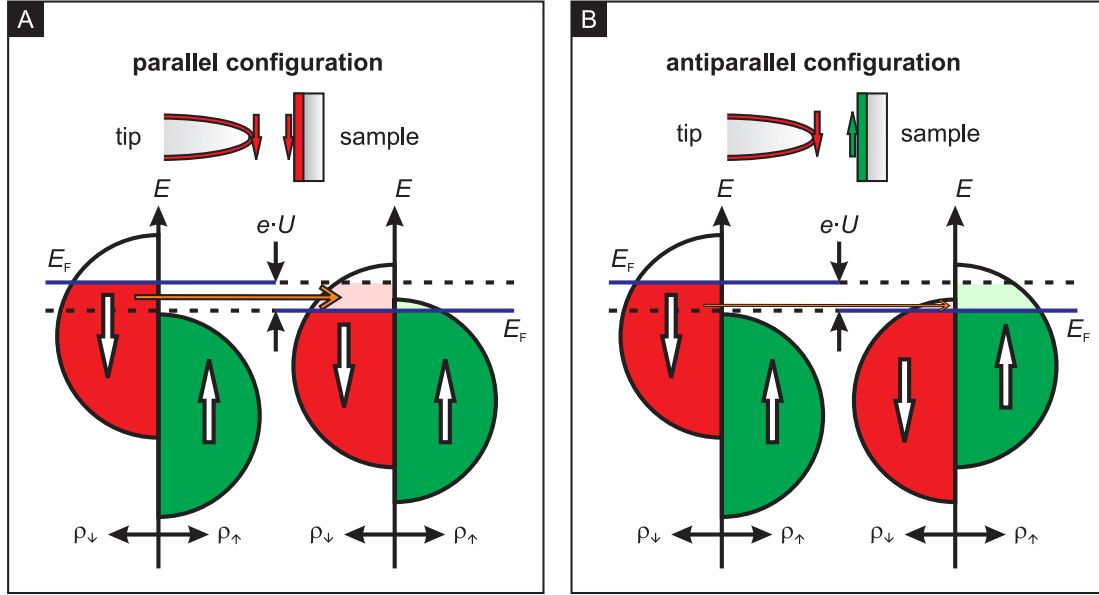
Figure 3.5: Spin-polarized scanning tunneling microscopy (with spin and energy conservation) for the case of positive sample bias. (**A**) Parallel configuration of tip and sample magnetizations: Only spin ↓ electrons from the tip can tunnel into unoccupied spin ↓ states of the sample. (**B**) Antiparallel configuration. The number of unoccupied spin ↓ states of the sample is drastically decreased compared to the parallel magnetic configuration, leading to a reduced tunneling current.

a magnetic surface while recording the differential tunnel conductance dI/dU. The variation of the dI/dU signal as a function of lateral tip position results in a map that represents the magnetic structure of the sample.

The concept of spin-polarized tunneling based on electron spin and energy conservation is shown in Fig 3.5 for parallel (A) and antiparallel (B) configuration of the magnetic electrodes. Each of the magnets is characterized by its spin-split density of states $\rho_\uparrow(E)$ and $\rho_\downarrow(E)$. For positive bias voltage U, an electron with spin ↓ can only tunnel from the tip into an unoccupied sample state with spin ↓. Since the tunneling probability depends on the number of electronic states available the spin-polarized current will be larger for the parallel configuration of the magnetic electrodes than for the antiparallel one. The Tersoff-Hamann theory has been extended by Wortmann *et al.* [41] for the case of STM imaging with a spin-polarized tip:

$$dI/dU(\vec{r_t}, U) \propto \underbrace{n_t \cdot n_s(\vec{r_t}, E_F + eU)}_{\text{spin-averaged}} + \underbrace{\vec{m}_t \cdot \vec{m}_s(\vec{r_t}, E_F + eU)}_{\text{spin-dependent}}, \qquad (3.14)$$

where $\vec{m}_t$ and $\vec{m}_s$ are the vectors of the energy-integrated LDOS magnetizations of tip and sample, respectively, and $\vec{r_t}$ denotes the position of the tip apex. It has

been assumed that the spin-up and spin-down tip density of states is constant in energy which might not be true in general.

The spin-dependence of the tunneling current in SP-STM experiments with two magnetic electrodes has been nicely demonstrated with a ferromagnetic CrO_2 tip scanning above a Cr(001) surface [42], thereby confirming the theoretically predicted idea of the topological antiferromagnetic order of the Cr(001) surface with alternately magnetized terraces separated by monatomic steps [43, 44], as shown in Fig. 3.6A. The contribution from spin-dependent tunneling leads to alternating step heights when scanning with a closed feedback loop. For a parallel configuration of tip and sample magnetization the tunnel current is larger than for the antiparallel case when measured at the same tip-sample distance. However, with a closed feedback-loop the distance changes to keep the tunnel current constant. Consequently, the tip-sample distance has to be decreased when changing from the parallel to the antiparallel configuration. This leads to the alternating step heights shown in Fig. 3.6B.

Using Eq. 3.14, the differential tunneling conductance dI/dU can be divided into a spin-averaged part and a spin-dependent part. A magnetic dI/dU-map of the sample can be acquired by choosing the appropriate bias voltage for high contrast of the dI/dU signal on different magnetic domains. In Fig. 3.6C, the topography of the Cr(001) surface is shown, whereas the simultaneously obtained dI/dU map in Fig. 3.6D reveals the magnetic domain structure.

The interplay between the integrated tunnel current I and the dI/dU signal has been worked out by Kubetzka *et al.* [45] in detail. The dI/dU signal recorded on different magnetic domains at the same distance (with open feedback loop) may differ drastically from that obtained with closed feedback loop:

Imagine a magnetic tip and a magnetic sample at fixed bias voltage $U > 0$ with electrons tunneling from the tip into the sample. Then all spin $\uparrow$ and spin $\downarrow$ states of the tip in the energy range between the Fermi energy E_F and $E_F + eU$ contribute to the integrated current I with a non-vanishing spin-polarization. When the tip moves from one magnetic domain to another, the tunnel junction is assumed to switch from the parallel to the antiparallel configuration. Because the resistance has increased, the tip has to be moved closer to the surface to maintain the current I. The simultaneously recorded dI/dU signal also changes, because a) the electronic configuration of the tunnel junction changed due to the modified tip-sample distance and b) the magnetic configuration changed due to the movement from one magnetic domain to another. To ensure that the dI/dU signal is recorded at the same distance z, a bias voltage U is chosen that corresponds to a vanishing spin-polarization of the integrated current I. Under this condition, the dI/dU signal recorded in magnetic dI/dU maps is directly correlated to the density of magnetic states at the energy $E = eU$. Furthermore, if the integrated current polarization is not zero, *cross-talk* between the topography map and the dI/dU map can be observed resulting in a magnetic structure superimposed on the
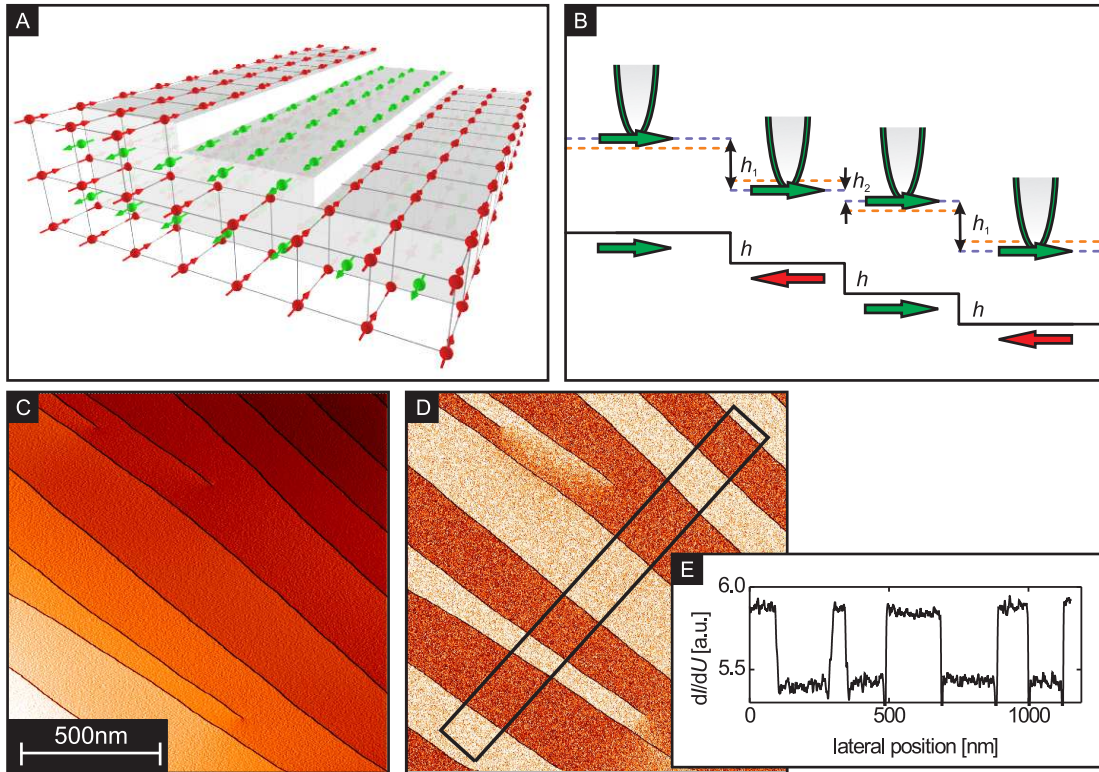
Figure 3.6: (**A**) Model of the Cr(001) surface as a topological antiferromagnet: Each of the terraces are ferromagnetic, and adjacent terraces separated by monatomic steps are coupled antiparallel. (**B**) SP-STM experiments show an alternating step height ($h_1 > h_2$) due to spin-dependent contributions to the spin-polarized tunnel current (blue line). Using a non-magnetic tip results in a constant step height (h, orange line). (**C**) Constant-current mode STM image of the Cr(001) surface. Nine terraces separated by monoatomic steps are visible. (**D**) Simultaneously acquired spin-resolved dI/dU map at $U = -100\,\text{mV}$ sample bias. (**E**) dI/dU signal line section of the marked rectangle in (D). The signal level changes at every step between low and high due to antiparallel magnetization of adjacent terraces.

topography. However, in most of the SP-STM experiments it is important to image topographic and magnetic features simultaneously to correlate the information. To clearly separate the topographic (z) from the magnetic (dI/dU) channel, an appropriate bias voltage U has to be chosen.

In this thesis, the influence of high spin-polarized currents on thermally switching magnetic nanoislands is described. In contrast to the SP-STM mode where a vanishing integrated spin polarization is used, the experiments on the current-induced magnetization switching were performed at bias voltages connected to an appreciable integrated spin-polarization and a non-vanishing contrast in the dI/dU signal. This allows to simultaneously modify and observe the magnetic properties of a particular nanoisland.

Chapter 4

Instrumentation and Preparation

To study clean and well-ordered magnetic nanostructures by means of SP-STM, the instrumental setup has to ensure the cleanliness and repeatibility of the experiments. Under vacuum conditions at a base pressure of 10^{-6} mbar, within one second one atomic layer will be adsorbed from the residual gas onto a clean surface, assuming a sticking coefficient of unity [46]. The studies presented in this thesis were performed under ultra-high vacuum conditions (UHV, pressures below 10^{-9} mbar) to ensure stable experimental conditions.

4.1 The UHV system

The experiments are performed in a commercial UHV chamber system [47]. It consists of four chambers separated by UHV valves: (i) a load-lock with a dedicated pumping system, allowing tip and sample transfer into the system within several hours, (ii) a dosing chamber for gas adsorption (not used in this work), (iii) a chamber for preparation of tips and samples, and (iv) an analysis chamber equipped with a unit for Auger electron spectroscopy (AES) and low energy electron diffraction (LEED). A top view of the analysis chamber is shown in Fig. 4.1. A satellite of the analysis chamber contains the variable temperature STM (VT-STM) for SP-STM/STS investigations. Tips and samples are transferred between the chambers by linear manipulators. Each of the analysis and preparation chambers is equipped with an ion-pump. Their base pressure is below 1×10^{-9} mbar ($= 1 \times 10^{-7}$ Pa).

The main facilities used in this work are an electron beam heater, Cr and Fe evaporators, an (x, y, z)-manipulator equipped with a resistive heater, and a O_2 dosing valve. All these devices are mounted to the preparation chamber shown in Fig. 4.2.
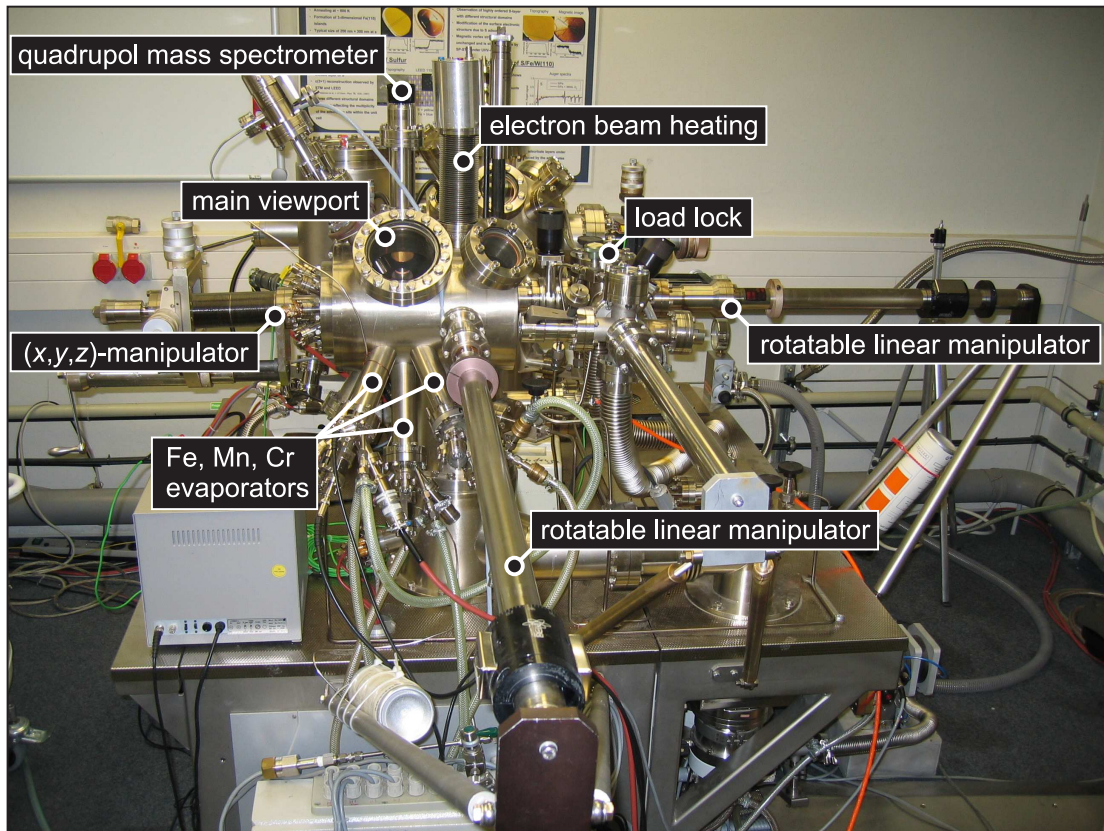
A home-built electron beam heater is used to prepare W tips and W(110) substrates, where temperatures up to $T = 2400$ K are required. It consists of two parallel tungsten wires serving as a stage for tip and sample holders. The wires
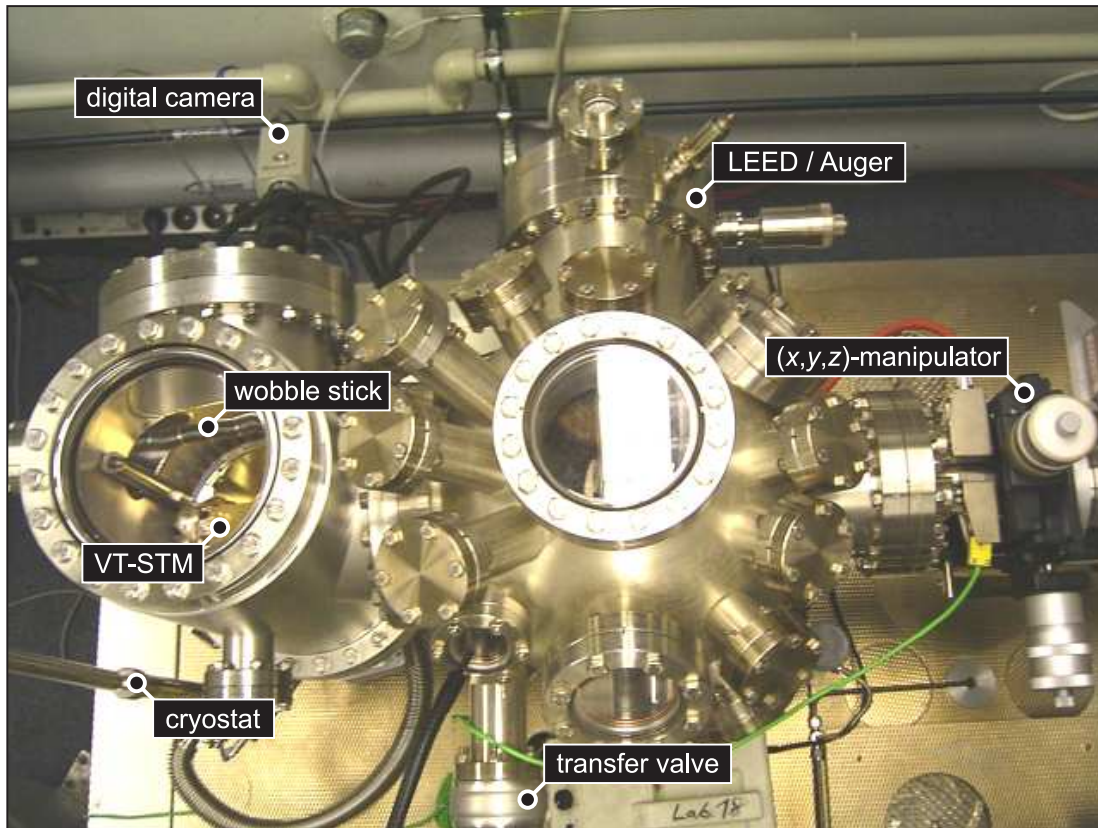
Figure 4.1: Top view of the analysis chamber. It is equipped with a LEED/Auger unit and the VT-STM. Tips and samples from the preparation chamber are transfered through the transfer valve into the (x, y, z)-manipulator which either serves to position the sample in front of the LEED/Auger unit or to transfer it to the satellite chamber with the VT-STM. Here, a wobble-stick is used to insert tips and samples into the VT-STM. A digital camera helps to manually approach the tip to the sample before the automatic approach is used to get into tunneling contact.

can be connected to a high voltage, $U_{\mathrm{HV}} < 2000\,\mathrm{V}$. A tungsten filament powered by a dc current $I_{\mathrm{fil}} \approx 3.5\,\mathrm{A}$ serves as a cathode. As the filament is heated it emits electrons which are accelerated by the high voltage thereby heating the sample. The temperature of the sample is measured with an infrared pyrometer using an emission coefficient $\epsilon = 0.43$.
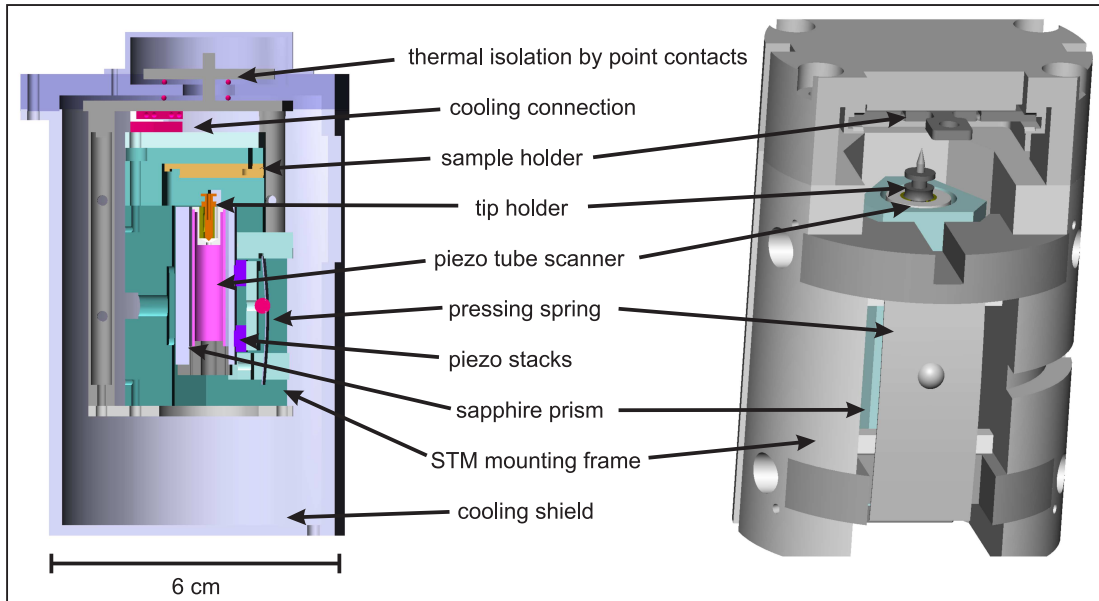
Cr and Fe are evaporated using electron beam evaporators equipped with flux monitors. The evaporator material is heated by bombardment with electrons from a thoriated tungsten filament which has a rather low work function facilitating the electron emission. A water-cooled copper shield avoids unwanted heating of the surroundings that could cause impurities in the evaporator beam. Cr is evaporated from a crucible and Fe is evaporated from a wire. To calibrate the evaporators, submonolayer amounts of the respective metals were deposited on a clean W(110)

Figure 4.2: Side view of the preparation chamber. New tips and samples are transfered from the load-lock chamber for *in vacuo* preparation. The electron beam heater is used to clean tips and the W substrate. Tips and samples can be positioned in front of the Fe and Cr evaporators using the (x, y, z)-manipulator. Clean W subtrates are prepared by dosing oxygen into the chamber.

substrate, and the coverage is determined by STM. The evaporation rates used in this work are $9\,\mathrm{ML/min}$ for Cr and $1.2\,\mathrm{ML/min}$ for Fe.

Samples and tips are positioned in front of the evaporators using the (x, y, z)-manipulator. In order to anneal thin film coated tips or samples, the preparation chamber is equipped with a resistive heater, allowing temperatures between room temperature (RT) and $T = 1150\,\mathrm{K}$, measured indirectly with a chromel/alumel thermocouple. A dosing valve is connected to the preparation chamber in order to introduce O_2 gas into the UHV system for cleaning the W(110) substrate (see Sec. 4.4).

thermal isolation by point contacts

cooling connection

sample holder

tip holder

piezo tube scanner

pressing spring

piezo stacks

sapphire prism

STM mounting frame

cooling shield

6 cm

Figure 4.3: Technical drawing of the VT-STM: Cross-section of the whole instrument (left) and three-dimensional model of the STM body (right).

4.2 The variable-temperature scanning tunneling microscope

The home-built variable-temperature STM is specifically designed for the study of temperature-dependent magnetic phenomena by SP-STM. A detailed description of the VT-STM can be found in the Ph.D. thesis of Torben Hänke [48].

The STM allows studies at temperatures between 20 K and 300 K and is equipped with a tip exchange mechanism. In order to allow high energy resolution of STS at low temperatures and to keep thermal drift between the tip and the sample at a minimum, the whole microscope is cooled. A cooled tip also allows a larger choice of magnetic materials to be used to coat the SP-STM tips, because ultra-thin magnetic films are often paramagnetic at temperatures near RT.

The STM is based on a design developed by D. Haude [49]. It includes a fast tip exchange mechanism and is well isolated from mechanical, acoustic or electronic noise sources. The high resonance frequency of the STM in combination with an external low resonance frequency damping stage results in an effective filter against mechanical noise. The damping stage consists of a massive copper base plate that is suspended from four metal springs. The STM is located on top of the base plate and thermally decoupled by six small ruby balls that are clamped between the base plate and the STM housing. For the coarse approach of the tip to the sample a piezoelectrically driven stepper motor is used, built in the "walker"
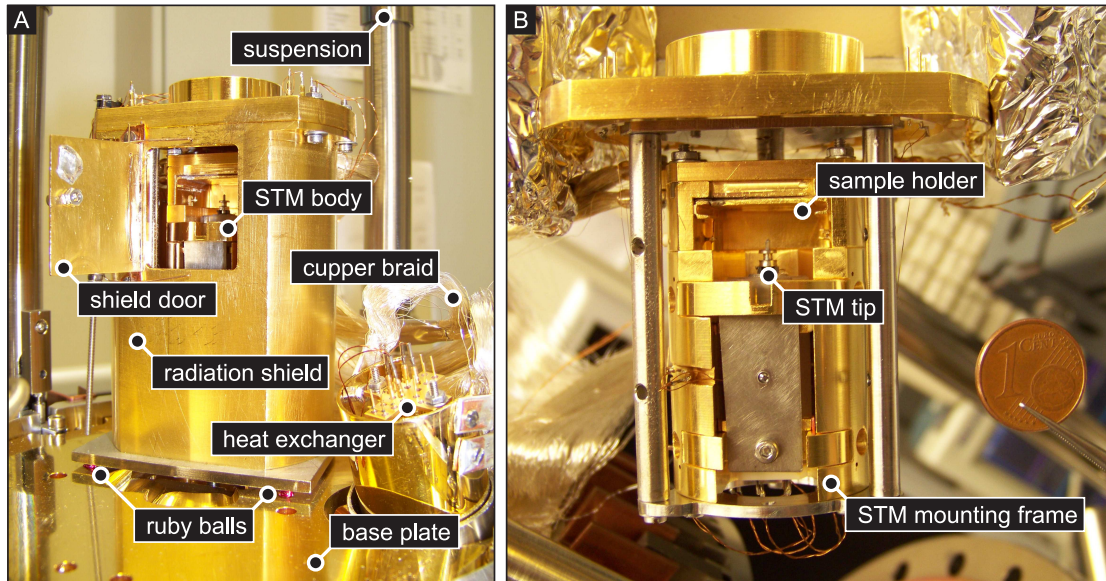
Figure 4.4: (A) Photograph of the VT-STM instrument. The base plate is mounted with an eddy current damping. The STM body is located inside the radiation shield which is mounted on top of the base plate and thermally decoupled by ruby balls. The whole STM is cooled via copper braids connected to the heat exchanger of the liquid Helium flow cryostat. Ruby balls serve as thermal decoupling from the base plate. Tips and samples can be inserted after opening the shield door. (**B**) Detailed view of the STM. The STM mounting frame is designed to maximize the thermal decoupling from the radiation shield. The tip is approached from the bottom, and the sample is mounted upside down into the sample holder. A one-cent coin indicates the size.

design [50].

A technical drawing of the STM is shown in Fig. 4.3, and Fig. 4.4 shows a photograph of the instrument. The sample is mounted upside down in the sample holder, and the tip is approached from the bottom. The tip is mechanically clamped inside the piezoelectric tube scanner which is glued into the sapphire prism of the coarse approach mechanism. The sample temperature is measured using a GaAs/GaAlAs diode sensor fixed to the STM body close to the sample holder.

The whole VT-STM is cooled by a liquid He flow cryostat from CryoVac [51]. The temperature is controlled by a manual valve regulating the amount of liquid He flowing through the cryostat and an electric heating. The temperature at the heat exchanger is stabilized by an integrated PID-temperature controller. Oxygen-free and high-conductive copper braids provide the thermal connection between the STM and the cryostat. Their high flexibility avoids the transmission of vibrations to the STM. The cryostat exhaust cools a radiation shield surrounding the STM. The STM body has a slightly higher temperature ($\Delta T \approx 10\,\mathrm{K} - 15\,\mathrm{K}$)

than the heat exchanger, measured by the additional temperature sensor on the STM body. The lowest base temperature of approximately $18\,\mathrm{K}$ at the sample is reached within two hours, starting at RT. Here, the heat exchanger reaches the final minimum temperature of $T_{\mathrm{ex}} = 6\,\mathrm{K}$ rather quickly, while the sample follows with some delay.

In order to perform STM measurements at variable tunnel currents of up to $I \approx 5\,\mu\mathrm{A}$, a commercial current-to-voltage amplifier "FEMTO DLPCA-200" [52] is used. In this project tunnel currents of up to $I_{\mathrm{max}} \in \{100\,\mathrm{nA},\ 1\,\mu\mathrm{A},\ 10\,\mu\mathrm{A}\}$ were used in the respective amplification ranges between $10^8\,\mathrm{V/A}$ (for low current) and $10^6\,\mathrm{V/A}$ (for high current). In principle the amplifier can be used to set currents in the mA range. However, the tip-sample configuration will change from a tunneling to a direct mechanical contact at a certain tunnel conductance limit [53].

4.3 Tip preparation

SP-STM/STS strongly depends on the electronic and magnetic stability of the tips. In this project, magnetic sensitive tips were prepared by *in-situ* coating with Cr by evaporation and subsequent annealing [20]. The tips are sharpened from a 0.8 mm diameter polycrystalline W wire by electrochemical ac-etching in a solution of NaOH in distilled water (8 g NaOH per 100 ml H_2O). After etching, the tip is clamped into a tip holder and fixed to a tip shuttle. After inserting the tip into the UHV system, it is flashed to $T = 1500\,\mathrm{K}$ in order to remove the oxide layer at the tip. The flash also results in an increased adhesion of the magnetic films. However, high-resolution SEM images show that the heating also melts the tip apex leading to a tip radius of about 500 nm. Probably, a small cluster protrudes from the tip, which is responsible for the lateral resolution of SP-STM.

To make the tip magnetically sensitive, it is coated with a few hundred monolayers of chromium followed by annealing at $T = 550\,\mathrm{K}$ for $t = 240\,\mathrm{s}$. The annealing results in a thin stable magnetic film at the tip apex. By choosing other materials or film thicknesses the in-plane or out-of-plane sensitivity of the magnetic tip and the presence or absence of stray fields from the tip can be controlled. In this work, only W tips coated with a Cr film at least 100 monolayers thick are used, because they are sensitive to the in-plane component of the sample magnetization and do not exhibit any significant stray-field [54]. Antiferromagnetic tips are most suitable for detailed studies of ferromagnetic samples as the absence of tip stray fields excludes interactions between the tip and the sample magnetization.

4.4 Preparation of W(110) substrates

The cleanliness of the substrate plays a crucial role in the growth of nanostructures. Because of its high melting point and low miscibility a W(110) crystal is
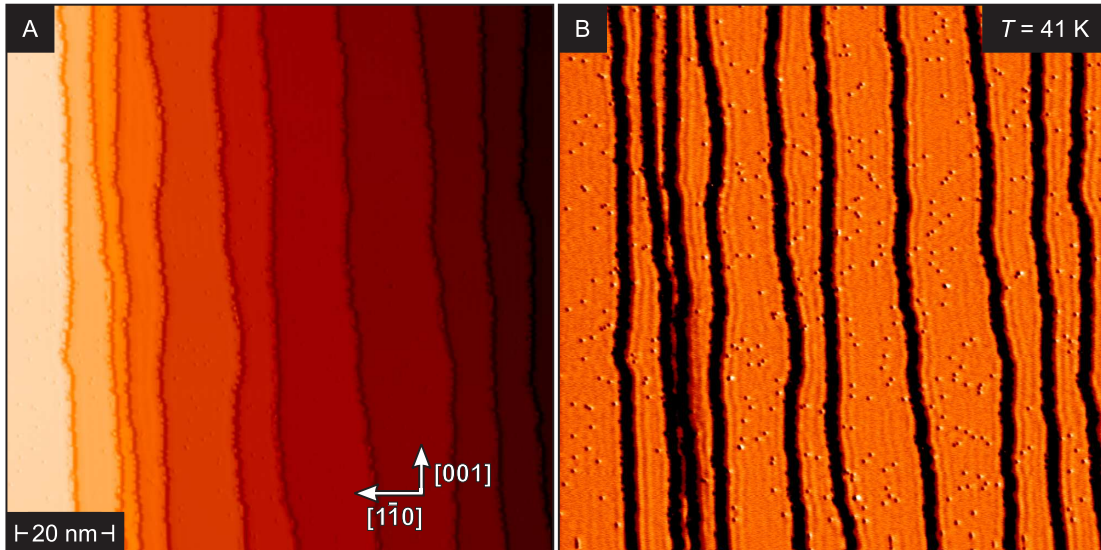
Figure 4.5: The W(110) substrate. (**A**) Constant-current topographic overview image and (**B**) simultaneously measured dI/dU map of a typical W(110) surface as prepared within this thesis ($I = 20\,$nA, $U = -200\,$mV, bare tungsten tip). While eleven atomically flat terraces separated by monatomic step edges can be recognized in the topography, the dI/dU map reveals striking periodic variations, mainly along the step edges. Approximately 340 individual residual adatoms can be identified.

suitable as a substrate for various metals and serves as the substrate for all experiments performed. On the clean W(110) surface a pronounced wave pattern in the differential conductance maps can be observed. This pattern originating from step edges and residual impurities on the surface is linked to a downwards dispersing electron band with an upper band edge $E_0 = (314 \pm 12)\,$meV and an effective mass $m_{\text{eff}} = (-1.15 \pm 0.05) \cdot m_{\text{e}}$. Comparison with the W(110) band structure obtained by density functional theory (DFT) calculations reveals that a $p_z d_{xz}$-like surface resonance is responsible [55].

The W(110) surface is cleaned by cycles of annealing ($T \approx 1500\,$K for about 30 min) in oxygen atmosphere and a subsequent high-temperature flash ($T \approx 2300\,$K for 15 s) in UHV at a base pressure of $P \leq 1 \times 10^{-9}\,$mbar. Temperatures are measured with an infrared pyrometer using an emission coefficient $\epsilon = 0.43$. Oxygen of 99.9999% purity is dosed with a leak valve, and the chemical composition of the residual gas in the preparation chamber can be analyzed with a quadrupole mass-filter. At any step of the oxygen treatment P_{ox} is at least 500 times higher than any other partial pressure. The oxygen partial pressure is decreased stepwise from $P_{\text{ox}} = 2 \times 10^{-6}\,$mbar in the initial cycle to $P_{\text{ox}} = 4 \times 10^{-8}\,$mbar in the final cycle.

During the annealing process carbon impurities segregate to the surface, where they react with the oxygen to form CO and CO_2. This process leads to a carbon

depletion layer below the surface. Flashing the surface desorbs the adsorbed oxygen and tungsten oxides.

The topography of the W(110) surface as prepared for our experiments is shown in Fig. 4.5A. The simultaneously obtained electronic $\mathrm{d}I/\mathrm{d}U$ map shown in Fig. 4.5B reveals periodic variations mainly along the step edges. This wave pattern originates from the surface resonance and indicates that the W(110) surface is sufficiently clean. On the terraces, $N_{\mathrm{impurity}} \approx 350$ adatoms can be counted. Calculating the overall number of W surface atoms N_{W} within the image section leads to a ratio of $N_{\mathrm{impurity}}/N_{\mathrm{W}} \approx 2 \times 10^{-3}$, which is comparable to the results published in Ref. [55].

Once the crystal has been prepared by the described procedure, it is usually sufficient to flash the crystal between sample preparations to obtain a clean substrate. Nevertheless, after a number of deposition-flashing cycles the substrate begins to accumulate impurities, probably carbon, originating either from the evaporated material or from segregation. When the impurity concentration gets too high, the surface resonance vanishes, and the W(110) surface has to be cleaned in oxygen again.

Chapter 5

Growth and Magnetism of Fe/W(110)

All the experiments presented in this work have been performed on iron nanoislands on a W(110) substrate. In the past, the system Fe/W(110) has been studied intensively with various techniques. In the low-coverage regime Fe/W(110) exhibits very interesting structural, electronic and magnetic properties. This chapter covers aspects of growth and magnetic properties relevant to the experiments performed in this thesis.

5.1 Growth

The structure of Fe on W(110) depends on various parameters such as coverage and growth temperature. The main structural properties in the low coverage regime are driven by the large lattice mismatch of 9.4% between the two materials
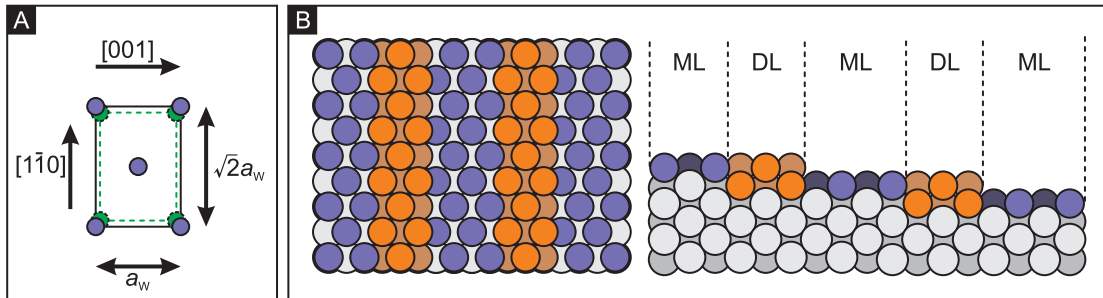
Figure 5.1: Growth of Fe on a W(110) substrate. (**A**) The high lattice mismatch between the two-atomic surface unit cells of the substrate (black rectangle) and Fe (green dotted rectangle) induces stress in the wetting monolayer. (**B**) Sketch of the atomic coordination of a step-flow grown Fe film on a vicinal W(110) (grey circles) surface with a coverage of one (blue circles, ML) and two (orange circles, DL) layers of Fe in a top-view (left) and a side view (right).

(lattice constant of W: $a_{\mathrm{W}} = 3.165\,\text{Å}$ and of Fe: $a_{\mathrm{Fe}} = 2.867\,\text{Å}$ [56]), as depicted in Fig. 5.1A. This lattice mismatch deeply affects the growth of the first Fe layers, and the growth process depends strongly on the substrate temperature.

The first atomic layer (AL) grows pseudomorphically, creating nanoislands, patches and decoration of step edges at RT and stripes growing along step edges at elevated substrate temperature, until a closed film is formed at a nominal coverage of $\theta = 1.0\,\text{AL}$. This wetting monolayer is stable up to $T = 1100\,\text{K}$, where the film starts to evaporate from the substrate [57]. This stability against clustering is generally expected when the free surface energy of the substrate ($2.9\,\text{J/m}^2$ for W) is larger than that of the film ($2.0\,\text{J/m}^2$ for Fe), increased by the interface energy [57, 58]. In simple terms, the monolayer is stable because the Fe-W bond is stronger than the Fe-Fe bond, and therefore atoms avoid the second layer if empty sites are available in the first one.

A substrate held at room temperature leads to the nucleation of free second-layer islands and the decoration of step edges. With increasing coverage the island sizes increase, and finally the islands coalesce into a network. Additionally, dislocation lines evolve, which serve as nucleation centers for the third layer that grows before the second layer is complete.

At elevated substrate temperature step-flow growth dominates. Consequently, double layer stripes emerge already at coverages $1\,\text{AL} < \theta < 2\,\text{AL}$. These stripes form along the step edges and are separated by monolayer stripes, as shown in Fig. 5.1B. At $\theta = 2\,\text{AL}$ a closed double-layer film forms with sporadic dislocation lines along the [001] direction. By incorporation of additional Fe atoms these dislocation lines lead to a relaxation of the stress along the [1$\bar{1}$0] direction.

These dislocation lines form a regular pattern for the third AL, and areas with a local coverage of 4 AL up to 12 AL show a two-dimensional reconstruction network. At higher coverages Fe is completely relaxed and reaches the bulk lattice constant [59, 60]. Whereas three-dimensional islands are formed for higher coverage and higher growth temperature [61], the wetting monolayer is always observed in between the islands.

5.2 Magnetism

The magnetic properties of the Fe/W(110) system have been investigated in the past, leading to the discovery of many interesting effects [54, 57, 62–69]. Its magnetization is strongly connected to the growth and therefore governed by lattice mismatch and relaxation with increasing film thickness.

The magnetization of a closed monolayer film of Fe/W(110) is driven by its uniaxial anisotropy, leading to an easy axis of magnetization pointing along the [1$\bar{1}$0] direction. Consequently, the Fe monolayer exhibits in-plane ferromagnetic order, and a Curie-temperature of $T_{\mathrm{c}} = 225\,\text{K}$ has been determined experimen-

tally [57, 70]. Combined Kerr magnetometry and SP-STM experiments allow the investigation of the monolayer magnetism in more detail [71]: Adjacent magnetic domains are separated by domain walls having a width $w_{\mathrm{ML}} = 0.6 \pm 0.2\,\mathrm{nm}$, and if the substrate terraces are narrow (typically about $10\,\mathrm{nm}$), the magnetic domains of adjacent stripes exhibit a dipolar antiparallel coupling. From Kerr magnetometry experiments measuring the magnetic susceptibility χ as a function of temperature T, the effective activation barrier energy e_{W} per atomic row is estimated to $e_{\mathrm{W}} = (7.6 \pm 0.7)\,\mathrm{meV}$. The combination of both results allows the exchange stiffness $A = 1.8^{+1.1}_{-0.7} \times 10^{-12}\,\mathrm{J/m}$ and the uniaxial anisotropy constant $K = 20.3^{+13.0}_{-7.4} \times 10^{6}\,\mathrm{J/m^3}$ ($4.2\,\mathrm{meV/atom}$) for the monolayer system of Fe/W(110) to be estimated.

At coverages above one monolayer, second-layer stripes form along the step edges. In contrast to the monolayer, the easy axis of magnetization on the double layer is oriented perpendicular to the surface [62, 63]. Furthermore, the domain walls in the second-layer exhibit the same rotational direction of the magnetization, which is attributed to the Dzyaloshinskii-Moriya interaction playing a significant role in that coverage regime and breaking the symmetry of right and left rotating domain walls [54, 72]. If the coverage is increased further until the second layer is complete, the magnetization exhibits an out-of-plane stripe pattern with domains preferentially aligned along the $[1\bar{1}0]$ direction.

For a local coverage of more than two monolayers the magnetic easy axis switches back from perpendicular to in-plane. Another spin reorientation to the [001] easy direction occurs at approximately $\theta = 22\,\mathrm{AL}$ [73]. Different magnetic structures are observed for three-dimensional islands depending on their size and shape. Smaller island form a single domain state, whereas larger islands contain magnetic vortices [61]. Nevertheless, the wetting monolayer in between the islands maintains its uniaxial ferromagnetic in-plane ordering.

5.3 Topography and magnetism of iron nanoislands

All the experiments described here have been performed on iron nanoislands on a W(110) substrate. Nominally 0.14 atomic layers of iron have been evaporated onto a clean W(110) substrate held a room temperature. The topography of a Fe/W(110) sample with pseudomorphically grown monolayer islands at $T = 35\,\mathrm{K}$ is shown in Fig. 5.2A. Obviously, the iron atoms either decorate the step edges or form small nanoislands. The islands have typical diameters between $2\,\mathrm{nm}$ and $6\,\mathrm{nm}$, thereby consisting of about 100 atoms. In between the islands a standing wave pattern can be recogized in the $\mathrm{d}I/\mathrm{d}U$ map. This feature of non-magnetic origin can be attributed to a surface resonance band and serves as an indicator for the high cleanliness of the W(110) substrate (see Sec. 4.4).

The simultaneously recorded magnetic $\mathrm{d}I/\mathrm{d}U$ map at $T = 35\,\mathrm{K}$ in Fig.5.2B
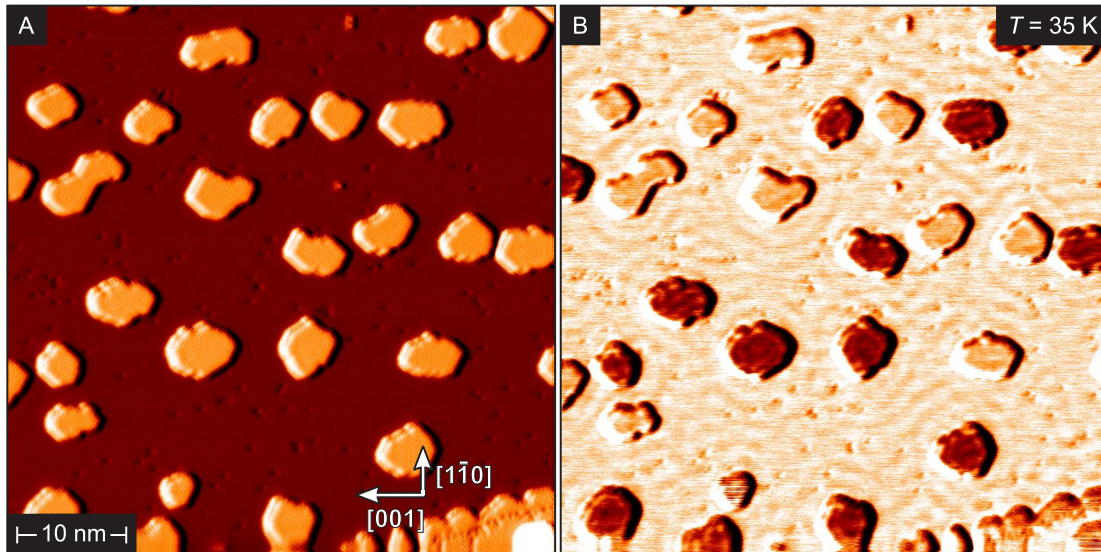
Figure 5.2: (**A**) Topography and (**B**) in-plane magnetic dI/dU map of Fe monolayer islands on W(110) measured at $T = 35\,\text{K}$ (parameters: $I = 2\,\text{nA}$, $U = -150\,\text{mV}$). A dark or bright signal on the islands represents a magnetization direction parallel or antiparallel to the tip magnetization, respectively. In between the islands a standing wave pattern is visible on the substrate, indicating its high cleanliness.

reveals two stages of contrast on the iron islands (dark and bright). As stated above, the monolayer system of Fe/W(110) exhibits a uniaxial ferromagnetic order. Hence, the projection of the tip magnetization onto the magnetization of the nanoislands is not zero, and the dark and bright dI/dU signal reflects the two possible magnetic configurations of the nanoislands. The dI/dU signal on every individual nanoisland is homogeneous, and no domain structure is observed. Obviously, the nanoislands are in a monodomain magnetic configuration due to their small sizes. Larger overview images indicate that the nanoislands do not exhibit a preferential orientation of the magnetization, therefore the net magnetization is zero when averaging over numerous islands.

To summarize, the Fe/W(110) nanoislands with diameters between $2\,\text{nm}$ and $6\,\text{nm}$ exhibit a stable magnetization at $T = 35\,\text{K}$. For the following experiments, the temperature has been increased. The question arises to what extend the magnetization of the nanoislands is influenced by thermal excitation.

Chapter 6

Thermally Induced Magnetization Switching of Nanoislands

In the previous chapter it has been shown that nanoislands consisting of approximately 100 atoms on a W(110) substrate are in a single domain state of magnetization, as revealed by SP-STM experiments at $T \approx 30\,\mathrm{K}$. With increasing temperature the magnetization becomes unstable due to thermal activation, and this can be seen in the respective $\mathrm{d}I/\mathrm{d}U$ signal when tunneling from a (thermally stable) magnetic tip into an individual nanoisland.

## 6.1 Observation of thermally induced magnetization switching

A topographic overview of an ensemble of magnetic iron nanoislands on a W(110) substrate at $T = 56\,\mathrm{K}$ is shown in Fig. 6.1A. Three W(110) terraces decorated with nanoislands of different sizes and shapes can be recognized. In contrast to images taken at low temperature, the simultaneously obtained magnetic $\mathrm{d}I/\mathrm{d}U$ map in Fig. 6.1B reveals that the islands are not completely dark or bright, but show a characteristic stripe pattern. This pattern can be explained by the thermally induced magnetization switching of the nanoislands: The SP-STM image is taken line by line (for most of the images presented in this work, the fast scanning direction is always along the [001] direction of the substrate), and because the magnetization of each island switches frequently, the $\mathrm{d}I/\mathrm{d}U$ signal on the islands changes, reflecting the respective orientation of tip and sample magnetization. Consequently, the islands appear dark for some lines and bright for some others in the magnetic map, leading to a stripe pattern as can be clearly seen in the inset in Fig. 6.1B. Note that in between two switching events the nanoisland is in the single domain state. The switching frequency strongly depends on the island size and shape [27, 74–76], which is reflected by the different stripe widths appearing
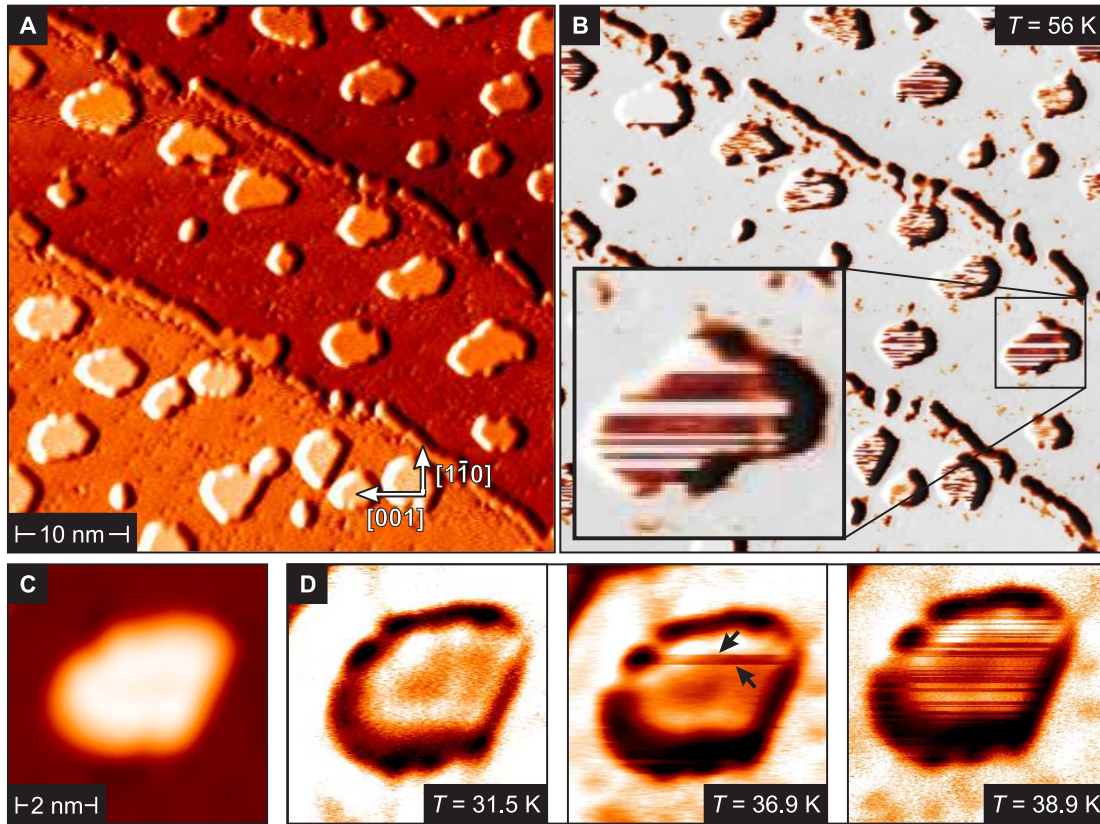
Figure 6.1: (**A**) Topography and (**B**) in-plane magnetic dI/dU map of Fe monolayer nanoislands on W(110) measured at $T = 56\,\mathrm{K}$ ($I = 2\,\mathrm{nA}$, $U = -200\,\mathrm{mV}$). Stripes appear on the islands (see inset) because they switch their magnetization frequently due to thermal activation. (**C**) Topography and (**D**) magnetic dI/dU maps ($I = 2\,\mathrm{nA}$, $U = -200\,\mathrm{mV}$) of a single nanoisland recorded at three different temperatures, showing an increased switching frequency with increasing temperature.

on the nanoislands in Fig. 6.1B: At the same temperature, small islands switch more frequently than larger ones.

Figure 6.1C shows the topography of one individual nanoisland that has been investigated at three different temperatures. The three respective magnetic dI/dU maps are shown in Fig. 6.1D. At $T = 31.5\,\mathrm{K}$, the magnetization is stable, as indicated by the homogenous dI/dU signal on the island. With increasing temperature an increasing switching frequency is observed: two reversal events are recorded at $T = 36.9\,\mathrm{K}$ (marked by arrows), and an irregular stripe pattern evolves for $T = 38.9\,\mathrm{K}$ due to multiple switching events.
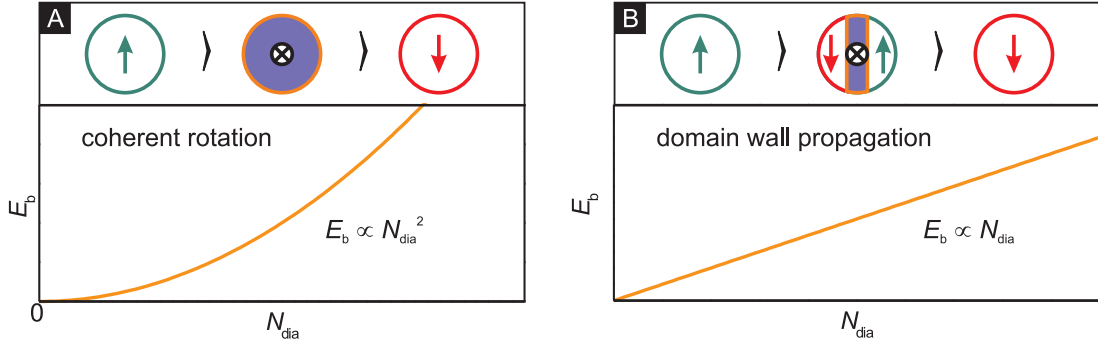
Figure 6.2: Models of reversal in circular shaped magnetic nanoparticles. (**A**) Coherent rotation: All magnetic moments align parallel, even during the switching process. Therefore, the effective activation energy is proportional to the island size, or to the square of its diameter. (**B**) Nucleation of a domain wall: A domain wall nucleates at one edge of the island, and reversal is achieved by the propagation of the domain wall. Consequently, the effective activation barrier is given by the maximum energy of the domain wall which is proportional to the diameter of the nanoisland.

Magnetization reversal models

Néel[22] and Brown[23] calculated the switching probability for a magnetic particle with uniaxial anisotropy under the assumption of coherent rotation, i.e. the magnetic moments of the particle are parallel and behave as one single macrospin. In this model the mean lifetime $\bar{\tau}$ between two switching events is described by the so-called Néel-Brown law

$$\bar{\tau} = \frac{1}{\nu_0} \cdot \exp\left[-\frac{E_b}{k_B T}\right], \tag{6.1}$$

with ν_0 being the Arrhenius prefactor, E_b the effective activation energy barrier that separates the two degenerate magnetization states ("up" and "down"), k_B the Boltzmann constant, and T the temperature.

In a simple model for a coherent rotation of all atomic spins within a monolayer island, E_b is equal to the total magnetic anisotropy energy (Fig. 6.2A):

$$E_{b,\text{coh}} = V \cdot K, \tag{6.2}$$

with K being the anisotropy constant and V the volume of the island. For a circular island, $E_{b,\text{Coh}} \propto K N_{\text{dia}}^2$, with N_{dia} being the island diameter. Consequently, a parabolic dependence of $E_{b,\text{coh}}$ on N_{dia} is expected for a coherent rotation of all spins.

If reversal is achieved via the nucleation of a domain wall that propagates through the nanoisland, E_b scales with the domain wall energy, which is propor-

tional to the length of the wall N_{dia} (see Fig. 6.2B) [77]:

$$E_{\mathrm{b,DW}} = 4S\sqrt{AK} = 4N_{\mathrm{dia}}\left(\frac{a}{\sqrt{2}}\right)^2\sqrt{AK}, \tag{6.3}$$

with a the lattice constant, $S = N_{\mathrm{dia}}(a/\sqrt{2})^2$ the area of the domain wall and A the exchange stiffness. Obviously, one would expect a linear scaling of $E_{\mathrm{b,DW}}$ with increasing island diameter N_{dia} for a reversal process that takes place via domain wall nucleation and propagation.

Although the Néel-Brown law was derived for particles that switch their magnetization coherently, both reversal processes can be described by an Arrhenius law, using an effective activation barrier energy for each respective process.

6.2 Data analysis techniques

Since magnetization reversal of thermally switching nanoislands takes place on a time scale of nanoseconds [78, 79], the STM time resolution of the $\mathrm{d}I/\mathrm{d}U$ signal (which is typically about $1\,\mathrm{ms}$) is not high enough to resolve the reversal process itself. Consequently, one has to find an indirect way to distinguish between the two proposed models of magnetization reversal. To find out which model best describes the magnetization reversal, the effective activation barrier energy E_{b} and the Arrhenius prefactor ν_0 have been determined for a number of individual nanoislands by deducing the mean lifetime τ between two magnetic switching events as a function of temperature T.

The detailed analysis methods are described in the following for the example of a single nanoisland (Fig. 6.3). Using two topographic line sections along the crystallographic axes [001] and [1$\bar{1}$0], the respective diameters $N_{[001]}$ and $N_{[1\bar{1}0]}$ of the island are determined, counted as a number of atomic rows (AR), as shown in (Fig. 6.3A). The selected nanoisland has a width of $N_{[001]} = (19 \pm 1)\,\mathrm{AR}$ along the [001] and $N_{[1\bar{1}0]} = (14 \pm 1)\,\mathrm{AR}$ along the [1$\bar{1}$0] direction. An atomic lattice can be superimposed to the topography to roughly estimate the atomic coordination within the nanoisland.

To record the time-dependent evolution of the island magnetization, the scanning probe tip is positioned on top of the center of the nanoisland. In this so-called point-mode experiment the magnetic $\mathrm{d}I/\mathrm{d}U$ signal is recorded as a function of time at one fixed temperature, as shown in Fig. 6.3B. The signal abruptly changes between two discrete levels, reflecting the island magnetization switching from parallel or antiparallel configurations (or vice versa) with respect to the stable tip magnetization. Then the lifetimes τ between two consecutive switching events is determined for the whole data set to plot a lifetime histogram, as shown in Fig. 6.3C. Approximately a thousand switching events have to be recorded to get
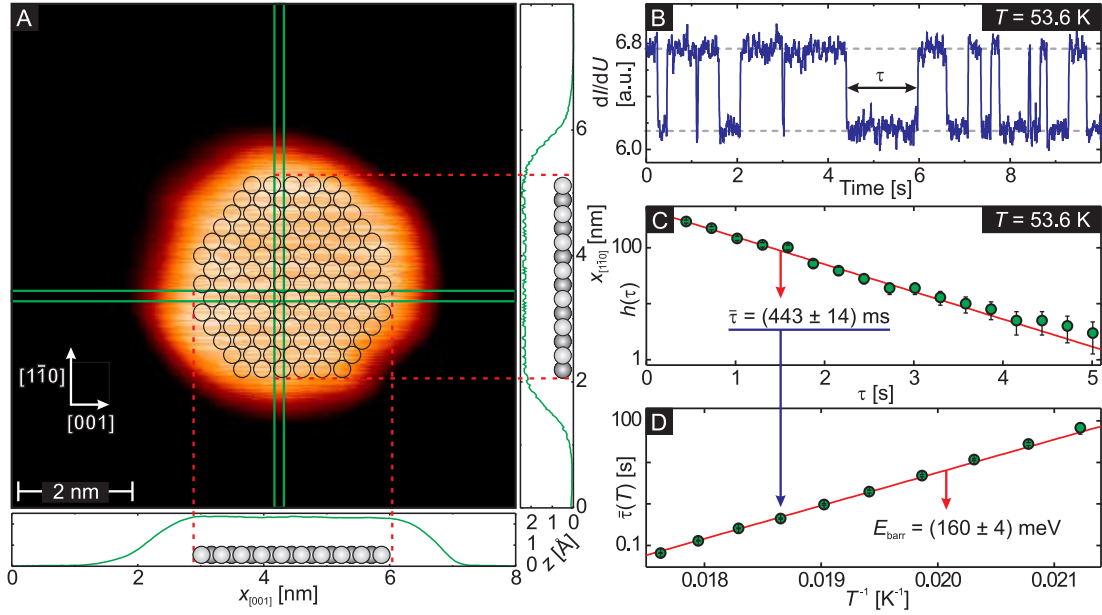
Figure 6.3: Example for the data analysis of an individual nanoisland. (**A**) Topography: The island width along the [001] and [1̄10] crystallographic directions (in number of atomic rows) is determined using respective linesections (panels next to the image) averaged over the area in between the green lines. (**B**) Section of the magnetic dI/dU signal recorded after positioning the SP-STM tip above the center of the island, showing a telegraphic signal corresponding to the switching behavior. Every single lifetime τ between two switching events is determined. (**C**) Respective histogram of lifetimes τ. Fitting with a decay law results in the mean lifetime $\bar{\tau}$. (**D**) Mean lifetime $\bar{\tau}$ in dependence of T^{-1} as determined for different temperatures T. The effective activation barrier energy E_b (slope) and Arrhenius prefactor ν_0 (offset) can be directly deduced from fitting the data with an Arrhenius-like function.

good statistics in the lifetime distribution. Similar to radioactive decay, the lifetime distribution can be described by an exponential decay law, and fitting the data results in the mean lifetime $\bar{\tau} = (443 \pm 14)\,\text{ms}$ for $T = 53.6\,\text{K}$. This procedure of lifetime determination is then repeated for different temperatures. The result for the selected nanoisland is shown in Fig. 6.3D. An Arrhenius-like behavior of $\bar{\tau}(T^{-1})$ is clearly visible. Fitting the data yields the effective activation energy barrier E_b and the Arrhenius prefactor ν_0 for each nanoisland investigated.

6.3 Experimental results

The above described procedure to determine the effective activation barrier energy E_b and Arrhenius prefactor ν_0 have been performed on eleven nanoislands that are shown in Fig. 6.4A. Each island is labeled in a sequence of increasing size. Note that the figure is a scaled composition of STM topography images that have
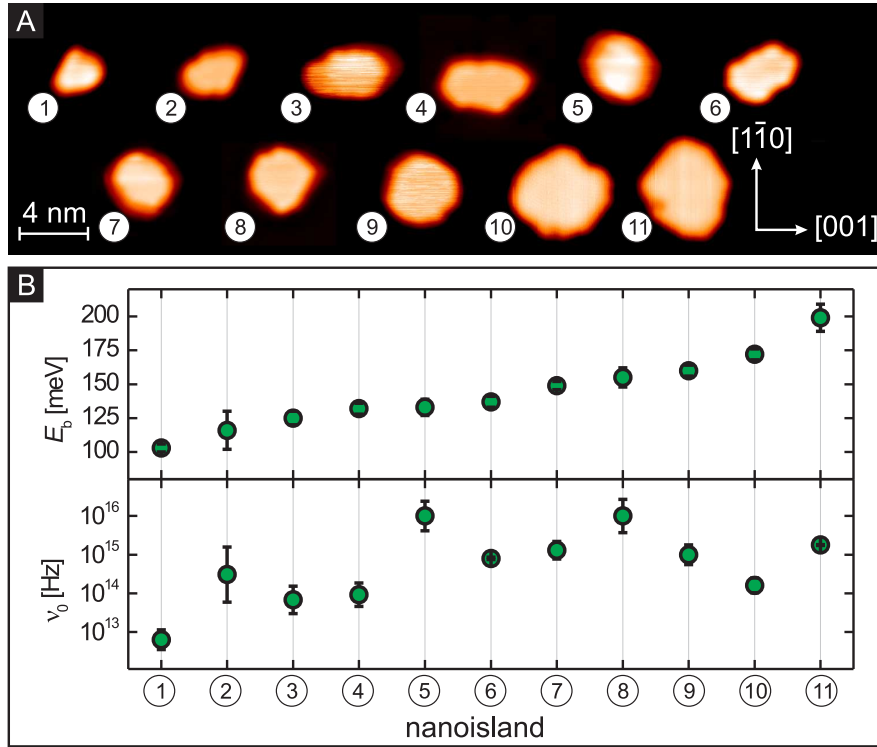
Figure 6.4: (**A**) Topography maps of all nanoislands that have been investigated for their thermal induced switching behavior. (**B**) Effective activation energy barrier E_b (top panel) and prefactor ν_0 (bottom panel) as determined for each of the nanoislands.

been obtained in different experiments.

To get a deeper insight into the magnetization reversal processes, all the selected nanoislands fulfill the following three criteria:

- They are all clearly separated from Fe decorated W(110) step edges or neighboring islands, thereby preventing interactions with the environment that may cause deviations from the intrinsic thermal switching behavior.

- All islands are very compact, showing almost circular or only slightly elongated shapes without kinks, thereby excluding multiple nucleation centers that may cause a complex magnetization reversal behavior.

- The islands consist purely of Fe atoms, with no impurity atoms that may influence the magnetic properties of the islands. The absence of impurities is checked both in the topography and the $\mathrm{d}I/\mathrm{d}U$ map.

The parameter E_b as well as ν_0 are determined for each nanoisland from two to up to ten different temperatures. The results are summarized in Fig. 6.4B, showing E_b and ν_0 for each island. An overall tendency of increasing E_b with
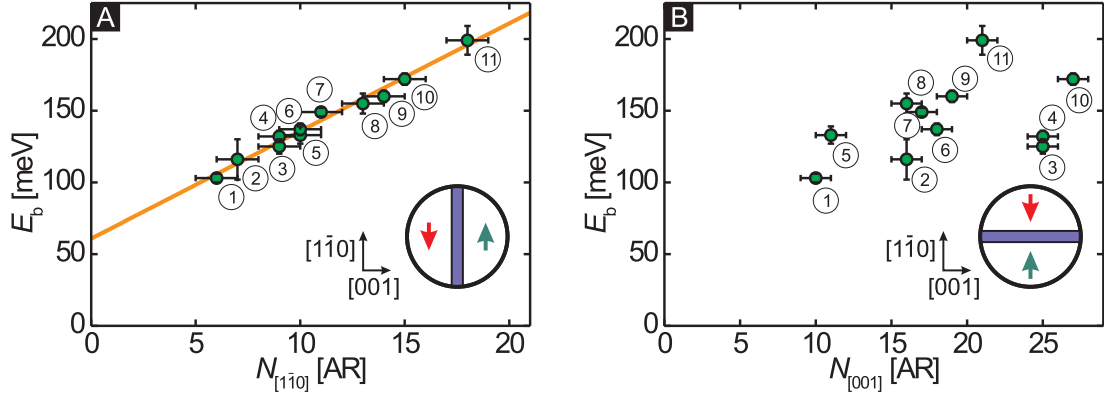
Figure 6.5: (**A**) Effective activation energy barriers E_b as a function of island diameter in number of atomic rows $N_{[1\bar{1}0]}$ along the $[1\bar{1}0]$ direction. A linear dependence is clearly visible, favoring a magnetization reversal by a domain wall moving along the [001] direction, as indicated in the inset. Fitting the data with a linear regression leads to $E_b = (61 \pm 5)\,\text{meV} + N_{[1\bar{1}0]} \cdot (7.5 \pm 0.4)\,\text{meV}$. (**B**) E_b of the same islands, plotted as a function of diameter in atomic rows $N_{[001]}$ along the [001] direction. No linear dependence on $N_{[001]}$ is visible, the model of a magnetization reversal by a domain wall moving along the $[1\bar{1}0]$ direction (see inset on the lower right) can be excluded.

increasing island size is visible, whereas ν_0 varies from $10^{12}\,\text{Hz}$ to $10^{16}\,\text{Hz}$ and shows no clear dependence on the island size.

Effective activation barrier energy

In Fig. 6.5A, the experimentally determined effective activation barrier energy E_b is plotted as a function of the respective island diameter along the $[1\bar{1}0]$ direction, $N_{[1\bar{1}0]}$. Obviously E_b scales linearly with $N_{[1\bar{1}0]}$. In contrast to Fig. 6.5A, E_b is widely distributed when plotted as a function of the diameter along the [001] direction, as can be seen in Fig. 6.5B.

Neither along the $[1\bar{1}0]$ direction nor along the [001] direction is a quadratic dependence of $E_b(N_{\text{dia}})$ observed. Hence the model of a coherent rotation of all magnetic moments of the island is not applicable, and thermal magnetization reversal takes place via nucleation and propagation of a domain wall, with E_b increasing with the domain wall length and hence with the island diameter.

However, this model of magnetization reversal with an effective activation barrier energy that is equal to the domain wall energy $E_{b,\text{DW}}$ as given in Eq. 6.3 is not valid in detail. For a vanishing domain wall length, the respective energy $E_b(0)$ should also vanish, but from the experiment an energy barrier offset $E_0 = E_b(0) > 0$ is observed. Consequently, the proposed model is oversimplified, and an additional energy barrier contribution E_0 has to be taken into account that does not scale with the island diameter $N_{[1\bar{1}0]}$. As will be shown later in this
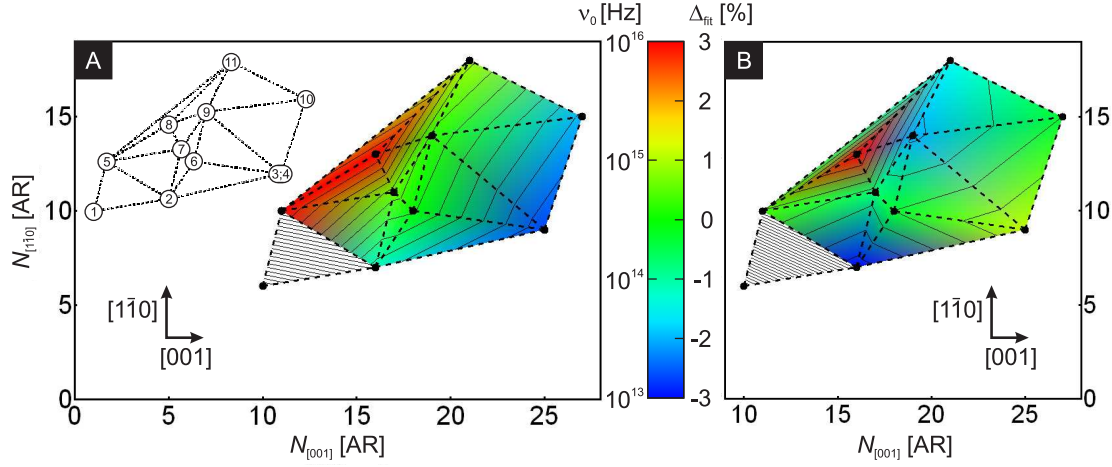
Figure 6.6: (**A**) Arrhenius prefactor ν_0 as a function of island dimension along the [001] and [1$\bar{1}$0] direction, respectively. Neglecting the data point for island "1", a gradient is visible in the color-coded distribution of ν_0 (see labeled mesh inset for island correlation). The data are fitted to a plane in the $(N_{[001]}, N_{[1\bar{1}0]}, \log[\nu_0/\nu_{\text{unit}}])$ space. (**B**) Color-coded relative deviation Δ_{fit} of the experimentally determined ν_0 from the fit.

chapter, this energy barrier offset E_0 can be attributed to the activation barrier energy E_{nuc} of a nucleus that initially has to reverse its magnetization to generate a domain wall.

Fitting the data with a linear function

$$E_{\text{b}} = E_0 + e_{\text{DW}} \cdot N_{[1\bar{1}0]}, \tag{6.4}$$

with E_0 being the energy offset and e_{DW} the domain wall energy per length (in AR), leads to $E_0 = (61 \pm 5)\,\text{meV}$ and $e_{\text{DW}} = (7.5 \pm 0.4)\,\text{meV}$.

To conclude, the effective activation barrier energy E_{b} only depends on the island dimension along the [1$\bar{1}$0] direction, and not along the [001] direction. From these experimental results one can directly deduce that the domain wall that moves through the island during the reversal process is oriented along the [1$\bar{1}$0] direction and therefore propagates along the [001] direction.

Arrhenius prefactor

In Fig. 6.6A, the experimentally determined prefactor ν_0 is plotted as a function of $N_{[001]}$ and $N_{[1\bar{1}0]}$ (note the logarithmic scale for ν_0). The labeled inset mesh helps to correlate each nanoisland to its respective data point. Adding a contour plot to the graph reveals that all data points (apart from the nanoisland labeled "1") seem to lie on a plane in the three-dimensional $(N_{[001]}, N_{[1\bar{1}0]}, \log_{10}[\nu_0/\nu_{\text{unit}}])$ space ($\nu_{\text{unit}} = 1\,\text{Hz}$), as indicated by the interpolated color gradient ranging from high ν_0 values (red) on the upper left to low values (blue) on the lower right of the

graph. Considering only the data points of nanoislands "2" to "11", this gradient is fitted to an apparent plane of the form

$$\nu_{\text{fit}}(N_{[001]}, N_{[1\bar{1}0]}) = 10^{c_0 + c_{[001]} \cdot N_{[001]} + c_{[1\bar{1}0]} \cdot N_{[1\bar{1}0]}} \, \text{Hz}, \tag{6.5}$$

leading to $c_0 = 16.3 \pm 0.4$, $c_{[001]} = -0.14 \pm 0.02$ and $c_{[1\bar{1}0]} = 0.12 \pm 0.03$. In Fig. 6.6B, the relative deviation

$$\Delta_{\text{fit}}(i) = \frac{\log_{10}[\nu_0(i)/\nu_{\text{unit}}] - \log_{10}[\nu_{\text{fit}}(N_{[001]}(i), N_{[1\bar{1}0]}(i))/\nu_{\text{unit}}]}{\log_{10}[\nu_{\text{fit}}(N_{[001]}(i), N_{[1\bar{1}0]}(i))/\nu_{\text{unit}}]}, \quad i = 1, \dots, 11 \tag{6.6}$$

of the experimentally determined data points $\nu_0(i)$ ($i = 2, \dots, 11$) from the respective apparent fitting plane $\nu_{\text{fit}}(N_{[001]}(i), N_{[1\bar{1}0]}(i))/\nu_{\text{unit}}$ is plotted. The fact that $|\Delta_{\text{fit}}| \leq 3\%$ indicates that the fit reproduces the experimental data very well – except for the nanoisland "1" with $\Delta_{\text{fit}} = -18\%$ (we will come back to this later). Consequently, the experimentally determined Arrhenius prefactor ν_0 can be described by

$$\nu_0 \approx 10^{16.3} \cdot 10^{-0.14 \cdot N_{[001]}} \cdot 10^{0.12 \cdot N_{[1\bar{1}0]}} \cdot \nu_{\text{unit}}. \tag{6.7}$$

6.4 Model for magnetization reversal of nanoislands

The detailed magnetization reversal may proceed via metastable states as described in the following (see Fig. 6.7A): From time to time, small patches at the [001] apex of the island try to switch their magnetization coherently. Once this nucleus is created, it is surrounded by a short domain wall (I). Because this configuration is energetically unfavorable, the nucleus and the domain wall are likely to annihilate again. In cases where the energy from the thermal bath is high enough, the domain wall can move through the whole nanoisland (II). If it is absorbed at its nucleation site, the initial single domain configuration will be restored, and no net magnetization reversal is observed. Magnetization reversal only occurs when the domain wall successfully propagates through the whole nanoisland and annihilates at the opposite side (III).

Once the domain wall is nucleated, it can be described as a quasiparticle diffusing through the nanoisland. Due to the absence of external forces, moving forward and backward is energetically degenerate (moving the domain wall does not cost energy), and therefore the possibility of moving one step back or one step forward within one short time interval is equal to 0.5. Following random walk theory for a particle moving inside a 1D box with absorbing walls [80], the mean distance covered after n steps scales with $\sqrt{n}$. Thus the probability of a domain wall diffusing successfully from one end of the island to the other decreases with increasing
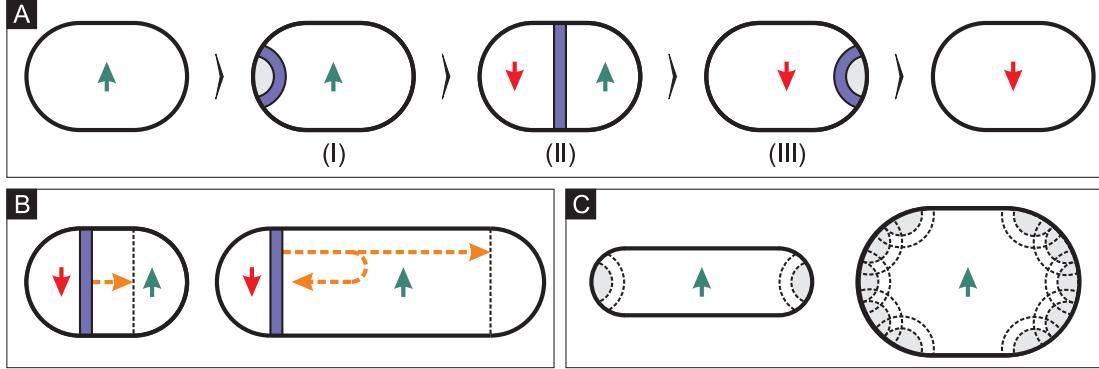
Figure 6.7: (**A**) Model of the thermal magnetization switching of a nanoisland, as deduced from the experimental findings: A domain wall is nucleated at one end of the island, propagates to the other end and annihilates again, leading to a net reversal of magnetization. (**B**) With increasing elongation of the nanoisland along the domain wall propagation direction, the probability of a domain wall rolling from one end to the other is decreased, leading to a decreased switching rate. (**C**) With increasing width of the nanoisland, the number of nucleation centers for a domain wall increases, leading to an increase of the switching rate.

dimension along the [001] direction, as shown in Fig. 6.7B. For very elongated islands, it is likely that the domain wall returns to its nucleation site (as indicated by the arrows) and will annihilate there, with no net magnetization reversal. Due to the time resolution of SP-STM neither the nucleation nor the domain wall motion can be observed. Consequently, only successful magnetization reversals are detected, and therefore the experimentally determined Arrhenius prefactor ν_0 decreases with increasing elongation of the nanoisland. This is reflected by the slight decrease of ν_0 in Fig. 6.6A when increasing $N_{[001]}$ and keeping $N_{[1\bar{1}0]}$ constant. The factor $10^{-0.14 \cdot N_{[001]}}$ in Eq. 6.7 may be interpreted as the probability of a magnetization reversal after successful nucleation of a domain wall.

To nucleate a domain wall that can diffuse through the nanoisland, the energy borrowed from the surrounding temperature bath has to be high enough to

- reverse all the spins of a critical activation volume V_{act} for nucleation, and simultaneously

- create a domain wall that extends through the maximum dimension along the [1$\bar{1}$0] direction of the nanoisland,

and therefore $E_{\text{b}} = E_{\text{nuc}} + E_{\text{DW}}$. From theoretical studies of thermally induced magnetization dynamics it is known that V_{act} depends on the exchange length $l_{\text{ex}} = \sqrt{\frac{A}{K}}$ [74–76, 81], which is a material parameter. Therefore, V_{act} is assumed to be approximately constant. With increasing diameter along the [1$\bar{1}$0] direction, the number of potential nucleation sites for magnetization reversal increases, as shown

in Fig. 6.7C. Thus every additional nucleation center increases the probability of magnetization reversal. Consequently, the experimentally determined Arrhenius prefactor ν_0 increases when increasing $N_{[1\bar{1}0]}$ while keeping $N_{[001]}$ constant, as can be seen from the fit in Fig. 6.6A. The factor $10^{0.12 \cdot N_{[1\bar{1}0]}}$ in Eq.6.7 describes the scaling of ν_0 with the diameter of the nanoisland along the $[1\bar{1}0]$ direction, $N_{[1\bar{1}0]}$.

To summarize, two opposing effects determine the prefactor ν_0, as revealed by the experiment: With increasing diameter along the $[001]$ direction, ν_0 increases, and with increasing diameter along the $[1\bar{1}0]$ direction, ν_0 decreases. Note that these dependencies are temperature-independent and therefore have no influence on the effective activation barrier energy $E_{\rm b}$, but only on the Arrhenius prefactor. The factor $10^{16.3}$ Hz in Eq.6.7 may be interpreted as the effective attempt frequency $\nu_{\rm act}$ of the spin ensemble inside the critical activation volume $V_{\rm act}$.

Regarding the smallest nanoisland "1", one may speculate that—due to its small size—the magnetic reversal of this island is driven by the coherent rotation of all magnetic moments rather than by the nucleation and propagation of a domain wall. The experimentally determined attempt frequency is $\nu_0 = (6.3^{+2.8}_{-0.5}) \times 10^{12}$ Hz. This value is slightly larger than the typical attempt frequencies resulting from experiments on superparamagnetic nanoparticles, with ν_0 being in the range of 10^9 Hz to 10^{11} Hz [82–85]. However, from our experiments on the Fe/W(110) nanoislands it is obvious that ν_0 is not a fixed material constant, but depends on the size and the shape of the nanoisland. In general, the attempt frequency depends on many parameters like external field, temperature, damping constant and magnetic properties [23].

As indicated by the experimental results for nanoisland "1", a cross-over from switching via the nucleation of a domain wall to the coherent rotation of the magnetic moments is expected with a further decrease of island size. New processes may play a non-negligible role for very small nanoislands, for example tunneling between magnetic states to reverse the magnetization. Future investigations of nanoislands consisting of less than 30 atoms will help to get a deeper insight into the reversal processes of nanoislands in this size regime.

6.5 Determination of exchange stiffness and magnetic anisotropy

Since both the domain wall energy $E_{\rm DW} \propto \sqrt{A \cdot K}$ and the domain wall width $w \propto \sqrt{A/K}$ depend on the exchange stiffness A and the magnetic anisotropy K, it is straightforward to determine these material parameters from the experimental results. The domain wall that propagates through the island cannot be resolved due to the limited time resolution of SP-STM, so stable domain walls on a single monolayer of Fe/W(110) have been investigated to determine w.
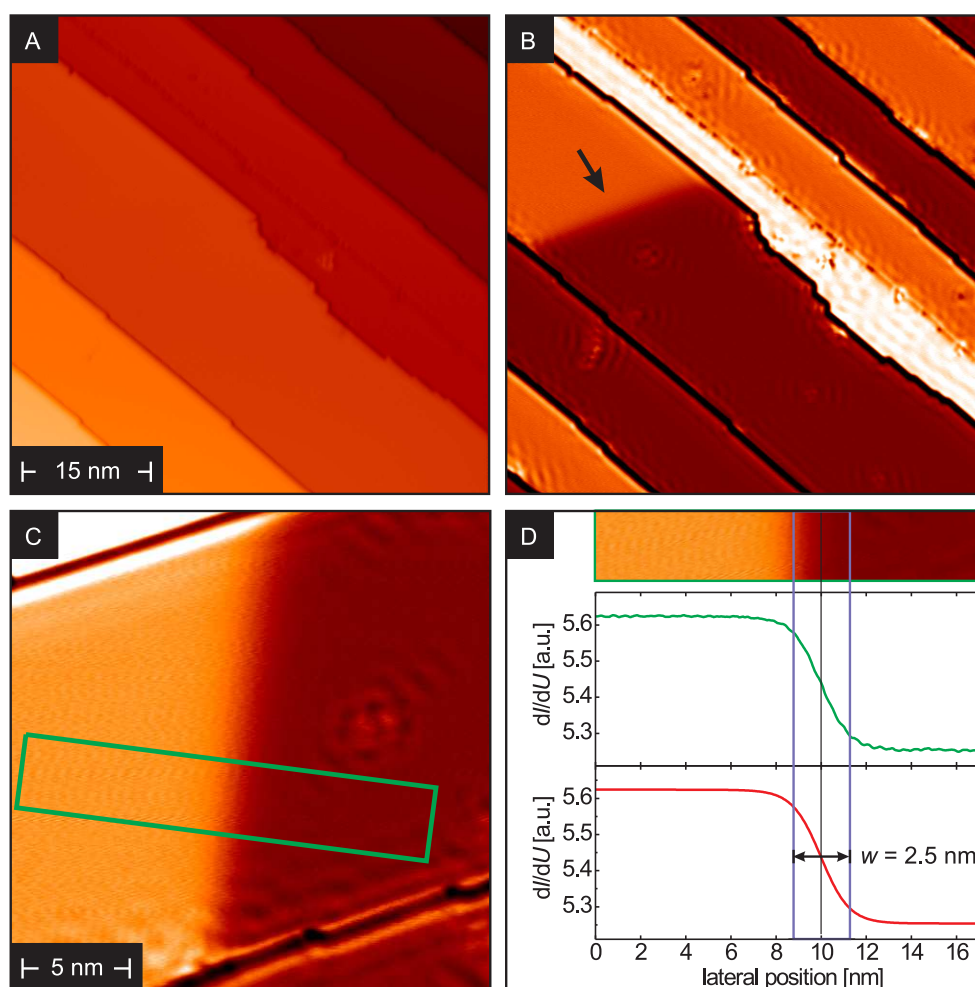
Figure 6.8: (A) Topography and (B) simultaneously obtained magnetic dI/dU map of a W(110) surface covered with about 1 ML Fe. In the magnetic map, a domain wall occurs within one Fe stripe (arrow). (C) Magnetic map of a zoom into the domain wall of (B). (D) Line section (upper panel) averaged within the area marked in (C) and respective domain wall fit (lower panel), leading to an estimated domain wall width $w \approx 2.5\,\mathrm{nm}$.

Monolayer domain wall width

In Fig. 6.8A, the topography of a Fe/W(110) sample with a coverage of approximately one monolayer is shown. Several terraces can be seen that are almost perfectly covered by a single iron monolayer. The magnetic contrast in the dI/dU map in Fig. 6.8B reflects the two possible magnetic states of the monolayer. Adjacent domains within the monolayer are separated by a domain wall, as marked by the arrow. Fig. 6.8C shows a zoom into that domain wall, and a line section across the area marked by the box is shown in Fig. 6.8D. The experimental data
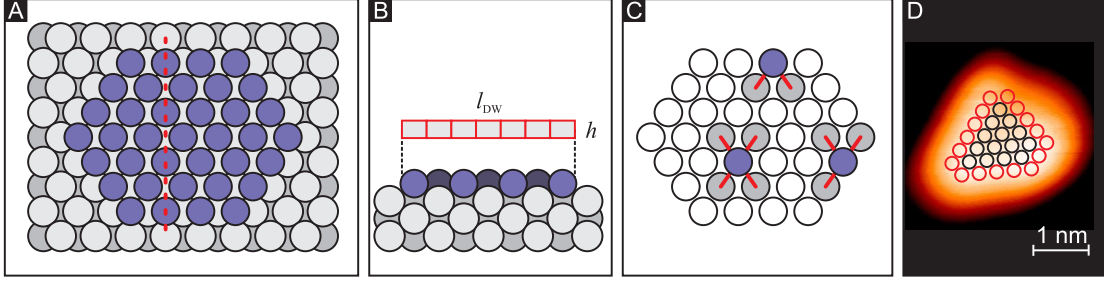
Figure 6.9: (**A**) Atomic composition of a typical Fe nanoisland on a W[110] substrate. (**B**) Line section along the dotted line in (A), and sketch of the domain wall area $S = l_{\mathrm{DW}} \cdot h$. (**C**) Nearest-neighbor exchange interaction of atoms at different positions of a nanoisland. Whereas center atoms have four nearest neighbors, atoms at the edge have only two or three. (**D**) Topography of nanoisland "1" and a superimposed atomic lattice to get a rough estimation of the atomic configuration. 14 center atoms (black circles) are surrounded by 17 rim atoms (red circles).

(green data points) are fitted with a domain wall profile (red line) of the form

$$y(x) = y_0 + y_{\mathrm{sp}} \cos \left(\arccos \left[\tanh \left(\frac{x - x_0}{w/2} \right) \right] + \phi \right), \qquad (6.8)$$

where $y(x)$ is the $\mathrm{d}I/\mathrm{d}U$ signal measured at position x, x_0 is the position of the domain wall, and y_0 and y_{sp} are the spin-averaged and spin-polarized $\mathrm{d}I/\mathrm{d}U$ signals, respectively. The angle between the magnetization axes of tip and sample is given by ϕ. From the fit, a domain wall width $w = 2.5\,\mathrm{nm}$ is derived.

The widths of several domain walls have been determined, revealing that w varies between $1.8\,\mathrm{nm}$ and $2.5\,\mathrm{nm}$. For the following considerations, an averaged domain wall width $w_{\mathrm{av}} = (2.15 \pm 0.35)\,\mathrm{nm}$ is assumed.

Center atoms of nanoislands

In Fig. 6.9A, the atomic composition of a typical nanoisland of compact shape is sketched in a top view. The maximum length of a domain wall that propagates through the island is given by the width of the island along the $[1\bar{1}0]$ direction. A section along the red dotted line is shown in Fig. 6.9B. It is clearly visible that the domain wall area S directly scales with the number of atomic rows $N_{[1\bar{1}0]}$ of the island. The length l_{DW} of the domain wall is given by $l_{\mathrm{DW}} = N_{[1\bar{1}0]} \cdot a/\sqrt{2}$ with a the lattice constant. The island height is $h = a/\sqrt{2}$, and hence, $S = l_{\mathrm{DW}} \cdot h = N_{[1\bar{1}0]} \cdot a^2/2$ ($a = 0.316\,\mathrm{nm}$ for W).

In classical micromagnetics, the domain wall energy $E_{\mathrm{DW}} = e_{\mathrm{DW}} \cdot N_{[1\bar{1}0]}$ and domain wall width w are given by $E_{\mathrm{DW}} = 4S\sqrt{AK}$ and $w = 2\sqrt{A/K}$. From the experiment, the domain wall energy per atomic row e_{DW} is given by

$$e_{\mathrm{DW}} = 2a^2\sqrt{AK} = (7.5 \pm 0.4)\,\mathrm{meV}. \qquad (6.9)$$

By combining e_{DW} and w_{av}, the parameters A and K can be determined separately:

$$A = \frac{1}{4a^2} \cdot e_{\text{DW}} \cdot w_{\text{av}} = (6.5 \pm 0.3) \times 10^{-12} \,\text{J/m}, \tag{6.10}$$

$$K = \frac{1}{a^2} \frac{e_{\text{DW}}}{w_{\text{av}}} = (5.6 \pm 0.3) \times 10^6 \,\text{J/m}^3 = (0.55 \pm 0.03) \,\text{meV/atom.} \tag{6.11}$$

Rim effects

In micromagnetics, the Heisenberg exchange energy E_{ex} per atom is described by [86]:

$$E_{\text{ex}} = -JS^2 \sum_{j=1}^{z} \left(\vec{\alpha} \cdot \frac{\partial^2 \vec{\alpha}}{\partial x^2} x_j^2 + \vec{\alpha} \cdot \frac{\partial^2 \vec{\alpha}}{\partial y^2} y_j^2 + \vec{\alpha} \cdot \frac{\partial^2 \vec{\alpha}}{\partial z^2} z_j^2 \right) \tag{6.12}$$

$$= \int_{V_{\text{atom}}} A \left\{ \left(\frac{\partial \vec{\alpha}}{\partial x} \right)^2 + \left(\frac{\partial \vec{\alpha}}{\partial y} \right)^2 + \left(\frac{\partial \vec{\alpha}}{\partial z} \right)^2 \right\} \mathrm{d}V. \tag{6.13}$$

Here, J is the exchange integral, S is the magnitude of the spin (in units of $\hbar$), $(x,y,z) = (\pm\frac{1}{2}a, \pm\frac{\sqrt{2}}{2}a, 0)$ denote the components of the distance $\vec{r}_j$ to the z nearest neighbors, and $\vec{\alpha}(\vec{r}_j)$ is a unit vector parallel to the spin at site j.

As can be seen from Eq. 6.12, the exchange energy E_{ex} scales with the number of nearest neighbors. Whereas inner atoms have four nearest neighbors ($z = 4$), atoms at the rim have only two (or three) nearest neighbors, as indicated in Fig. 6.9C. Consequently, the exchange energy E_{ex} is decreased by a factor of two for atoms at the rim.

To adapt the micromagnetic description of the domain wall energy E_{DW} to atoms that are located at the rim of a nanoisland, an effective exchange stiffness for the rim, $A_{\text{rim}} = A/2 = 3.25 \times 10^{-12} \,\text{J/m}$, is introduced. Additionally, the effective anisotropy K_{rim} of rim atoms is significantly increased due to the reduced coordination, as has been found experimentally for Co nanoislands on Pt(111) [87], where edge atoms exhibit a 20 times larger anisotropy energy than bulk and surface atoms.

To elaborate the rim effect for the Fe/W(110) nanoislands, two simple models have been applied. For both models, imagine a domain wall with a length $l = 2\,AR$, thus only consisting of rim atoms. From the fit of the experimental data, the effective activation barrier is given by $E_{\text{b}}(2) = E_0 + 2 \cdot e_{\text{DW}} = (76 \pm 5)\,\text{meV}$ (setting $N_{[1\bar{1}0]} = 2$ in Eq. 6.4).

In the first model, the experimentally determined effective activation barrier energy offset of $E_0 = (61 \pm 5)\,\text{meV}$ is totally caused by the increased anisotropy of the rim atoms, thereby neglecting any energy contribution of the nucleus activation energy E_{nuc} ($E_{\text{nuc},1} = 0\,\text{meV}$; the index "1" indicates the first model).

Consequently, the domain wall energy of the imaginary domain wall is given by $E_{\mathrm{DW},1} = E_{\mathrm{b}}(2)$, and the respective domain wall energy per rim atom is $e_{\mathrm{DW,rim},1} = 0.5 \cdot E_{\mathrm{b}}(2) = (38.0 \pm 2.5)\,\mathrm{meV}$. Thus, with $e_{\mathrm{DW,rim},1} = 2a^2 \sqrt{A_{\mathrm{rim}} K_{\mathrm{rim},1}}$ (cf. Eq. 6.9), the ratio between K and $K_{\mathrm{rim},1}$ can be calculated:

$$\frac{K_{\mathrm{rim},1}}{K} = 2 \left(\frac{e_{\mathrm{DW,rim}}}{e_{\mathrm{DW}}} \right)^2 = 51 \pm 9 \tag{6.14}$$

Hence, $K_{\mathrm{rim},1} = (28 \pm 5)\,\mathrm{meV/atom}$. This value is very large compared to the anisotropy K of the center atoms. The ratio $K_{\mathrm{rim},1}/K$ exceeds that of the Co/Pt(111) system [87] by factor of two.

In a second and more detailed model, the activation energy for the reversal of the nucleus E_{act} is also taken into account. Now, not only the increased anisotropy at the rim, but also the energy for coherent flipping of the magnetic moments inside the nucleus contributes to the experimentally determined energy barrier offset $E_0 = (61 \pm 5)\,\mathrm{meV}$, and consequently it is not possible to discriminate the two contribtions from the investigations of E_{b}. However, as has been indicated by the analysis of the Arrhenius prefactor, nanoisland "1" may switch via the coherent rotation of all magnetic moments rather than by the nucleation and propagation of a domain wall. Under this assumption, the total activation energy barrier for this particular island is given by the sum over the anisotropy energies of each atom of the island. Incorporating rim effects, E_{b} is given by the anisotropy contributions of the N_{rim} rim atoms (having the anisotropy constant $K_{\mathrm{rim},2}$) and the N_{center} atoms at the center of the island (with anisotropy constant K). The index "2" labels the second model. Hence, in analogy to Eq. 6.2:

$$E_{\mathrm{coh},2} = N_{\mathrm{rim}} \cdot K_{\mathrm{rim},2} + N_{\mathrm{center}} \cdot K. \tag{6.15}$$

In Fig. 6.8D, a scaled atomic lattice is superimposed on the topographic image of nanoisland "1". A very rough estimation yields that the island consists of 31 atoms, with 17 of them at the rim. Consequently, $N_{\mathrm{rim}} = 17$ and $N_{\mathrm{center}} = 14$. From the experiment, the effective activation energy barrier of the nanoisland is $E_{\mathrm{b}} = 103 \pm 3\,\mathrm{meV}$, and setting these values into Eq. 6.15 results in $K_{\mathrm{rim},2} = 5.6\,\mathrm{meV/atom}$, which is a factor of ten higher than the anisotropy constant K of center atoms.

Within this model, it is now possible to estimate the nucleus activation energy $E_{\mathrm{nuc},2}$ of nanoislands that switch their magnetization via the nucleation and propagation of a domain wall, using A, A_{rim}, K and $K_{\mathrm{rim},2}$. The domain wall energy $E_{\mathrm{DW},2}(2)$ of the imaginary domain wall with $l = 2\,\mathrm{AR}$ is then given by

$$E_{\mathrm{DW},2}(2) = 2 \cdot 2a^2 \sqrt{A_{\mathrm{rim}} K_{\mathrm{rim},2}} = 33.9\,\mathrm{meV}. \tag{6.16}$$

Consequently, the energy needed to reverse the magnetization of the nucleus is given by the difference of $E_{\mathrm{b}}(2)$ and $E_{\mathrm{DW},2}(2)$: $E_{\mathrm{nuc}} = E_{\mathrm{b}}(2) - E_{\mathrm{DW},2}(2) \approx 42\,\mathrm{meV}$.

Note that, depending on the size and shape of the nanoisland, the actual composition of the nucleus may vary due to the different anisotropy energy contributions of the center and rim atoms. The nucleus may either consist purely of about seven rim atoms or may be a combination of rim and center atoms.

Comparison to earlier work on Fe/W[110]

The experimental results of this work can be compared to the results of M. Pratzer *et al.* [71, 88], who studied the Fe/W(110) system by means of Kerr magnetometry and SP-STM. Instead of superparamagnetic nanoislands, their experiments were performed on W(110) substrates covered with about 1.5 atomic layers of iron, leading to a system of a closed ferromagnetic iron monolayer and second-layer stripes decorating the W step edges. Using Kerr magnetometry, a domain wall energy per atomic row $e_b = (15.2 \pm 1.5)$ meV was determined. Combination with the domain wall width $w = 0.6 \pm 0.2$ nm as derived from SP-STM experiments leads to an exchange stiffness $A = 3.6^{+2.2}_{-1.4} \times 10^{-12}$ J/m and a magnetic anisotropy $K = 40.6^{+26}_{-15.2} \times 10^6$ J/m^3 (4.2 meV/atom). Note that the values of A and K in Ref. [71] have been corrected in Ref. [88].

Obviously, e_b as well as w (and therefore also A and K) in [71] significantly deviate from the experimental results here. In our epxeriments, a domain wall energy $e_b = (7.5 \pm 0.4)$ meV per atomic row and a domain wall width of $w = (2.15 \pm 0.35)$ nm has been determined, leading to $A = (6.5 \pm 0.3) \times 10^{-12}$ J/m and $K = (5.6 \pm 0.3) \times 10^6$ J/m^3. Probably, this discrepancy to the results in Ref. [71] is a consequence of the different quality of the samples: Whereas the dI/dU map in Ref. [71] shows a considerable density of impurity atoms, the dI/dU map of a typical sample as prepared here indicates a very clean Fe monolayer, as shown in Fig. 6.8C, where every single impurity atom can be indentified by the surrounding standing wave pattern that originates from the scattering of an electronic surface state. For films having a lower quality, every non-magnetic impurity atom leads to a decoupling of the iron atoms, and this leads to a reduced domain wall energy and domain wall width.

To summarize, based on the investigation of the mean lifetime $\bar{\tau}$ between successive switching events of individual nanoislands at different temperatures, one gets insight into the microscopic reversal processes that are not directly observable with conventional SP-STM techniques. Combining the analysis of the Arrhenius-like switching behavior of the nanoislands and the determination of the domain wall width of a closed monolayer of Fe/W(110), the exchange stiffness A and anisotropy K for both the center atoms and the rim atoms in a nanoisland can be determined separately.

Chapter 7

Current-induced Magnetization Switching of Nanoislands

In the low-current regime of SP-STM, the distance Δz between a magnetic tip and the sample is typically several Å. When the tip is further approached to the surface, the spin-polarized current increases by orders of magnitude and therefore can exert a significant spin torque to the magnetization of a magnetic sample. Therefore, high spin-polarized currents should affect the switching behavior of nanoislands that frequently reverse their magnetization due to thermal agitation. In the following experiments, three main questions have been addressed:

- Is the junction between tip and sample still in the pure tunnel regime for µA tunnel currents?

- Does the electronic structure of the tunnel junction change significantly when the tip approaches the sample surface?

- What influence does a high spin-polarized tunnel current have on the switching behavior of magnetic nanoislands?

7.1   SP-STM in the high tunnel current regime

The z-displacement as a function of tunnel current with closed feedback loop at $U = -350\,\mathrm{mV}$ is shown in Fig.7.1A. A chromium coated W tip has been positioned above an individual Fe nanoisland, and the z-displacement of the tip was recorded while ramping the current I within the limits of the respective amplification ranges of the current-to-voltage amplifier. Obviously, the exponential behavior of $I(z)$ as derived from a simple one-dimensional model of tunneling [89] is experimentally confirmed over a wide range from low tunnel currents up to several µA. The tip lost material at $I \approx 8\,\mu\mathrm{A}$, resulting in a discontinuous step in the z-displacement (see the lower right of Fig.7.1A).
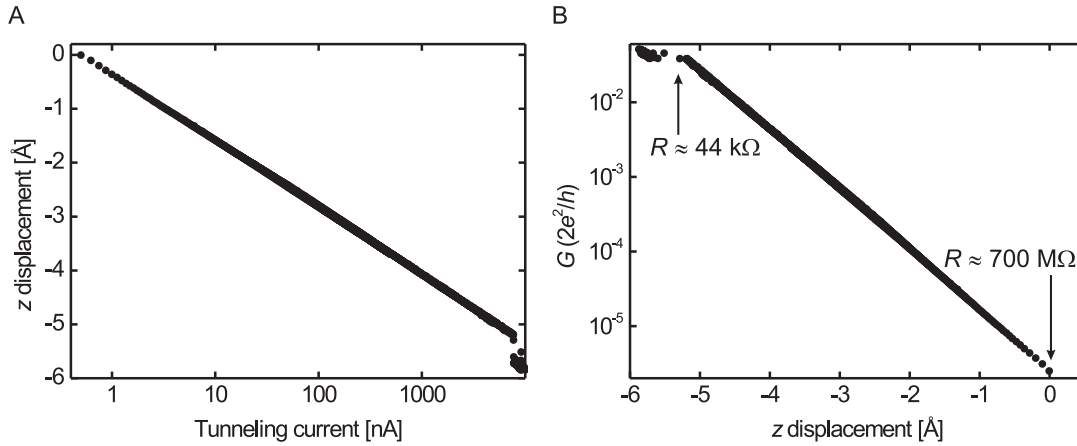
Figure 7.1: (**A**) z displacement as a function of tunnel current with closed feedback loop, taken with a Cr coated W tip positioned above an iron nanoisland ($U = -350\,\mathrm{mV}$). The exponential behavior of $z(I)$ in the tunneling regime is confirmed. Data were taken from low to high currents. At $I \approx 8\,\mu\mathrm{A}$ the tip lost material, resulting in a discontinuous step in z displacement on the lower right. (**B**) Respective conductance G in units of $R_\mathrm{c} = 2e^2/h$.

On further approaching the tip towards the surface, the junction will change from a tunneling to the point contact regime where new channels of conduction are opened due to ballistic transport. If the conduction channel associated with the formation of point contact is sufficiently narrow to be regarded as one-dimensional, a "constriction" resistance of

$$R_\mathrm{c} = \frac{h}{2e^2} = \frac{R_\mathrm{K}}{2} \approx 12\,900\,\Omega \tag{7.1}$$

can theoretically be derived [90], with $R_\mathrm{K} = h/e^2$ being the *von Klitzing constant*. As can be seen in Fig. 7.1B the conductance as function of z-displacement yields a minimum resistance on the order of $R_\mathrm{min} = U/I_\mathrm{max} \approx 44\,\mathrm{k}\Omega$ at $I = 8\,\mu\mathrm{A}$. Because this is a factor of four higher than R_c, it is reasonable to assume that the tip and the sample are in the tunneling regime even in the µA range.

From the tunnel conductance $G = I/U$, the apparent barrier height ϕ can be derived, since $G \propto \exp(-1.025\sqrt{\phi}z)$ [91]. Fitting the data shown in Fig.7.1B results in $\phi = (3.118 \pm 0.003)\,\mathrm{eV}$, which is a typical value for a metal tunnel junction [92].

Spin-polarized spectroscopy

To investigate how the tunnel junction is modified electronically when approaching the tip to the surface, spin-resolved scanning tunneling spectroscopy has been performed on a nanoisland that switches its magnetization due to thermal activation. An island with a low switching frequency has been chosen that allows SP-STS to
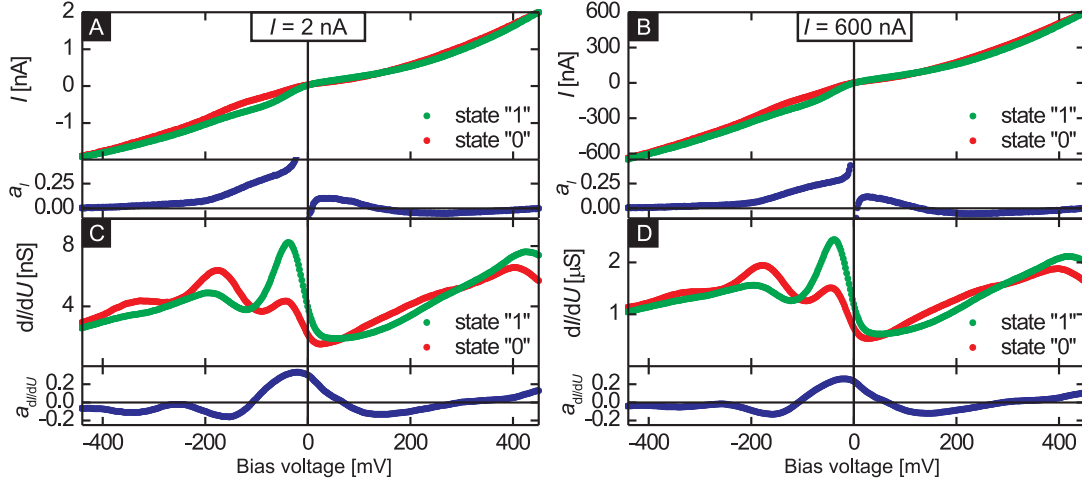
Figure 7.2: Spin-polarized spectroscopy performed on a nanoisland that thermally switches its magnetization state. A Cr coated W tip has been used with an open feedback loop (stabilizing bias $U_{stab} = +450\,$mV). (**A**) $I(U)$ at $I = 2\,$nA, measured during the magnetization state "0" (red) and "1" (green), and respective asymmetry a_I (blue). (**B**) Same as in (A), but at $I_{stab} = 600\,$nA. (**C**) Differential conductance $dI/dU(U)$ at $I = 2\,$nA, measured by means of Lock-In technique (modulation amplitude $U_{mod} = 20\,$mV, modulation frequency $f = 4.333\,$kHz). Red (green) data points denote the magnetization of the island being in the state "0" ("1"). The repective dI/dU asymmetry is plotted in the bottom row (blue). (**D**) Same as in (C), but at $I_{stab} = 600\,$nA. The spectroscopic features and therefore the electronic configuration of the tunnel junction does not change significantly upon increasing the current.

be performed on the same island with both magnetic configurations: in the parallel and in the antiparallel magnetization configuration. The results are shown in Fig. 7.2. The $I(U)$ curves recorded at low ($I = 2\,$nA) and high ($I = 600\,$nA) tunnel current and the respective asymmetry $a_I(U) = (I_1(U) - I_0(U))/(I_1(U) + I_0(U))$ are shown in (A) and (B). Here, $I_0(U)$ and $I_1(U)$ denote the tunnel current $I(U)$ taken on the island in the magnetic state "0" or "1". By definition, state "0" is related to a low dI/dU signal at $U = -200\,$mV, and state "1" is related to a high dI/dU signal at the same bias. In Fig. 7.2C and D the differential conductance $dI/dU(U)$ and the respective asymmetry $a_{dI/dU}(U) = [dI_1/dU - dI_0/dU]/[dI_1/dU + dI_0/dU](U)$ are plotted for the low and high tunnel current regimes.

Although the scaling of $I(U)$ and $dI/dU(U)$ changes by a factor of 300 when increasing the setpoint current from $I = 2\,$nA to $I = 600\,$nA, it is obvious that the spectroscopy curves of both current regimes are qualitatively very similar. The same applies to the curves of the differential tunnel conductance $dI/dU(U)$. A peak at about $+400\,$mV which is characteristic for an Fe monolayer on W(110) [93] can be observed, while features at negative bias are mainly connected to tip states and therefore may depend on the particular tip that is used in the experiment.
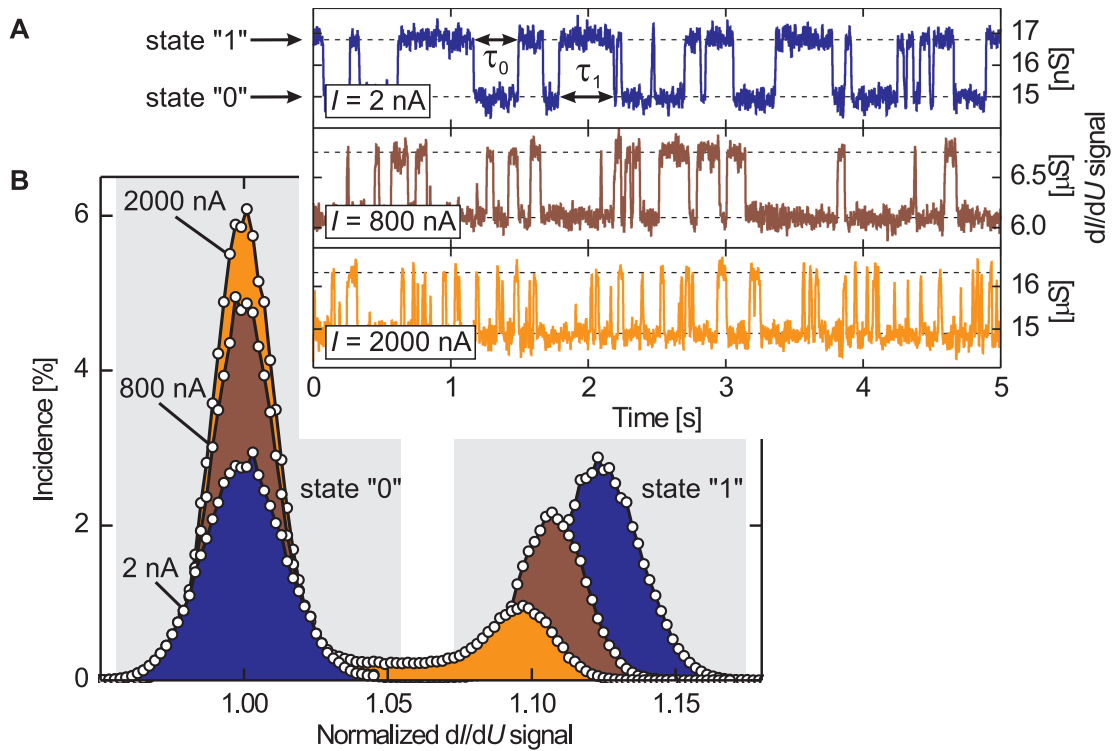
Figure 7.3: (**A**) Trace of the time-dependent magnetic dI/dU signal of one particular nanoisland (island area: $(5.7 \pm 0.4)\,nm^2$) recorded at different tunnel currents I ($T = 48.4\,K$, $U = -200\,mV$). (**B**) Histogram of the overall magnetic dI/dU signal normalized with respect to the state "0" level at different tunnel currents. Whereas state "0" and state "1" are equally populated at low currents, a substantial asymmetry toward state "0" is found at high currents.

Obviously, increasing the current from $2\,nA$ to $600\,nA$ does not have a significant influence on the electronic structure of the tunnel junction. Hence, the same electronic states predominantly contribute to the tunnel current in both the low and high tunnel current regimes.

7.2   Spin torque effects on thermally switching nanoislands

To investigate the effects of spin-polarized currents on the switching behavior, the magnetic dI/dU signal has been recorded as a function of time with the tip positioned stationary above the central region of small Fe nanoislands with a typical surface area of $7\,nm^2$, i.e. consisting of about 100 atoms. All measurements have been performed in the constant-current mode with different tunnel currents obtained by adjusting the tip-sample distance.

For example, the traces in the panels of Fig. 7.3A show the first 5 s of the spin-resolved dI/dU signal measured on one particular island at tunnel currents $I = 2\,$nA, 800$\,$nA, and 2000$\,$nA. The dI/dU signal abruptly changes between two discrete levels, thereby reflecting the switching behavior of the nanoisland that reverses its magnetization from state "0" (low level) to state "1" (high level) and vice versa. At low tunnel current, the island statistically switches its magnetization between the two states, revealing no preferential magnetization orientation. This is expected, because the two magnetization states are energetically degenerate and therefore should be populated equally. However, when increasing the tunnel current to 800$\,$nA, the magnetization slightly prefers to be in the state "0", as reflected by the dI/dU signal. This imbalance of the population increases when setting a tunnel current of $I = 2000\,$nA, as shown in the bottom panel of Fig. 7.3A. Now, the dI/dU signal remains at the lower level most of the time, and distinct peaks indicate short switching events that change the magnetization of the island from state "0" to state "1" and immediately back to state "0".

Fig. 7.3B shows the histograms of the magnetic dI/dU signal recorded over a much longer period (700$\,$s), normalized to the lower level at the different tunneling currents. At a low tunnel current, the histogram reveals that both states occur with the same probability, as indicated by the same area of the two peaks of state "0" and state "1". As I increases, however, an imbalance between states "0" and "1" builds up until one state clearly dominates, as shown for $I = 2000\,$nA: The area covered by peak of state "0" (A_0) is much smaller than the area under the peak of state "1" (A_1). Furthermore, with increasing tunnel current, a slight shifting of the peak of state "1" towards the peak of state "0" is observed, reflecting a decreasing dI/dU signal contrast. This decrease might be caused by a distance-dependent polarization of the electronic states involved in the tunneling process.

To summarize the experimental finding, spin-polarized tunnel currents lead to a splitting of the two (otherwise degenerate) effective activation barriers separating the two magnetization states. To quantify this imbalance, each of the histogram peaks was fitted by a Gaussian with the Area $A_{0,1}$. By defining the histogram asymmetry

$$a_{\mathrm{H}} \equiv \frac{A_1 - A_0}{A_1 + A_0}, \tag{7.2}$$

asymmetries of $a_{\mathrm{H}} = (-0.7 \pm 0.5)\%$, $(-39.4 \pm 0.7)\%$ and $(-74 \pm 1)\%$ for $I = 2\,$nA, 800$\,$nA and 2000$\,$nA were observed. Obviously, a high spin-polarized tunnel current injected from a magnetic tip forces a thermally switching nanoisland to favor one of the degenerate magnetic states.

7.3   Bias-dependent spin-torque

It is known from theory [94] as well as from experiments on magnetic nanopillars [5] that the spin torque changes sign when reversing the spin current direction. To switch the magnetization back and forth, we investigated the switching behavior as a function of sample bias at $I = 600\,\text{nA}$.

In order to characterize the tip, the magnetic $\mathrm{d}I/\mathrm{d}U$ signal as a function of bias voltage has been recorded on one particular nanoisland with low switching frequency using spin-polarized tunneling spectroscopy with a closed feedback loop. Nanoislands that have a very low switching frequency with a mean lifetime on the order of a minute make it possible to perform spectroscopy on one single system for both the parallel and antiparallel configuration of tip and sample magnetization. To check the magnetic state of a nanoisland, the $\mathrm{d}I/\mathrm{d}U$ signal is recorded before and after every single spectroscopy curve. Therefore, spectroscopic features can be directly correlated to the respective sample magnetization configuration. Note that in general, on static magnetic samples with a local variation of the magnetization, the tip has to be moved to a different site on the sample to perform spin-resolved spectroscopy, and local variations of the electronic structure of a sample may cause features that are not only related to the different magnetic configuration. In our experiments on thermally switching nanoislands, changes in the electronic structure can be excluded.

The $\mathrm{d}I/\mathrm{d}U$ asymmetry

$$a_{\mathrm{d}I/\mathrm{d}U} = \frac{\mathrm{d}I/\mathrm{d}U(\uparrow\uparrow) - \mathrm{d}I/\mathrm{d}U(\uparrow\downarrow)}{\mathrm{d}I/\mathrm{d}U(\uparrow\uparrow) + \mathrm{d}I/\mathrm{d}U(\uparrow\downarrow)} \tag{7.3}$$

serves as a measure for the magnetic signal contrast: If $a_{\mathrm{d}I/\mathrm{d}U}$ is zero, no magnetic contrast is observed, and for $a_{\mathrm{d}I/\mathrm{d}U} \neq 0$ the $\mathrm{d}I/\mathrm{d}U$ signal changes, depending on the relative orientation of the tip and sample magnetization.

The $\mathrm{d}I/\mathrm{d}U$ asymmetry $a_{\mathrm{d}I/\mathrm{d}U}(U)$ is plotted in Fig. 7.4A both for a low current of $I = 2\,\text{nA}$ (blue) and a high current of $I = 600\,\text{nA}$ (orange), respectively. To avoid tip crashes at zero bias, a window around $U = 0\,\text{mV}$ has been excluded. Note that $a_{\mathrm{d}I/\mathrm{d}U}$ can change sign when varying the bias voltage U, as can be seen for $U \geq 250\,\text{mV}$ in the positive bias regime in Fig. 7.4A. This is attributed to the fact that the $\mathrm{d}I/\mathrm{d}U(U)$ signal is related to the spin "up" and spin "down" density of electronic states involved in the tunneling process at given bias U.

As can be seen from the graph, $a_{\mathrm{d}I/\mathrm{d}U}(U)$ is positive over a wide range of bias voltages. As a convention, islands showing a high $\mathrm{d}I/\mathrm{d}U$ signal at negative bias (appearing "bright" in magnetic maps) are in the state "1", whereas a low ("dark") $\mathrm{d}I/\mathrm{d}U$ signal at $U < 0$ is related to the magnetic state "0". Obviously, the contrast is not inverted when inverting the bias voltage from -200 mV to +200 mV: "bright" islands remain "bright" when changing sign of the voltage, and "dark" islands remain "dark". Therefore, the $\mathrm{d}I/\mathrm{d}U$ signal can be used to determine directly the
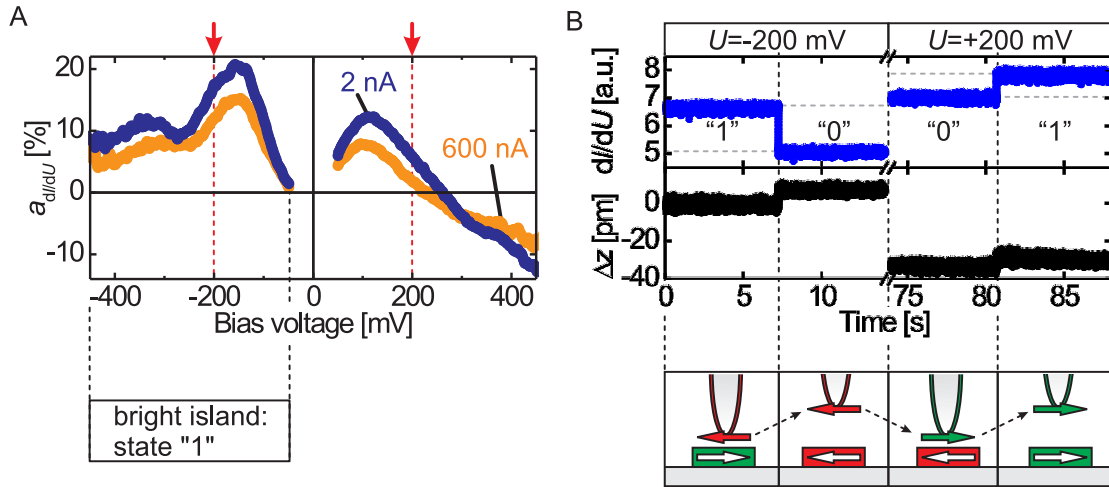
Figure 7.4: (**A**) Magnetic contrast $a_{\mathrm{d}I/\mathrm{d}U}$ as a function of bias voltage for tunnel currents of $I = 2\,\mathrm{nA}$ and $I = 600\,\mathrm{nA}$. No change of contrast is expected when changing the bias voltage from -200 mV to +200 mV – this means, that a "bright" island at negative bias appears "bright" at positive bias. Only for voltages exceeding 250 mV is a change in contrast expected. (**B**) Section of the $\mathrm{d}I/\mathrm{d}U$ signal and the respective change in tip-sample distance Δz with a closed feedback loop. After the first switching event the bias voltage has been inverted from $U = -200\,\mathrm{mV}$ to $U = +200\,\mathrm{mV}$. The next switching event is observed at positive bias, and the respective tip displacement Δz indicates that the total spin polarization of the current is reversed.

magnetic state ("0" or "1") of an island.

A section of the $\mathrm{d}I/\mathrm{d}U$ signal and the respective change in tip-sample distance Δz on the same island at low tunnel current and closed feedback loop is shown in Fig. 7.4B. Initially, the island is in the state "1", as reflected by the high $\mathrm{d}I/\mathrm{d}U$ signal. The applied bias voltage is $U = -200\,\mathrm{mV}$, therefore, electrons are tunneling from the sample into the tip. After some seconds a spontaneous switching event is recorded, as can be seen both from the change of the $\mathrm{d}I/\mathrm{d}U$ signal and the tip displacement Δz. The tip has been retracted some picometers, and this indicates that the magnetic tunnel junction changed from antiparallel to parallel configuration. The magnetization of the island remains stable over a period of about 60 seconds, and within this time the bias between the tip and the sample has changed to $U = +200\,\mathrm{mV}$, leading to a Δz displacement of the tip and a changed $\mathrm{d}I/\mathrm{d}U$ signal due to the different tunnel conditions. Now, electrons are tunneling from the tip to the sample. Then, a second switching event is observed. The $\mathrm{d}I/\mathrm{d}U$ signal increases to a higher level – consequently, the island has switched back from state "0" to state "1". Simultaneously, the tip has been rectracted by a few picometer, again indicating that the magnetic tunnel junction changed from antiparallel to parallel configuration. This finding indicates that the total spin polarization of the tunnel current is inverted when inverting the bias voltage. The respective tip-sample magnetization configurations are indicated in
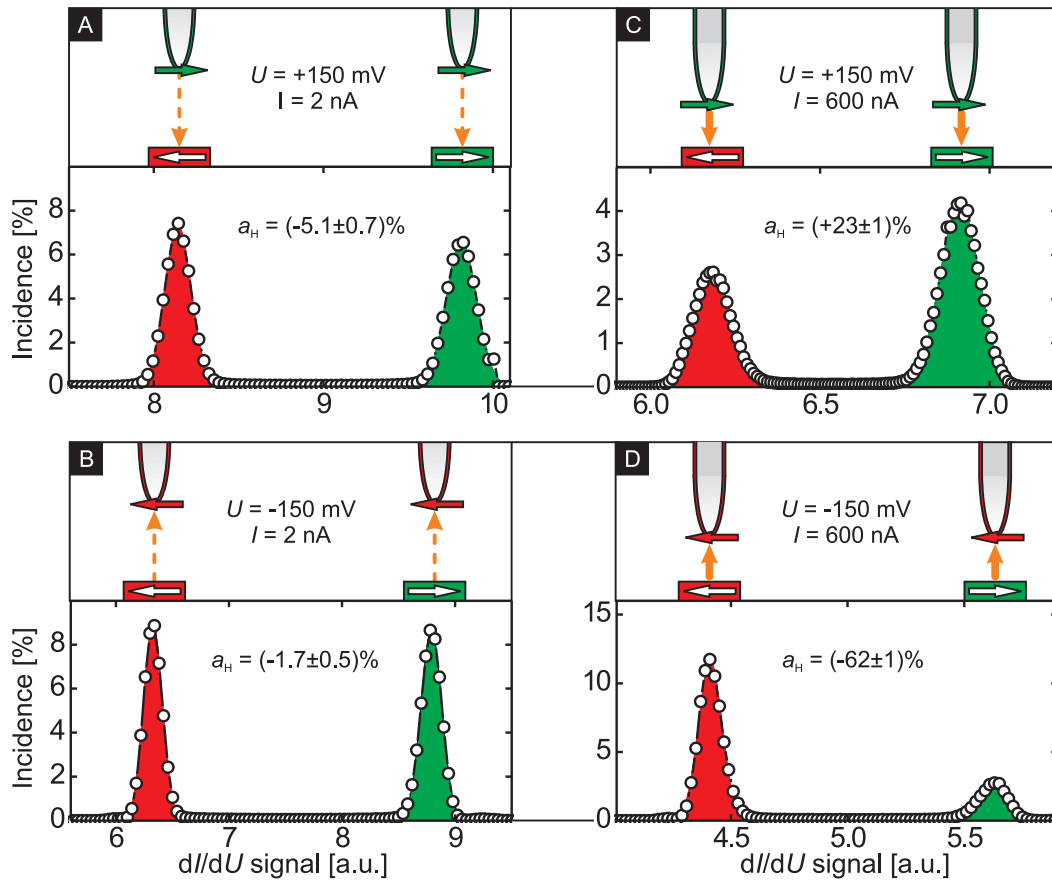
Figure 7.5: Histograms of the magnetic dI/dU signal measured at low (**A**),(**B**) and high (**C**),(**D**) current (island area: $(8.6 \pm 0.5)\,\mathrm{nm}^2$, $T = 55.9\,\mathrm{K}$). The bias voltage is $U = +150\,\mathrm{mV}$ for (A),(C) and $U = -150\,\mathrm{mV}$ for (B),(D). While only a very low histogram asymmetry a_H is observed at low tunnel current, high asymmetries were found at high tunnel current, and the sign of the asymmetry depends on the current direction.

the lower panel of Fig. 7.4B.

Using the same tip, the bias-dependent switching behavior of a nanoisland with a higher thermal switching frequency has been investigated. Fig. 7.5 shows histograms of the magnetic dI/dU signal measured on the particular island at a relatively low tunnel current of $I = 2\,\mathrm{nA}$ (A and B) and a much higher current of $600\,\mathrm{nA}$ (C and D). While the data of Fig. 7.5A and C were taken at positive sample bias, $U = +150\,\mathrm{mV}$, i.e. with I flowing from the tip to the sample, B and D were obtained with the opposite current direction at $U = -150\,\mathrm{mV}$.

At low current, irrespective of the current direction, a small negative histogram asymmetry a_H is observed. This may be the effect of a small residual magnetic stray field due to uncompensated spins at the Cr tip apex. In contrast, the histograms measured at higher tunnel currents of $600\,\mathrm{nA}$ (C and D) exhibit much
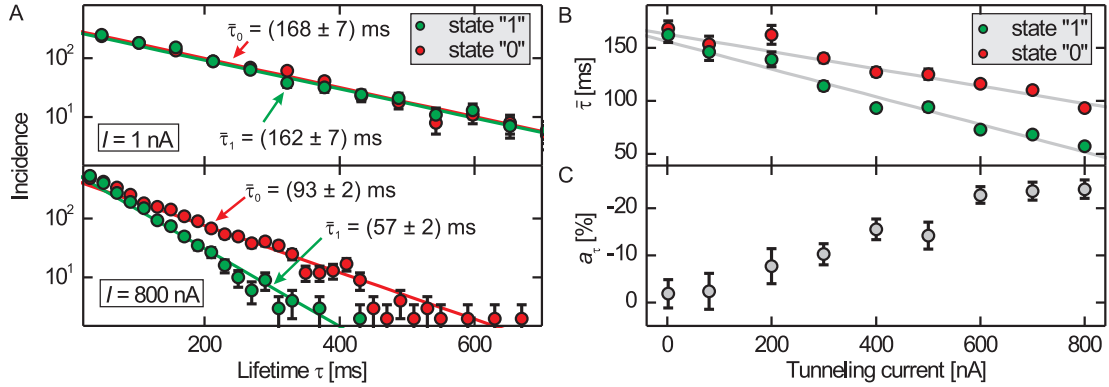
Figure 7.6: (**A**) Histograms of the lifetimes τ_0 and τ_1 of states "0" and "1" measured at $I = 1\,\text{nA}$ (top panel) and at $I = 800\,\text{nA}$ (bottom panel) ($T = 50.6\,\text{K}$, $U = -200\,\text{mV}$, $E_b = (133 \pm 4)\,\text{meV}$; island area: $(5.5 \pm 0.4)\,\text{nm}^2$). A decay function was fitted to the experimental data (lines) resulting in the mean lifetime $\bar{\tau}_{0,1}$. (**B**) Tunnel current dependence of the mean lifetimes $\bar{\tau}_{0,1}$ (gray lines are guides to the eye) and (**C**) the mean lifetime asymmetry a_τ.

higher asymmetries. Hence, in agreement with the experiments on lithographically prepared nanopillars, the sign of the asymmetry depends on the polarity of the tunnel junction: while a positive asymmetry $a_H = (+23 \pm 1)\%$ is observed for $U = +150\,\text{mV}$, we obtain $a_H = (-62 \pm 1)\%$ for $U = -150\,\text{mV}$.

On the same island using the same SP-STM tip the tunnel current has been repeatedly changed between low and high currents as well as between positive and negative bias voltage, and the results of Fig. 7.5A-D have been reproduced. Therefore, irreproducible changes of tunneling conditions such as accidental tip changes can be excluded.

7.4 Separation of Joule heating and spin torque contributions

A statistical analysis of the lifetimes of states "0" and "1", τ_0 and τ_1 has been performed to elaborate Joule heating and spin torque contributions. Plotting the incidence of τ_0 and τ_1 as a function of the lifetimes results in a state-resolved lifetime histogram of the nanoisland, as shown in Fig. 7.6A for a low tunnel current of $I = 1\,\text{nA}$ in the top panel. Fitting with an exponential decay law results in the respective mean lifetimes $\bar{\tau}_0$ for state "0" and $\bar{\tau}_1$ for state "1". Obviously, $\bar{\tau}_0 = \bar{\tau}_1$ at low tunnel currents. This is as expected since both states are energetically degenerate.

The lifetime histograms for a high tunnel current of $I = 800\,\text{nA}$ is shown in the bottom panel of Fig. 7.6A, using the same tip on the same nanoisland. In contrast to the low current regime, a different behavior is observed: At high tunnel current,
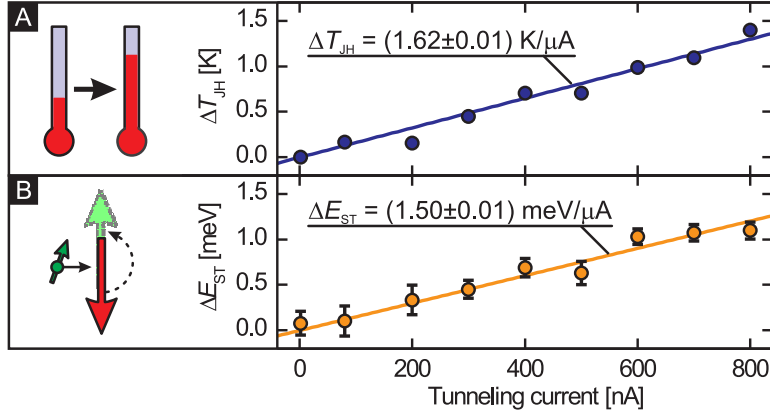
Figure 7.7: Experimentally determined Joule heating ΔT_{JH} (**A**) and spin torque effect ΔE_{ST} (**B**)as a function of the tunnel current I. Both show a linear dependence on I.

state "0" has a much higher mean lifetime than state "1". Consequently, the mean lifetime is found to depend strongly on the relative magnetization directions of the tip and the sample.

Plotting $\bar{\tau}_0$ and $\bar{\tau}_1$ as a function of the different tunnel currents between $1\,\mathrm{nA}$ and $800\,\mathrm{nA}$ reveals a trend from equal lifetimes at low current to an imbalance at high current, as shown in Fig. 7.6B. Two effects can be observed with increasing current: The mean lifetime of both states decreases with increasing current, and an additional asymmetry in the mean lifetimes evolves. The first effect can be attributed to Joule heating ΔT_{JH} of the island due to the high tunnel current, while the lifetime asymmetry has its origin in the spin torque effect that increases or decreases E_{b} by ΔE_{ST} due to the spin-polarized current. The lifetime asymmetry is defined by

$$a_\tau \equiv \frac{\bar{\tau}_1 - \bar{\tau}_0}{\bar{\tau}_1 + \bar{\tau}_0}. \tag{7.4}$$

Note that a_τ is equivalent to the histogram asymmetry a_{H}, since $A_1/A_0 = \bar{\tau}_1/\bar{\tau}_0$ (c.f. Eq. 7.2). In Fig. 7.6C, a_τ is plotted as a function of the tunnel current I. At low I, $a_\tau = 0$. With increasing I, a_τ also increases, and values of up to -25% for $I = 800\,\mathrm{nA}$ were obtained (Fig. 7.6C).

Joule heating

Knowing the mean lifetimes $\bar{\tau}_0$ and $\bar{\tau}_1$ allows the Joule heating and spin torque contributions to be determined quantitatively. From the ratio of the products of the respective mean lifetimes at high ($\bar{\tau}_{0,\mathrm{high}}$, $\bar{\tau}_{1,\mathrm{high}}$) and low current ($\bar{\tau}_{0,\mathrm{low}}$, $\bar{\tau}_{1,\mathrm{low}}$)

the temperature increase due to Joule heating ΔT_{JH} can be calculated:

$$\frac{\bar{\tau}_{0,\mathrm{high}} \cdot \bar{\tau}_{1,\mathrm{high}}}{\bar{\tau}_{0,\mathrm{low}} \cdot \bar{\tau}_{1,\mathrm{low}}} = \exp\left[\frac{2E_{\mathrm{b}}}{k_{\mathrm{B}}(T + \Delta T_{\mathrm{JH}})} - \frac{2E_{\mathrm{b}}}{k_{\mathrm{B}}T}\right]$$

$$\Rightarrow \Delta T_{\mathrm{JH}} = T \cdot \left[\left(1 + \frac{k_{\mathrm{B}}T}{2E_{\mathrm{b}}} \ln \frac{\bar{\tau}_{0,\mathrm{high}} \cdot \bar{\tau}_{1,\mathrm{high}}}{\bar{\tau}_{0,\mathrm{low}} \cdot \bar{\tau}_{1,\mathrm{low}}}\right)^{-1} - 1\right]. \qquad (7.5)$$

In Fig. 7.7A, ΔT_{JH} is plotted as a function of the tunnel current I, based on the experimentally determined mean lifetimes.

To estimate the Joule heating temperature rise from a theoretical point of view, a simple model [95] was applied. A half sphere of radius r is considered at an initial temperature of $0\,\mathrm{K}$. When the energy $E_{\mathrm{J}} = U \cdot I \cdot t$ is dissipated within the half sphere at a constant rate A per unit time t and unit volume V,

$$A = \frac{E_{\mathrm{J}}}{Vt} = \frac{3}{2}\frac{UI}{\pi r^3}, \qquad (7.6)$$

the temperature T inside the half sphere of thermal conductance λ is given by

$$T = \frac{r^2 A}{\lambda} = \frac{3}{2\pi}\frac{UI}{\lambda r}. \qquad (7.7)$$

Assuming the energy of the tunneling electrons is dissipated within a radius r of about 1 to $2\,\mathrm{nm}$, which is in rough agreement with known values of the inelastic mean free path of electrons [96], the simple model using $\lambda = 170\,\mathrm{W/mK}$ [56] indicates a temperature rise of 0.2 to $0.5\,\mathrm{K}$ for $I = 800\,\mathrm{nA}$. The experimentally determined Joule heating effect is a factor of three higher than that estimated using this model. Maybe the model is too simple—however, the linear dependence of ΔT_{JH} on the tunnel current I is clearly visible in Fig. 7.7A.

An experimental study of heat generation in a metal-vacuum-metal tunnel junction between an STM tip and a metallic sample has been performed, demonstrating that the Joule heat dissipated in the sample scales linearly with the tunnel current at constant bias voltage [97]. Consequently, both the simple model and the experiments in the STM configuration indicate that the temperature increase ΔT_{JH} scales linearly with I, and fitting the experimental data in Fig. 7.7A results in $\Delta T_{\mathrm{JH}}(I) = I \cdot (1.62 \pm 0.01)\,\mathrm{K/\mu A}$. This corresponds to an effective reduction of the activation energy barrier E_{b} of approximately $4\,\mathrm{meV}$ for $I = 1\,\mu\mathrm{A}$ at $T = 50.6\,\mathrm{K}$.

Spin torque

Knowing $\Delta T_{\mathrm{JH}}(I)$, the respective change $\Delta E_{\mathrm{ST}}(I)$ that modifies the effective activation barrier E_{b} to $E_{\mathrm{b}} \pm \Delta E_{\mathrm{ST}}$ can be calculated, using the mean lifetimes $\bar{\tau}_{0,\mathrm{high}}$

and $\bar{\tau}_{1,\mathrm{high}}$ in the high tunnel current regime:

$$
\begin{aligned}
\frac{\bar{\tau}_{1,\mathrm{high}}}{\bar{\tau}_{0,\mathrm{high}}} &= \exp\left[\frac{2\Delta E_{\mathrm{ST}}}{k_{\mathrm{B}}(T + \Delta T_{\mathrm{JH}})}\right] \\
\Rightarrow \Delta E_{\mathrm{ST}} &= \frac{k_{\mathrm{B}}(T + \Delta T_{\mathrm{JH}})}{2} \ln \frac{\bar{\tau}_{1,\mathrm{high}}}{\bar{\tau}_{0,\mathrm{high}}}.
\end{aligned}
\tag{7.8}
$$

The spin torque contribution ΔE_{ST} is plotted as a function of the tunnel current I in Fig. 7.7B. A linear dependence of ΔE_{ST} on I is clearly visible, and this is as expected from the macro spin model with finite-temperature effects described in Sec. 2.3. Fitting the data results in $\Delta E_{\mathrm{ST}} = I \cdot (1.50 \pm 0.01)\,\mathrm{meV}/\mu\mathrm{A}$.

Neglecting Joule heating effects, the mean lifetime $\tau_{0,1}$ as a function of the current I can be expressed as (cf. Eq. 2.22):

$$
\bar{\tau}_{0,1} = \nu_{\mathrm{a}}^{-1} \exp\left[\frac{E_{\mathrm{b}}}{k_{\mathrm{B}}T}\left(1 - \frac{I}{I_{\mathrm{c}}}\right)\right],
\tag{7.9}
$$

where ν_{a} is the attempt frequency and I_{c} denotes the threshold current to switch the magnetization at $T = 0\,\mathrm{K}$.

The effective activation barrier E_{b} can be derived from the mean lifetime $\bar{\tau}(T)$ measured at two different temperatures T_1 and T_2 and low tunnel current $I \ll I_{\mathrm{c}}$:

$$
E_{\mathrm{b}} = k_{\mathrm{B}} \cdot \frac{T_1 T_2}{T_2 - T_1} \cdot \ln \frac{\bar{\tau}(T_1)}{\bar{\tau}(T_2)}.
\tag{7.10}
$$

For the particular island in Fig. 7.6, $E_{\mathrm{b}} = (133 \pm 4)\,\mathrm{meV}$. Fitting the experimentally determined lifetime asymmetry a_{τ} to

$$
a_{\tau} = \tanh\left(\frac{E_{\mathrm{b}}}{k_{\mathrm{B}}T} \cdot \frac{I}{I_{\mathrm{c}}}\right)
\tag{7.11}
$$

leads to a threshold current $I_{\mathrm{c}} = (89 \pm 4)\,\mu\mathrm{A}$. This current would be necessary to switch the nanoisland at a temperature of $T = 0\,\mathrm{K}$ using the pure spin torque effect. Such high currents are not realizable within the tunneling regime—however, Joule heating plays an important role, hence one has to consider the combined action of the Joule heating ΔT_{JH} and the spin torque effect ΔE_{ST}.

Considerations for potential data storage applications

For potential applications in data storage devices every nanoisland that represents one bit has to be thermally stable for over ten years. On the other hand, switching the magnetization must be realized within milliseconds for fast writing performance. Consequently, the investigated nanoisland would have to be cooled down to T_{stable} to exhibit a stable magnetization over $\bar{\tau}_{\mathrm{stable}} = 10\,\mathrm{ys} \approx 3 \times 10^8\,\mathrm{s}$.

A

B
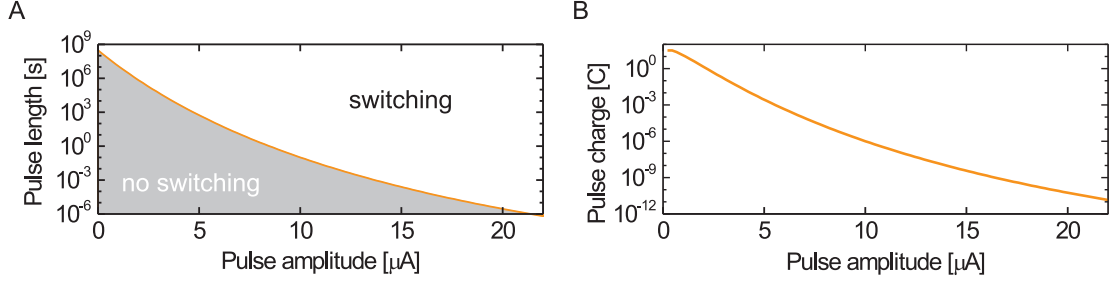
Figure 7.8: (**A**) Current pulse length as a function of the pulse amplitude to switch the magnetization of the given nanoisland that has been investigated in Fig. 7.6 after cooling it down to $T = 30\,\text{K}$. (**B**) Total charge that is flowing to switch the magnetization, as a function of the pulse amplitude. With increasing amplitude the total charge is decreased.

Knowing that the nanoisland has a mean lifetime $\bar{\tau} = 168\,\text{ms}$ at $T = 50.6\,\text{K}$ allows T_{stable} to be estimated:

$$\frac{\bar{\tau}_{\text{stable}}}{\bar{\tau}} = \exp\left[\frac{\Delta E_{\text{b}}}{k_{\text{B}} T_{\text{stable}}} - \frac{\Delta E_{\text{b}}}{k_{\text{B}} T}\right]$$

$$\Rightarrow \frac{1}{T_{\text{stable}}} = \frac{1}{T} + \frac{k_{\text{B}}}{E_{\text{b}}} \ln \frac{\bar{\tau}_{\text{stable}}}{\bar{\tau}}. \tag{7.12}$$

This leads to $T_{\text{stable}} \approx 30\,\text{K}$. To switch the nanoisland at this temperature with a high spin-polarized tunnel current, the mean lifetime has to be drastically reduced to a small value. The mean lifetime τ_{switch} in the high spin-polarized current regime can be calculated as a function of I, including the Joule heating contribution (ΔT_{JH}) and spin torque effects (ΔE_{ST}), both decreasing the effective activation barrier E_{b} to favor a magnetization reversal:

$$\tau_{\text{switch}}(I) = \tau_{\text{stable}} \cdot \exp\left[\frac{E_{\text{b}} - \Delta E_{\text{ST}}(I)}{k_{\text{B}}(T_{\text{stable}} + \Delta T_{\text{JH}}(I))} - \frac{E_{\text{b}}}{k_{\text{B}} T_{\text{stable}}}\right]. \tag{7.13}$$

Note that a high spin-polarized current has only to be applied until the first switching event occurs. Therefore, instead of a continuous current, short current pulses can be used that are long enough to cause a magnetization reversal. The minimum pulse length is given by $\tau_{\text{switch}}(I)$ and therefore depends on the current amplitude I.

In Fig. 7.8A, the minimum pulse length is plotted as a function of the pulse amplitude, derived from Eq. 7.13. Within the grey shaded area, the pulse will not cause the magnetization to switch, and the white area marks regions of possible pulse lengths and amplitudes for successful magnetization reversal. As can be seen from the plot, the pulse length decreases with increasing amplitude. For example, using a pulse amplitude of $5\,\mu\text{A}$ the minimum pulse length to switch the

magnetization of the given island is of the order of 400 s. This is of course too long for commercial data storage applications. A possible way to reduce the pulse length is to apply even higher tunnel currents or to use nanoislands with a lower effective activation energy barrier E_b.

From the pulse length τ_{switch} and the pulse amplitude I, the total charge $q = \tau_{switch} \cdot I$ that is needed to switch the magnetization can be determined, as shown in Fig. 7.8B. Note that $q = 1\,\text{nC}$ is related to approximately 6×10^9 electrons, thus, 10^6 to 10^{18} electrons are tunneling into the nanoisland to switch the magnetization. Since Joule heating effects play a crucial role, it is not possible to determine a single characteristic critical current I_c. In fact, I_c depends on the time required for magnetization reversal.

Assuming an effective area of the tunnel junction given by a lateral STM resolution of $5\,\text{Å}$ [37], the corresponding current density is $1.3 \times 10^8\,\text{A/cm}^2$ for $I = 1\,\mu\text{A}$. This value is one order of magnitude higher than the current density used in switching experiments based on TMR devices [98]. Note that in our experiments the tunnel current acts very locally at the injection point of the current, whereas in planar junctions the current density is averaged over the whole interfacial plane and is assumed to be homogenously distributed. But in fact, leakage channels at the interface may cause a locally increased current density. Consequently, it is reasonable that the current densities that drive the magnetization reversal are comparable both in the experiments using SP-STM and planar tunnel junctions.

7.5   Oersted field contributions

Spatially resolved measurements were performed using the SP-STM tip as a source or drain of spin-polarized electrons. Moving the tip to different sites on one particular nanoisland allows information on site-specific properties to be gained that cannot be obtained in spatially averaging experiments performed with nanopillars.

Figure 7.9A shows the topography of an iron nanoisland consisting of about 100 atoms. While scanning this island with $I = 600\,\text{nA}$, the magnetic $\text{d}I/\text{d}U$ signal on each of the pixels has been measured for a duration of 12 s to calculate the site-specific histogram asymmetry a_H on the basis of the corresponding data point histograms.

The result is shown in a color-coded representation in Fig. 7.9B. In spite of the rather large statistical error, a gradient along the [001] direction can clearly be seen. The effect can be analyzed quantitatively by averaging a_H column- and row-wise: that is, along the [1$\bar{1}$0] and the [001] directions, respectively. Whereas $\bar{a}_H$ is constant within the error at about 42% when moving the tip along the [1$\bar{1}$0] direction, it becomes smaller from the left (50%) to the right (34%) of the island.

The observation can be explained by the current that is flowing through the nanoisland and having an Oersted field: The current is surrounded by a magnetic
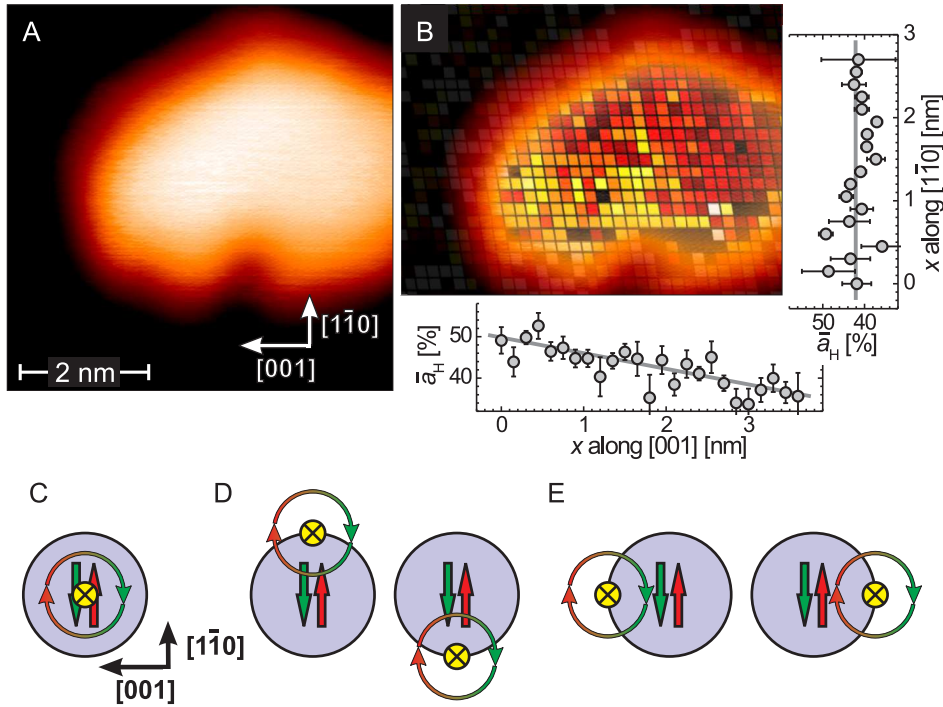
Figure 7.9: (**A**) Topography and (**B**) map of the current-induced asymmetry a_H as measured with a Cr-coated probe tip at $I = 600\,\mathrm{nA}$ and $U = +200\,\mathrm{mV}$ (island area: $(6.7 \pm 0.6)\,\mathrm{nm}^2$, $T = 55.0\,\mathrm{K}$). The plots show a_H averaged in rows and columns, i.e. along the $[1\bar{1}0]$ and $[001]$ direction, respectively. While $\bar{a}_H$ is constant within the error bar along the $[1\bar{1}0]$ direction, it clearly reduces by about $16\,\%$ from the left to the right side of the island (lines are guide to the eye only). The schematic illustrates the influence of the Oersted field with the tip positioned in the center (**C**), at the magnetic poles (**D**), or at the charge-free side (**E**) of the nanoisland.

field that interacts with the magnetization of the island. Consequently, the lateral tip position influences the switching behavior of the nanoisland at high tunneling currents. Three basic cases can be distinguished, as illustrated in Fig. 7.9, C to E.

If the tip is positioned above the island center, the influence of the Oersted field along the $[1\bar{1}0]$ direction, which is the easy axis of the nanoisland, cancels (Fig. 7.9C). In this case, pure spin-current induced switching occurs without any Oersted field contribution. Likewise, no influence by the Oersted field is expected if the tip is moved from the center to either island edge along the $[1\bar{1}0]$ direction (Fig. 7.9D) as the effective field acting on the island is oriented perpendicular to the easy axis. Only if the tip is moved from the center along the $[001]$ direction is one magnetic state favored over the other by the Oersted field (Fig. 7.9E). With the tip at the left edge of the island, one state is favored and the opposite state is favored with the tip at the right edge. Therefore, with the tip sampling data from left to right, i.e. perpendicular to the easy axis, we observe a slope in the histogram asymmetry as shown in Fig. 7.9B.
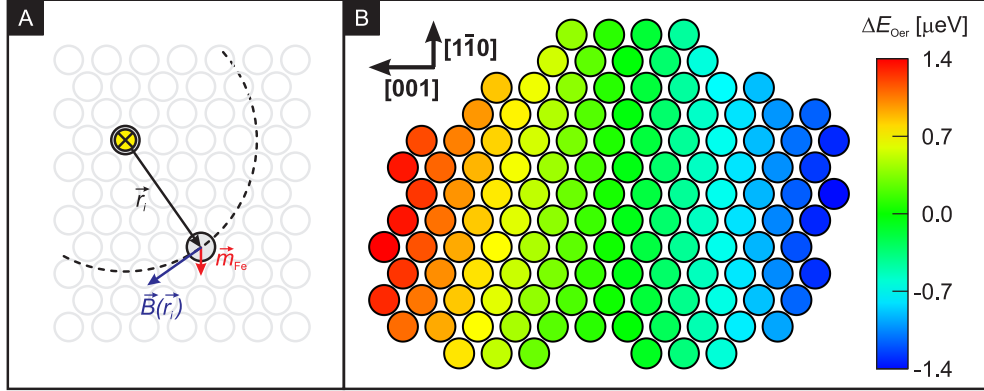
Figure 7.10: (**A**) Model of the Oersted field effect of a current flowing through a nanoisland. Every magnetic moment $\vec{m}_{\mathrm{Fe}}$ at position $\vec{r}_i$ relative to the tip position contributes the local Zeeman energy $\vec{m}_{\mathrm{Fe}} \cdot \vec{B}(\vec{r}_i)$ to the total Zeeman energy ΔE_{Oer}. (**B**) Color-coded results of the total Zeeman energy ΔE_{Oer} due to Oersted field effects as calculated for different tip positions.

The ratio between the Oersted field contribution ΔE_{Oer} and spin torque effect ΔE_{ST} can be determined directly from the spatially resolved histogram asymmetry at the center ($a_{\mathrm{H,c}} = 42\%$) and at the left edge ($a_{\mathrm{H,l}} = 50\%$) or right edge ($a_{\mathrm{H,r}} = 34\%$) of the nanoisland. Using Eq. 7.8 and the fact that $\bar{\tau}_1 / \bar{\tau}_0 = (1 + a_{\mathrm{H}})/(1 - a_{\mathrm{H}})$ results in

$$\frac{\Delta E_{\mathrm{L/R}}}{\Delta E_C} = \frac{\ln \frac{1 + a_{\mathrm{H,L/R}}}{1 - a_{\mathrm{H,L/R}}}}{\ln \frac{1 + a_{\mathrm{H,C}}}{1 - a_{\mathrm{H,C}}}}, \tag{7.14}$$

with $\Delta E_{\mathrm{L}} = \Delta E_{\mathrm{ST}} + \Delta E_{\mathrm{Oer}}$ and $\Delta E_{\mathrm{R}} = \Delta E_{\mathrm{ST}} - \Delta E_{\mathrm{Oer}}$ being the total change of the effective activation barrier energy at the left and right edge of the island due to the combined spin torque and Oersted field effect, and $\Delta E_{\mathrm{C}} = \Delta E_{\mathrm{ST}}$ being the pure spin torque effect (because Oersted field effects cancel at the center of the island). Using the experimentally determined histogram asymmetries a_{H} results in $\Delta E_{\mathrm{Oer}} = 0.22 \cdot \Delta E_{\mathrm{ST}}$. Assuming the spin torque effect is the same as determined from the lifetime analysis, the Oersted field effect can be estimated quantitatively for $I = 600\,\mathrm{nA}$: $\Delta E_{\mathrm{Oer}} \approx 0.2\,\mathrm{meV}$. This finding indicates that the magnetization switching is dominated by the spin torque induced by the spin-polarized current, whereas the influence of the Oersted field remains small.

Theoretical models to describe Oersted field effects

Two simple models help to quantitatively estimate the Oersted field contribution from a theoretical point of view. In classical physics, the Oersted field $\vec{B}(\vec{r})$ of a wire with a vanishing cross-sectional area and infinite length is given by

$$\vec{B}(\vec{r}) = \frac{\mu_0}{2\pi |\vec{r}|} \cdot I \cdot \hat{r}_\perp, \tag{7.15}$$

with $\vec{r}$ being the position vector lying in a plane perpendicular to the wire, and $\mu_0 = 4\pi \times 10^{-7}\,\mathrm{N/A^2}$ is the vacuum permeability. $\hat{r}_\perp$ denotes a unit vector lying perpendicular to $\vec{r}$ having a right-handed rotation with respect to the current direction. Every atom within the Fe nanoisland on W(110) has a magnetic moment $\vec{m}$. Due to uniaxial anisotropy, $\vec{m}$ aligns along the $[1\bar{1}0]$ direction. The Oersted field, which is an inhomogeneous magnetic field, interacts with all the magnetic moments of the island, leading to a total Oersted field energy $\Delta E_{\mathrm{Oer}}(\vec{r}_{\mathrm{tip}})$ as a function of tip position $\vec{r}_{\mathrm{tip}}$ (see Fig. 7.10A):

$$\Delta E_{\mathrm{Oer}}(\vec{r}_{\mathrm{tip}}) = \sum_i \vec{m}_{\mathrm{Fe}} \cdot \vec{B}(\vec{r}_i - \vec{r}_{\mathrm{tip}}) \cdot (1 - \delta_{\vec{r}_i, \vec{r}_{\mathrm{tip}}}), \qquad (7.16)$$

where $\vec{r}_i$ is the position of atom i. For the nanoisland, $|\vec{m}| = 2.79\mu_{\mathrm{B}}$ [99], with $\mu_{\mathrm{B}} = e\hbar/2m_{\mathrm{e}}$, e is the electron charge and m_{e} is the electron mass.

In Fig. 7.10B, the total Oersted field energy $\Delta E_{\mathrm{Oer}}(\vec{r}_{\mathrm{tip}})$ of the nanoisland is plotted in a color-coded representation as a function of the tip position on a fictitious atomic lattice of the island. A gradient along the [001] direction is clearly visible, reproducing the experimental results shown in Fig. 7.9B. Note that the Oersted field cancels in the center region due to the symmetry of the island. The maximum Oersted field energy at the left or right edge of the island is $|\Delta E_{\mathrm{Oer}}| \leq 1.4\,\mu\mathrm{eV}$, which is a very small value compared to the experimental result.

An analytical way to determine the Oersted field contribution is to calculate $\Delta E_{\mathrm{Oer}}(\vec{r}_{\mathrm{tip}})$ for a circularly shaped nanoisland from an integral over the island volume V. The maximum value of $|\Delta E_{\mathrm{Oer,max}}|$ is given when the tip is positioned on the left or right edge of the nanoisland, $\vec{r}_{\mathrm{tip}} = \vec{r}_{\mathrm{tip,max}}$. In this configuration,

$$\begin{aligned} |\Delta E_{\mathrm{Oer,max}}| &= -\int_V \frac{\vec{m}_{\mathrm{Fe}}}{V_{\mathrm{atom}}} \cdot \vec{B}(\vec{r} - \vec{r}_{\mathrm{tip,max}})\mathrm{d}^3 r \\ &= -\frac{m_{\mathrm{Fe}}}{\sqrt{2} \cdot a_{\mathrm{W}}^2} \cdot \mu_0 \cdot R \cdot I. \end{aligned} \qquad (7.17)$$

Here, V_{atom} is the atomic volume with the tungsten lattice constant $a_{\mathrm{W}} = 0.316\,\mathrm{nm}$, and R denotes the radius of the island. For this model, the nanoisland from the experiment is assumed to be circular shaped with the same volume, therefore $R = (1.5 \pm 0.2)\,\mathrm{nm}$. From this calculation, a maximum Oersted field energy of $|\Delta E_{\mathrm{Oer,max}}| = (1.3 \pm 0.2)\,\mu\mathrm{eV}$ is estimated. This value is also two orders of magnitude smaller than determined from the experiment, but fits very well the rough estimation of the first simple model described above.

The question arises what external homogeneous magnetic field would have the same influence on the switching behavior as the Oersted field that is generated when the tip is positioned at the [001] edge of the nanoisland. The field energy E_{ext} of an external field is given by

$$\Delta E_{\mathrm{ext}} = N \cdot \vec{m}_{\mathrm{Fe}} \cdot \vec{B}, \qquad (7.18)$$

with N being the number of atoms within a nanoisland. For the island investigated, $N = 95 \pm 8$. Consequently, the Oersted field energy is effectively equal to an external magnetic field $|\vec{B}| \approx 80\,\mu\text{T}$. This very small value is comparable to the earth's magnetic field, which in Germany is on the order of $10\,\mu\text{T}$ to $15\,\mu\text{T}$.

Obviously, the simple estimations from the theoretical point of view are not suitable to reproduce the experimental results regarding the Oersted field contributions. Maybe some assumptions are not appropriate: For example, the classical model of a wire with minimal cross-sectional area and an infinite length is certainly not adequate to describe the electron flow through a nanoisland, and hence the Oersted field is not derived correctly. In principle it is a basic and still open question if and how tunneling electrons generate an Oersted field during the tunneling process. Future investigations will help to get a deeper insight into this topic.

To summarize, a high spin-polarized current injected into a thermally switching nanoisland leads to the modification of the mean magnetic state lifetimes due to the combined effect of spin torque generation, Joule heating and Oersted field contributions. The experiments allow to quantify the three effects, thereby revealing that the Oersted field only has a minor effect compared to those of spin torque and Joule heating.

Chapter 8

Switching the Magnetization of Quasistable Nanoislands

The challenge for future data storage applications is to switch nanoscale magnetic bits that exhibit stable magnetization over a period of at least ten years. Hence, current-induced magnetization switching must be the single driving force for the magnetization reversal, and every single bit has to be thermally stable.

So far, we investigated current-induced magnetization switching in the temperature regime where the islands frequently switch their magnetization due to thermal excitation, and the effect of the spin current is to generate an imbalance of state lifetimes. Now we want to switch islands that exhibit a stable magnetization over the time scale of the experiment. For this purpose we use a different technique. In contrast to the previous experiments, the steady high current is replaced by a short high-current pulse to switch the magnetization of quasistable nanoislands. This technique prevents the tip from eventual damage or electronic changes, which have been observed frequently for continuous currents exceeding $2\,\mu\text{A}$.

8.1   Nanoisland in the low-frequency regime

The topography of a W(110) surface decorated with Fe monolayer nanoislands is shown in Fig. 8.1A. The simultaneously recorded magnetic $\mathrm{d}I/\mathrm{d}U$ map in Fig. 8.1B reveals that most of the nanoislands exhibit an unstable magnetization – they switch frequently at $T = 44.2\,\text{K}$. However, only one single switching event is observed for the center island (marked by the arrow).

After positioning the tip above the center region of the quasistable island, the $\mathrm{d}I/\mathrm{d}U$ signal and the tip displacement have been measured simultaneously as a function of time t with a closed feedback loop at low tunnel current, as shown in Fig. 8.1C. At $t = 0\,\text{s}$, the magnetization of the island is in the state "0", indicated by a low $\mathrm{d}I/\mathrm{d}U$ signal. After some time, the $\mathrm{d}I/\mathrm{d}U$ signal changes to state
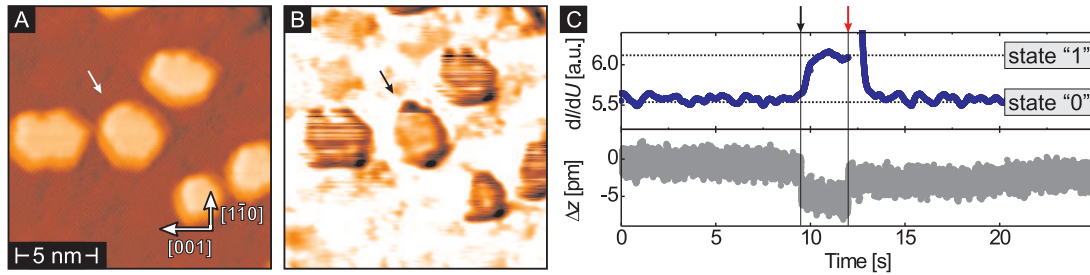
Figure 8.1: (**A**) Topography and (**B**) in-plane magnetic dI/dU map of Fe monolayer islands on W(110) measured at $T = 44.2$ K (parameters: $I = 2$ nA, $U = -200$ mV). Whereas the center island (marked by arrow; size: (5.6 ± 0.6) nm^2) only switches once, the neighbouring islands switch more often due to thermal agitation. The center island has been investigated in detail (parameters: $I = 20$ nA, $U = -200$ mV). (**C**) dI/dU signal (top) and tip displacement Δz as measured as a function of time. The island switches thermally from state "0" to state "1" (indicated by black arrow), and the tip-sample distance is decreased by ≈ 5 pm. After two seconds a short high-current pulse is applied (red arrow), causing magnetization reversal of the nanoisland from state "1" back to state "0".

"1" (marked by the black arrow), thereby indicating that the nanoisland reverses its magnetization due to thermal activation. In addition, the tip has slightly approached the surface ($\Delta z \approx -5$ pm). Consequently, the magnetization of tip and sample was in the parallel configuration at $t = 0$ s, and due to the switching event it changes to the antiparallel configuration. Because the tunnel resistance is now increased, the tip has to approached the sample to keep the tunnel current constant. Note that the slow change of the dI/dU signal contrasting with the abrupt change in the tip's z-position arises from the fact that a lock-in integrating time constant of 100 ms was used to get a sufficiently high signal-to-noise ratio at the low setpoint current I in the high-current range of the current-to-voltage amplifier.

About two seconds after the thermal switching event, a manually initiated high-current pulse ($I_p = 5$ µA, $U_p = -200$ mV, $t_p = 10$ ms, closed feedback loop) has been applied, as marked by the red arrow. The pulse generation has been realized with a special macro, and data acquisition is interrupted for the duration of the pulse, therefore the respective dI/dU signal and tip displacement Δz are not recorded during the pulse. After the pulse, the dI/dU signal as well as the tip displacement Δz changed back to the initial configuration. Obviously, the nanoisland has switched back to the initial magnetic state "0". The z position of the tip changed slightly compared to the situation before the pulse, which is caused by thermal drift of the piezo scanner that is compensated by the feedback-loop.

To prove the effectiveness of this switching technique, a series of current pulses has been applied to switch the magnetization of the chosen island. A 1000 s section of the dI/dU signal is shown in Fig. 8.2. The grey data points are related to the
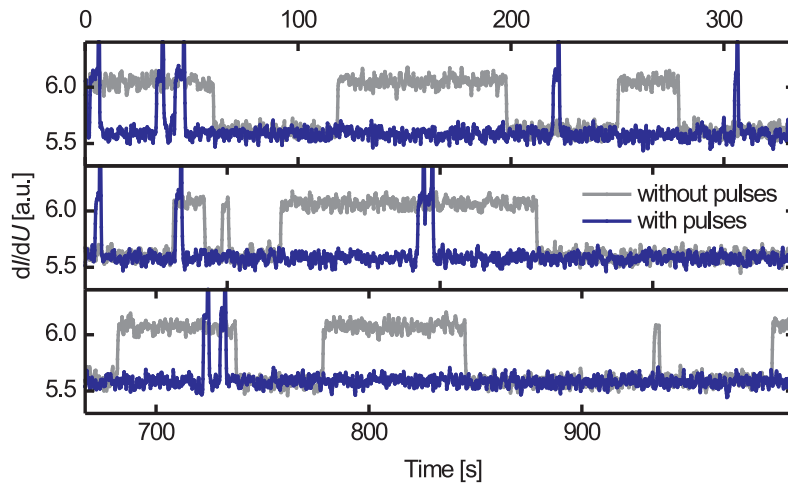
Figure 8.2: $1000\,\text{s}$ section of the $\mathrm{d}I/\mathrm{d}U$ signal as recorded at low tunnel current ($I = 20\,\text{nA}$). Whereas in the first experiment the intrinsic thermally activated magnetization switching is observed with no interaction between tip and sample (grey line), short current pulses were applied after every thermally induced switching event in the second experiment (blue line), forcing the island to switch back its magnetization.

signal recorded at low tunnel currents without applications of high-current pulses, revealing that the magnetization rarely switches. In total, 70 switching events from state "0" to state "1" were recorded within $5000\,\text{s}$. In a second experiment, every single thermal switching event to the state "1" is followed by a manually initiated high-current pulse, thereby trying to switch back the magnetization to the state "0" (blue data points). 67 out of 70 attempts (that is 96%) were successful and caused a reversal of the magnetization. Consequently, short tunnel current pulses can be used to reverse the magnetization of a nanoisland that switches at a very low frequency.

However, from this experiment it remains unclear if the spin torque or the Joule heating is the driving force for the magnetization reversal. To get a deeper insight to the processes involved in magnetization switching, a more complex experiment has to be performed, including a detailed analysis of the Joule heating and spin torque contributions in the high-current tunneling regime. This has been done in the following.

8.2 Quasistable nanoisland

Figure 8.3 illustrates the basic idea for switching an individual thermally stable magnetic nanoisland using short pulses of high spin-polarized currents. Initially, the island is considered to be in the state "down" (A). The high effective activation
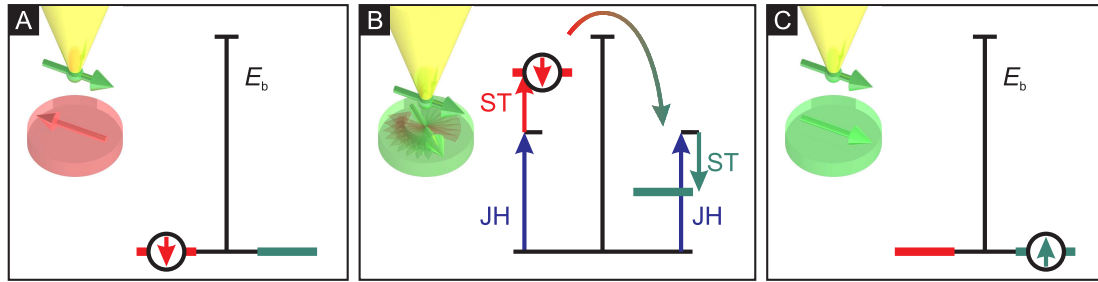
Figure 8.3: Basic principle of switching the magnetization of a nanoisland by applying a short current pulse. (**A**) Initial state. The magnetization is in the state "down", and the high effective activation barrier (E_b) prevents thermal switching events. (**B**) Application of a high current pulse originating from a magnetic STM tip. Joule heating (JH) decreases E_b for both states, and spin torque effects (ST) lift the degeneracy of the state lifetimes, thereby favoring a magnetization reversal from state "down" to "up". (**C**) End state. The magnetization is in state "up", and E_b prevents thermal switching events.

barrier E_b prevents magnetization by thermally driven reversal. After approaching a magnetic STM tip, a high spin-polarized current pulse is applied between the tip and the nanoisland (B). During the pulse, two distinct effects influence the magnetic state of the island. First, the Joule heating (JH) increases the effective temperature of the nanoisland, thereby decreasing the lifetime of the magnetic state. Second, the spin torque effect (ST) lifts the degeneracy of the state lifetimes, and E_b is decreased for state "down", favoring a magnetic reversal. Once the magnetization has switched, the increased effective activation barrier for state "up" caused by the spin torque inhibits an additional magnetization reversal. Finally, the current pulse ends, and the high effective energy barrier E_b again stabilizes the magnetization of the nanoisland against thermally driven reversal (C).

In Fig. 8.4A, the topography of a nanoisland sample at $T = 31.5\,\text{K}$ is shown. The $\mathrm{d}I/\mathrm{d}U$ signal in Fig. 8.4B indicates that most of the nanoislands exhibit a stable magnetization. Because the magnetization obviously reverses on time scales larger than the time to record one image, a series of STM images ($500\,\text{s}$ each) has been recorded over six hours to find suitable nanoislands that exhibit a stable magnetization over that time period. A zoom to one of these thermally stable islands is shown in the insets of Fig. 8.4A and B. It is in state "0", as indicated by a low $\mathrm{d}I/\mathrm{d}U$ signal.

Characterization at elevated temperature

To determine the effective activation barrier E_b as well as the Joule heating and spin torque contributions at high spin-polarized currents, the system has been warmed up by several K, thereby crossing the blocking temperature for thermally activated switching of the magnetization.
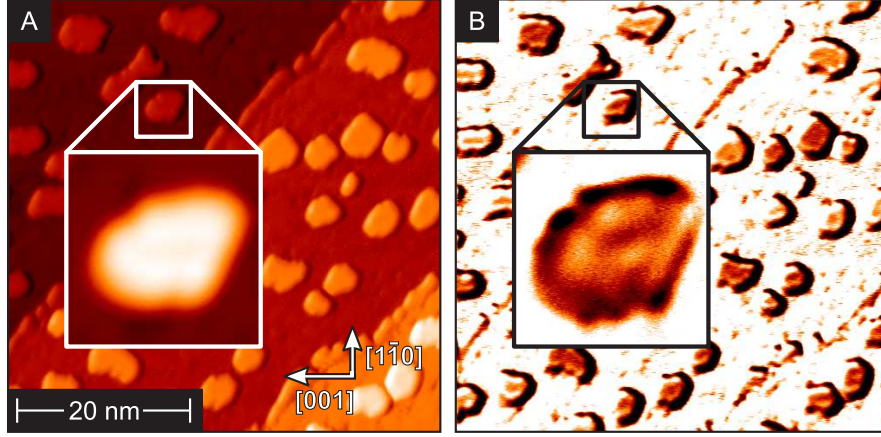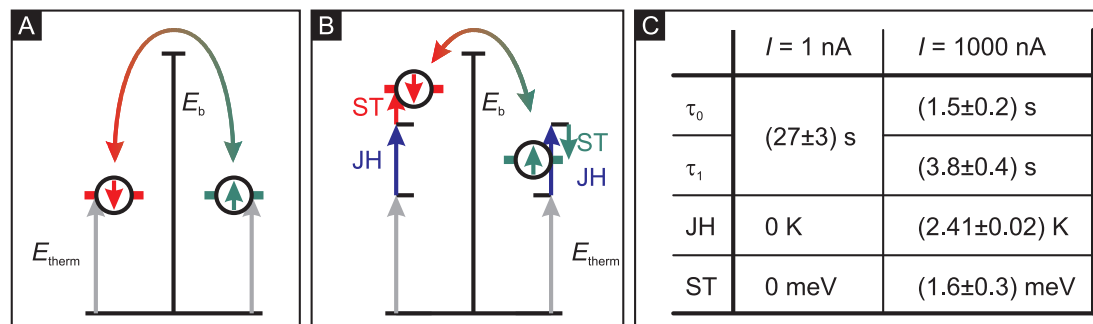
Figure 8.4: (**A**) Topography and (**B**) in-plane magnetic dI/dU map of Fe monolayer islands on W(110) measured at $T = 31.5\,$K (parameters: $I = 2\,$nA, $U = -200\,$mV; island size: $(4.0 \pm 0.4)\,$nm^2). Within the time for recording one image, most of the islands are magnetically stable. The particular island shown in the inset has been investigated in detail.

Now the magnetization is no longer stable, but switches thermally, as shown in Fig. 8.5A. At low tunnel current, intrinsic switching behavior has been observed at two different temperatures, $T = 36.9\,$K and $T = 38.8\,$K, leading to $\bar{\tau} = (27 \pm 3)\,$s and $\bar{\tau} = (3.6 \pm 0.2)\,$s, respectively. From the Arrhenius-like behavior of $\bar{\tau}$ as a function of T^{-1}, the effective activation barrier E_{b} can be deduced, leading to $E_{\mathrm{b}} = (126 \pm 8)\,$meV.

At $T = 36.9\,$K, the effects of a high tunnel current have been investigated in detail. As has been described in the experiments on the thermally switching nanoislands, two effects contribute to current-induced magnetization switching: Joule heating and spin torque. Their influence on the switching behavior is illustrated in Fig. 8.5B. At $I = 1000\,$nA, the mean lifetimes of state "0" ($\bar{\tau}_0$) and state "1" ($\bar{\tau}_1$) have been determined, yielding $\bar{\tau}_0 = (1.5 \pm 0.2)\,$s and $\bar{\tau}_1 = (3.8 \pm 0.4)\,$s. Following Eq. 7.5 and Eq. 7.8, the effective temperature rise ΔT_{JH} due to Joule heating and the modification ΔE_{ST} of the effective activation energy barrier due to the pure spin torque at $I = 1000\,$nA can be derived: $\Delta T_{\mathrm{JH}} = (2.41 \pm 0.02)\,$K and $\Delta E_{\mathrm{ST}} = \pm(1.6 \pm 0.3)\,$meV. The results are summarized in the table in Fig. 8.5C.

From $\Delta T_{\mathrm{JH}}(I = 1000\,\mathrm{nA})$ and $\Delta E_{\mathrm{ST}}(I = 1000\,\mathrm{nA})$ the effects of Joule heating and spin torque at even higher tunnel currents can be deduced: As has been shown in Fig. 7.7, both the Joule heating and the spin torque scale linearly with the tunnel current I. To switch the magnetization of the same nanoisland in the quasistable regime, a current pulse amplitude of $5000\,$nA was chosen. Consequently, in this high tunneling current regime, $\Delta T_{\mathrm{JH}}(I = 5000\,\mathrm{nA}) = (12.1 \pm 0.1)\,$K and $\Delta E_{\mathrm{ST}}(I = 5000\,\mathrm{nA}) = (8.0 \pm 1.5)\,$meV.

		$I = 1$ nA	$I = 1000$ nA
τ_0		(27±3) s	(1.5±0.2) s
τ_1			(3.8±0.4) s
JH		0 K	(2.41±0.02) K
ST		0 meV	(1.6±0.3) meV

Figure 8.5: (**A**) Principle of thermally induced magnetization switching. Due to thermal activation the magnetization may overcome the effective activation barrier E_b and therefore switch from "down" to "up" and vice versa. (**B**) Principle of current-induced magnetization switching in the superparamagnetic regime. Joule heating decreases E_b for both states, and spin torque effects lift the degeneracy of E_b, thereby favoring switching from state "down" to state "up". (**C**) State lifetimes τ_0 and τ_1, Joule heating contribution (JH) and spin torque contribution (ST) at low (1 nA) and high (1000 nA) tunnel current. Temperature: 36.9 K.

Switching the magnetization of a stable nanoisland

Now knowing the effective activation energy barrier E_b, the Joule heating $\Delta T_{JH}(I = 5000\,\text{nA})$ and the spin torque contributions $\Delta E_{ST}(I = 5000\,\text{nA})$, it is possible to find an appropriate current pulse length for switching the magnetization of the stable nanoisland very effectively. Initially, the nanoisland is in the state "0" at temperature $T = 31.5$ K. During the current pulse, the temperature of the nanoisland is increased by ≈ 12 K due to Joule heating, leading to a mean lifetime of state "0" and "1" $\bar{\tau}_{JH} \approx 65$ ms. Thus, a non-magnetic tip (with no spin torque effects) would maintain the degeneracy of the lifetime, and therefore switching back and forth would be equally probable.

Considering not only Joule heating but also the spin torque contribution of the high spin-polarized current pulse, the degeneracy of the lifetimes is lifted: For switching the magnetization from antiparallel to parallel configuration with respect to the tip magnetization, the lifetime is further decreased to $\bar{\tau}_{ST,P} \approx 8$ ms, whereas for switching the magnetization from parallel to antiparallel configurations, the lifetime is increased to $\bar{\tau}_{ST,AP} \approx 526$ ms. Obviously, the spin torque forces the magnetization to align in the parallel configuration, and once the reversal is achieved, the magnetization is stabilized by the spin torque.

The probability p_{switch} to switch the magnetization within a pulse length t_{pulse} is given by

$$p_{switch} = 1 - \exp\left[1 - \frac{t_{pulse}}{\bar{\tau}}\right], \tag{8.1}$$

with $\bar{\tau}$ being the mean lifetime during the high current pulse. $p_{switch}(t_{pulse})$ is shown in Fig. 8.6A for the three different parameters τ as determined for pure
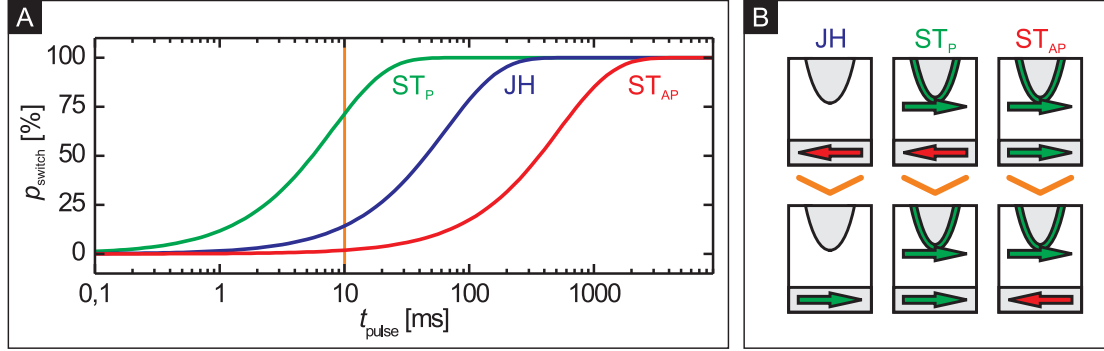
Figure 8.6: (**A**) Switching probabiblity p_{switch} as function of current pulse duration t_{pulse}, given by pure Joule heating (JH), spin torque switching to parallel (ST_P) and antiparallel (ST_{AP}) configuration of tip and sample magnetization. (**B**) Sketch of the different switching processes described in (A).

Joule heating (JH) and including spin torque effects: switching from antiparallel to parallel configuration of tip and sample magnetization (ST_P) or vice versa (ST_{AP}).

In the experiment, a tunnel current pulse of 5000 nA with a length of 10 ms has been applied. Considering only Joule heating (equivalent to a non-magnetic tip), the respective switching probability is $p_{switch} = 14\%$, and therefore it is unlikely to switch the magnetization by pure thermal activation. Taking the spin torque effects into account, the switching probability for a 10 ms pulse increases to $p_{switch} = 71\%$. Consequently, it is very likely to switch the magnetization by thermal and spin torque activation. The probability to switch the magnetization from antiparallel to parallel configuration is negligible, $p_{switch} = 2\%$. Thus, multiple switching events during the application of the current pulse can be neglected.

In Fig. 8.7A, the initial magnetic configuration is shown. The nanoisland under investigation appears dark, indicating that it is in the magnetic state "0". For the switching experiment the magnetic STM tip has been positioned above the center of the nanoisland at a tunnel current of 20 nA. Then a manually initiated high current pulse of 5000 nA with a duration of 10 ms has been applied. The respective setpoint current, dI/dU signal and z-displacement of the tip is shown in Fig. 8.7B. Right after the current pulse (at $t = 8$ s), the dI/dU signal has changed from state "0" to state "1", and also the z-displacement has abruptly changed by ≈ 0.2 Å. Note that the dI/dU signal only slowly leaves saturation after the current pulse because of a very long integrating time constant (100 ms) of the lock-in amplifier.

In order to exclude any tip changes as a reason for the changed dI/dU signal, a magnetic map of the nanoisland has been obtained after the pulse, as shown in Fig. 8.7C. It is clearly visible that the nanoisland changed its magnetization state
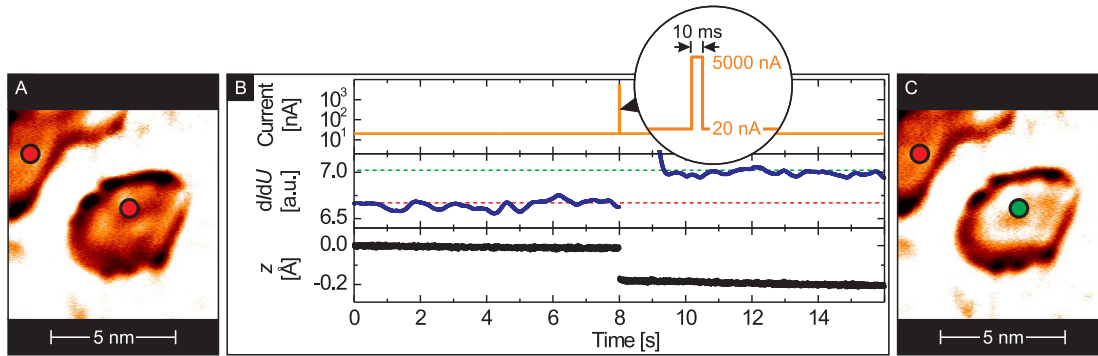
Figure 8.7: Switching the magnetization of a stable nanoisland by a current pulse. (**A**) Initial state. The nanoisland is in the magnetic state "0". (**B**) Current pulse experiment: tunnel current setpoint (top), dI/dU signal (middle) and z-displacement (bottom) as a function of time. After the current pulse, the magnetization of the island has changed, as indicated by the dI/dU signal and the z-displacement. (**C**) dI/dU map after the pulse. The nanoisland now is in the magnetic state "1".

from "0" to "1", as also indicated by the neighboring island which is still in the state "0" and has not been affected by the pulse.

Finally, a series of STM images has been taken to observe the switching behavior of the particular island and its surrounding. Even twelve hours after the high-current pulse, the STM images show no thermally activated magnetization reversal of the nanoisland that has been switched on purpose. Consequently, the magnetization reversal on the nanoisland indeed was iniated by the spin-torque from the high-current pulse and not by a coincidental thermal switching event. This finding indicates that a spin-polarized high-current pulse can be used to manipulate nanoislands that exhibit a thermally stable magnetization. Hence, the heat-assisted spin-torque of a high-current pulse generated by a SP-STM tip is high enough to overcome the activation energy barrier of an individual nanoisland.

Chapter 9

Summary and Perspectives

Switching the magnetization of a magnetic bit by the injection of a spin-polarized current offers the possibility for the development of innovative high-density data storage technologies. Within this work it is shown that individual magnetic iron nanoislands with typical sizes of 100 atoms can be addressed and locally switched using a magnetic scanning probe tip, thereby demonstrating current-induced magnetization switching across a vacuum barrier.

At elevated temperatures, the magnetization of each nanoisland normally fluctuates between two equally preferable magnetic states. A detailed analysis of this switching behavior as a function of temperature and island size reveals that the magnetization reversal of atomic-scale nanoislands is realized via the nucleation and diffusive propagation of domain walls. A coherent rotation of all magnetic moments during the magnetization reversal can be excluded.

The equilibrium of the magnetic state lifetime is broken when injecting a spin-polarized current. Depending on the current direction, the magnetization of the nanoisland favors parallel or antiparallel alignment with respect to the spin polarization of the current. The high lateral resolution of spin-polarized scanning tunneling microscopy allows three fundamental contributions involved in magnetization switching, i.e., current-induced spin torque, heating the island by the tunneling current, and Oersted field effects, to be quantified, thereby providing an improved understanding of the switching mechanism.

Moreover, a high spin-polarized current pulse also allows quasistable magnetic nanoislands to be switched, i.e. islands that switch their magnetization only once in several hours, thereby demonstrating that the torque generated by a spin-polarized tunnel current induces magnetic reversal in nanoislands that do not switch thermally.

While the fundamental physics underlying the spin transfer torque in spin valves has been extensively studied theoretically [3–17], its role in magnetic tunnel junctions remains an unexplored area so far, except for the pioneering work of Slonczewski [32, 33]. In magnetic tunnel junctions the spin-filtering and spin-
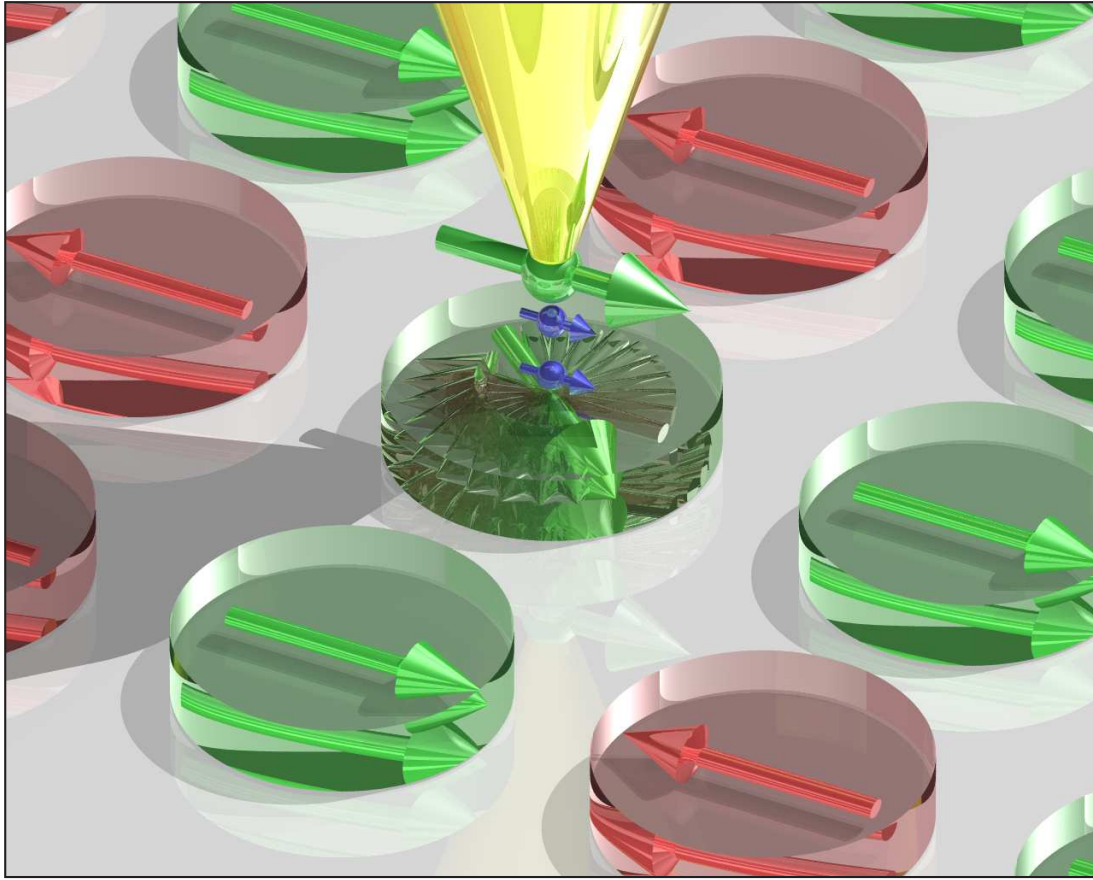
Figure 9.1: Application of SP-STM for the magnetic manipulation of nanoislands. The islands are addressed by a magnetic tip that serves as a combined read and write probe. At low spin-polarized tunnel current, the magnetic state of each nanoisland is read out. Using a high tunnel current, the magnetization of the nanoisland is reversed due to spin-torque effects.

torque generating processes depend strongly on the electronic structure of the electrodes, so it is very important to take a closer look at the theoretical background of current-induced magnetization switching through a vacuum barrier, including band structure effects.

The SP-STM experiments show that a magnetic scanning tip can be used both to read out information at lateral resolution down to the atomic scale and to manipulate very locally the magnetism of nanostructures, as illustrated in Fig.9.1. This technique opens up a completely new field of investigations using SP-STM as a tool for simultaneous manipulation and observation of magnetism at atomic lateral resolution, thereby providing new insights into magnetic phenomena on the nanoscale.

Current-induced magnetization switching combined with the ultimate lateral resolution of SP-STM will definitely provide new insight into the microscopic pro-

cesses of magnetization reversal. Many experiments on current-induced magnetization switching that have been performed on lithographically fabricated devices could now be repeated on the atomic-scale: While self-organized nanostructures or even single atoms provide a very well-defined sample, the injection point of a high spin-polarized current can be controlled precisely using SP-STM. Consequently, fascinating perspectives for a new class of experiments open up that will provide a more detailed understanding of magnetism and magnetic interactions.

Bibliography

[1] J. C. Slonczewski, J. Magn. Magn. Mater. **159**, L1 (1996).

[2] L. Berger, Phys. Rev. B **54**, 9353 (1996).

[3] J. A. Katine, F. J. Albert, R. A. Buhrman, E. B. Myers, and D. C. Ralph, Phys. Rev. Lett. **84**, 3149 (2000).

[4] M. Tsoi, A. G. M. Jansen, J. Bass, W.-C. Chiang, M. Seck, V. Tsoi, and P. Wyder, Phys. Rev. Lett. **80**, 4281 (1998).

[5] E. B. Myers, D. C. Ralph, J. A. Katine, R. N. Louie, and R. A. Buhrman, Science **285**, 867 (1999).

[6] J. E. Wegrowe, D. Kelly, Y. Jaccard, P. Guittienne, and J. P. Ansermet, Europhys. Lett. **45**, 626 (1999).

[7] J. E. Wegrowe, D. Kelly, X. Hoffer, P. Guittienne, and J. P. Ansermet, J. Appl. Phys. **89**, 7127 (2001).

[8] D. Kelly, J. E. Wegrowe, T. K. Truong, X. Hoffer, and J. P. Ansermet, Phys. Rev. B **68**, 134425 (2003).

[9] J. Z. Sun, J. Magn. Magn. Mater. **202**, 157 (1999).

[10] F. B. Mancoff and S. E. Russek, IEEE Trans. Magn. **38**, 2853 (2002).

[11] F. J. Albert, N. C. Emley, E. B. Myers, D. C. Ralph, and R. A. Buhrman, Phys. Rev. Lett. **89**, 226802 (2002).

[12] W. H. Rippard, M. R. Pufall, and T. J. Silva, Appl. Phys. Lett. **82**, 1260 (2003).

[13] M. R. Pufall, W. H. Rippard, and T. J. Silva, Appl. Phys. Lett. **83**, 323 (2003).

[14] B. Özyilmaz, A. D. Kent, D. Monsma, J. Z. Sun, M. J. Rooks, and R. H. Koch, Phys. Rev. Lett. **91**, 067203 (2003).

[15] Y. Ji, C. L. Chien, and M. D. Stiles, Phys. Rev. Lett. **90**, 106601 (2003).

[16] J. Hayakawa, K. Ito, M. Fujimori, S. Heike, T. Hashizume, J. Steen, J. Brugger, and H. Ohno, J. Appl. Phys. **96**, 3440 (2004).

[17] Y. Jiang, S. Abe, T. Ochiai, T. Nozaki, A. Hirohata, N. Tezuka, and K. Inomata, Phys. Rev. Lett. **92**, 167204 (2004).

[18] Y. Acremann, J. P. Strachan, V. Chembrolu, S. D. Andrews, T. Tyliszczak, J. A. Katine, M. J. Carey, B. M. Clemens, H. C. Siegmann, and J. Stöhr, Phys. Rev. Lett. **96**, 217202 (2006).

[19] R. Wiesendanger, *Scanning Probe Microscopy and Spectroscopy: Methods and Applications* (Cambridge Univ. Press, Cambridge, 1994).

[20] M. Bode, Rep. Progr. Phys. **66**, 523 (2003).

[21] D. Weller and A. Moser, IEEE Trans. Magn. **35**, 4423 (1999).

[22] M. L. Néel, Ann. Géophys. **5**, 99 (1949).

[23] W. F. Brown, Phys. Rev. **130**, 1677 (1963).

[24] W. Wernsdorfer, B. Doudin, D. Mailly, K. Hasselbach, A. Benoit, J. Meier, J.-P. Ansermet, and B. Barbara, Phys. Rev. Lett. **77**, 1873 (1996).

[25] W. Wernsdorfer, K. Hasselbach, A. Benoit, B. Barbara, B. Doudin, J. Meier, J.-P. Ansermet, and D. Mailly, Phys. Rev. B **55**, 11552 (1997).

[26] W. Wernsdorfer, E. B. Orozco, K. Hesselbach, A. Benoit, B. Barbara, N. Demoney, A. Loiseau, H. Pascard, and D. Mailly, Phys. Rev. Lett. **78**, 1791 (1997).

[27] M. Bode, O. Pietzsch, A. Kubetzka, and R. Wiesendanger, Phys. Rev. Lett. **92**, 067201 (2004).

[28] M. N. Baibich, J. M. Broto, A. Fert, F. N. V. Dau, F. Petroff, P. Eitenne, G. Creuzet, A. Friederich, and J. Chazelas, Phys. Rev. Lett. **61**, 2472 (1988).

[29] G. Binasch, P. Grünberg, F. Saurenbach, and W. Zinn, Phys. Rev. B **39**, 4828 (1989).

[30] M. Julliere, Phys. Lett. A **54**, 225 (1975).

[31] M. D. Stiles and A. Zangwill, Phys. Rev. B **66**, 014407 (2002).

[32] J. C. Slonczewski, Phys. Rev. B **39**, 6995 (1989).

[33] J. C. Slonczewski, Phys. Rev. B **71**, 024411 (2005).

[34] J. Z. Sun, Phys. Rev. B **62**, 570 (2000).

[35] G. Binnig, H. Rohrer, C. Gerber, and E. Weibel, Phys. Rev. Lett. **50**, 120 (1983).

[36] J. Bardeen, Phys. Rev. Lett. **6**, 57 (1961).

[37] J. Tersoff and D. R. Hamann, Phys. Rev. Lett. **50**, 1998 (1983).

[38] J. Tersoff and D. R. Hamann, Phys. Rev. B **31**, 805 (1985).

[39] R. J. Hamers, Annu. Rev. Phys. Chem. **40**, 531 (1989).

[40] J. Li, W.-D. Schneider, and R. Berndt, Phys. Rev. B **56**, 7656 (1997).

[41] D. Wortmann, S. Heinze, P. Kurz, G. Bihlmayer, and S. Blügel, Phys. Rev. Lett. **86**, 4132 (2001).

[42] R. Wiesendanger, H. J. Güntherodt, G. Güntherodt, R. J. Gambino, and R. Ruf, Phys. Rev. Lett. **65**, 247 (1990).

[43] S. Blügel, D. Pescia, and P. H. Dederichs, Phys. Rev. B **39**, 1392 (1989).

[44] M. Kleiber, M. Bode, R. Ravlić, N. Tezuka, and R. Wiesendanger, J. Magn. Magn. Mater. **240**, 64 (2002).

[45] A. Kubetzka, O. Pietzsch, M. Bode, and R. Wiesendanger, Appl. Phys. A **76**, 873 (2003).

[46] H. Lüth, *Surfaces and interfaces of solid materials* (Springer-Verlag, Berlin, 2001).

[47] Omicron Nanotechnology GmbH, D-65232 Taunusstein (1995).

[48] T. Hänke, Ph.D. thesis, University of Hamburg (2005).

[49] O. Pietzsch, A. Kubetzka, D. Haude, M. Bode, and R. Wiesendanger, Rev. Sci. Instr. **71**, 424 (2000).

[50] S. H. Pan, *Piezo-electric motor*, International Patent Publication Number WO 93/19494, International Bureau, World Intellectual Organization (1993).

[51] CryoVac GmbH, D-53842 Troisdorf (1998).

[52] FEMTO Messtechnik GmbH, Berlin, Germany.

[53] L. Limot, J. Kröger, R. Berndt, A. Garcia-Lekue, and W. A. Hofer, Phys. Rev. Lett. **94**, 126102 (2005).

[54] A. Kubetzka, M. Bode, O. Pietzsch, and R. Wiesendanger, Phys. Rev. Lett. **88**, 057201 (2002).

[55] M. Bode, S. Krause, L. Berbil-Bautista, S. Heinze, and R. Wiesendanger, Surf. Sci. **601**, 3308 (2007).

[56] http://www.webelements.de.

[57] U. Gradmann, G. Liu, H. J. Elmers, and M. Przybylski, Hyp. Int. **57**, 1845 (1990).

[58] E. Bauer, Z. Kristallogr. **110**, 372 (1958).

[59] H. Bethge, D. Heuer, C. Jensen, K. Reshöft, and U. Köhler, Surf. Sci. **331**–**333**, 878 (1995).

[60] M. Bode, Ph.D. thesis, University of Hamburg (1996).

[61] A. Wachowiak, J. Wiebe, M. Bode, O. Pietzsch, M. Morgenstern, and R. Wiesendanger, Science **298**, 577 (2002).

[62] N. Weber, K. Wagner, H. J. Elmers, J. Hauschild, and U. Gradmann, Phys. Rev. B **55**, 14121 (1997).

[63] J. Hauschild, U. Gradmann, and H. J. Elmers, Appl. Phys. Lett. **72**, 3211 (1998).

[64] O. Pietzsch, A. Kubetzka, M. Bode, and R. Wiesendanger, Phys. Rev. Lett. **84**, 5212 (2000).

[65] O. Pietzsch, A. Kubetzka, M. Bode, and R. Wiesendanger, Science **292**, 2053 (2001).

[66] M. Bode, A. Kubetzka, O. Pietzsch, and R. Wiesendanger, Appl. Phys. A **72**, S149 (2001).

[67] M. Bode, S. Heinze, A. Kubetzka, O. Pietzsch, X. Nie, G. Bihlmayer, S. Blügel, and R. Wiesendanger, Phys. Rev. Lett. **89**, 237205 (2002).

[68] M. Bode, A. Kubetzka, S. Heinze, O. Pietzsch, R. Wiesendanger, M. Heide, X. Nie, G. Bihlmayer, and S. Blügel, J. Phys.: Condens. Matter **15**, S679 (2003).

[69] A. Kubetzka, O. Pietzsch, M. Bode, and R. Wiesendanger, Phys. Rev. B **67**, 020401 (2003).

[70] H. J. Elmers, J. Hauschild, H. Höche, U. Gradmann, H. Bethge, D. Heuer, and U. Köhler, Phys. Rev. Lett. **73**, 898 (1994).

[71] M. Pratzer, H. J. Elmers, M. Bode, O. Pietzsch, A. Kubetzka, and R. Wiesendanger, Phys. Rev. Lett. **87**, 127201 (2001).

[72] M. Heide, G. Bihlmayer, and S. Blügel, Phys. Rev. B **78**, 140403(R) (2008).

[73] R. Kurzawa, K.-P. Kämper, W. Schmitt, and G. Güntherodt, Sol. State Commun. **60**, 777 (1986).

[74] H.-B. Braun, Phys. Rev. Lett. **71**, 3557 (1993).

[75] H.-B. Braun, Phys. Rev. B **50**, 16501 (1994).

[76] H.-B. Braun, J. Appl. Phys. **85**, 16172 (1999).

[77] A. Hubert and R. Schäfer, *Magnetic Domains* (Springer, 1998).

[78] I. N. Krivorotov, N. C. Emley, J. C. Sankey, S. I. Kiselev, D. C. Ralph, and R. A. Buhrman, Science **307**, 228 (2005).

[79] N. C. Emley, I. N. Krivorotov, O. Ozatay, A. F. Garcia, J. C. Sankey, D. C. Ralph, and R. A. Buhrman, Phys. Rev. Lett. **96**, 247204 (2006).

[80] G. Ehrlich, J. Chem. Phys. **44**, 1050 (1965).

[81] D. Hinzke and U. Nowak, Phys. Rev. B **61**, 6734 (2000).

[82] T. K. McNab, R. A. Fox, and A. J. Boyle, J. Appl. Phys. **39**, 5703 (1968).

[83] N. D. Rizzo, T. J. Silva, and A. B. Kos, Phys. Rev. Lett. **83**, 4876 (1999).

[84] S. I. Woods, J. R. Kirtley, S. Sun, and R. H. Koch, Phys. Rev. Lett. **87**, 137205 (2001).

[85] X. Wang and H. N. Bertram, J. Appl. Phys. **92**, 4560 (2002).

[86] S. Chikazumi, *Physics of Ferromagnetism* (Clarendon Press, Oxford, 1997).

[87] S. Rusponi, T. Cren, N. Weiss, M. Epple, P. Buluschek, L. Claude, and H. Brune, Nat. Mat. **2**, 546 (2003).

[88] M. Pratzer and H. J. Elmers, Phys. Rev. B **67**, 094416 (2003).

[89] R. H. Fowler and L. Nordheim, Proc. Roy. Soc. A **119**, 173 (1928).

[90] N. D. Lang, Phys. Rev. B **36**, 8173 (1987).

[91] G. Binnig, H. Rohrer, C. Gerber, and E. Weibel, Appl. Phys. Lett. **40**, 178 (1982).

[92] L. Olesen, M. Brandbyge, M. R. Sørensen, K. W. Jacobsen, E. Lægsgaard, I. Stensgaard, and F. Besenbacher, Phys. Rev. Lett. **76**, 1485 (1996).

[93] M. Bode, R. Pascal, and R. Wiesendanger, J. Vac. Sci. & Tech. A **15**, 1285 (1997).

[94] J. C. Slonczewski, J. Magn. Magn. Mater. **195**, L261 (1999).

[95] H. Goldenberg, Brit. J. Appl. Phys. **3**, 296 (1952).

[96] M. P. Seah and W. A. Dench, Surf. Interface Anal. **1**, 2 (1979).

[97] I. Bat'ko and M. Bat'ková, Eur. Phys. J. Appl. Phys. **31**, 191 (2005).

[98] G. D. Fuchs, N. C. Emley, I. N. Krivorotov, P. M. Braganca, E. M. Ryan, S. I. Kiselev, D. C. R. J. C. Sankey, R. A. Buhrman, and J. A. Katine, Appl. Phys. Lett. **85**, 1205 (2004).

[99] J. Hauschild, H. J. Elmers, and U. Gradmann, Phys. Rev. B **57**, R677 (1998).

Publications

- T. Hänke, S. Krause, L. Berbil-Bautista, M. Bode, R. Wiesendanger, V. Wagner, D. Lott, and A. Schreyer, *Absence of Spin-flip Transition at the Cr(001) Surface: A Combined Spin-polarized Scanning Tunneling Microscopy and Neutron Scattering Study*, Phys. Rev. B **71**, 184407 (2005).

- T. Hänke, M. Bode, S. Krause, L. Berbil-Bautista, and R. Wiesendanger, *Temperature-dependent Scanning Tunneling Spectroscopy of Cr(001): Orbital Kondo Resonance versus Surface State*, Phys. Rev. B **72**, 085453 (2005).

- L. Berbil-Bautista, S. Krause, T. Hänke, M. Bode, and R. Wiesendanger, *Spin-polarized Scanning Tunneling Microscopy Through an Adsorbate Layer: Sulfur-covered Fe/W(110)*, Surf. Sci. Lett. **600**, L20 (2006).

- S. Krause, L. Berbil-Bautista, T. Hänke, F. Vonau, M. Bode, and R. Wiesendanger, *Consequences of Line Defects on the Magnetic Structure of High Anisotropy Films: Pinning Centers on Dy/W(110)*, Europhys. Lett. **76**, 637 (2006).

- M. Bode, S. Krause, L. Berbil-Bautista, S. Heinze and R. Wiesendanger, *On the Preparation and Electronic Properties of Clean W(110) Surfaces*, Surf. Sci. **601**, 3308 (2007).

- L. Berbil-Bautista, S. Krause, M. Bode, and R. Wiesendanger, *Spin-polarized Scanning Tunneling Microscopy and Spectroscopy of Ferromagnetic Dy(0001)/W(110) Films*, Phys. Rev. B **76**, 064411 (2007).

- S. Krause, L. Berbil-Bautista, G. Herzog, M. Bode, and R. Wiesendanger, *Current-Induced Magnetization Switching with a Spin-Polarized Scanning Tunneling Microscope*, Science **317**, 1537 (2007).

Conferences

Invited talks

- 2008-03-11:
  Current-induced Magnetization Switching With a Spin-polarized Scanning Tunneling Microscope, March Meeting 2008 of the American Physical Society, New Orleans, Louisiana (USA).

- 2008-07-16:
  Current-induced Magnetization Switching With a Spin-polarized Scanning Tunneling Microscope, NSS5 / SP-STM2, Athens, Ohio (USA).

- 2008-07-31:
  Current-induced Magnetization Switching With a Spin-polarized Scanning Tunneling Microscope, ECOSS-25, Liverpool (UK).

Contributed talks

- 2004-03-10:
  S. Krause, T. Hänke, M. Bode, and R. Wiesendanger, *Spinpolarisierte Rastertunnelmikroskopie der Cr(001)-Oberfläche bei variabler Temperatur*, 68th Spring Conference, Deutsche Physikalische Gesellschaft, Regensburg (Germany).

- 2005-03-09:
  S. Krause, L. Berbil-Bautista, T. Hänke, M. Bode, and R. Wiesendanger, *Spinpolarisierte Rastertunnelmikroskopie auf S-bedeckten Fe-Inseln*, 69th Spring Conference, Deutsche Physikalische Gesellschaft, Berlin (Germany).

- 2005-07-04:
  S. Krause, L. Berbil-Bautista, M. Bode, and R. Wiesendanger, *Spin-Polarized STM Through an Adsorbate Layer: Sulfur-Covered Fe/W(110)*, 13th International Conference on STM, Sapporo (Japan).

- 2006-03-30:
  S. Krause, L. Berbil-Bautista, M. Bode, and R. Wiesendanger, *Thermal Switching Behavior of Superparamagnetic Nanoislands: SP-STM on Fe/W(110)*, 70th Spring Conference, Deutsche Physikalische Gesellschaft, Dresden (Germany).

- 2006-08-02:
  S. Krause, L. Berbil-Bautista, M. Bode, and R. Wiesendanger, *Thermal Switching Behavior of Superparamagnetic Nanoislands: SP-STM on Fe/W(110)*, International Conference on Nanoscience and Technology, Basel (Switzerland).

- 2007-03-29:
  S. Krause, L. Berbil-Bautista, G. Herzog, M. Bode, and R. Wiesendanger, *Current-induced Magnetization Switching – a Possible Application for SP-STM?*, 71st Spring Conference, Deutsche Physikalische Gesellschaft, Regensburg (Germany).

- 2007-07-03:
  S. Krause, L. Berbil-Bautista, G. Herzog, M. Bode, and R. Wiesendanger, *Current-induced Magnetization Switching – is it Possible with SP-STM?*, International Conference on Nanoscience and Technology, Stockholm (Sweden).

- 2008-02-27:
  S. Krause, G. Herzog, M. Bode, and R. Wiesendanger, *Current-induced Magnetization Switching of Thermally Stable Nanoislands*, 72nd Spring Conference, Deutsche Physikalische Gesellschaft, Berlin (Germany)

- 2008-07-23:
  S. Krause, G. Herzog, M. Bode, and R. Wiesendanger, *Current-induced Magnetization Switching of Thermally Stable Nanoislands Using SP-STM*, International Conference on Nanoscience and Technology, Keystone, Colorado (USA).

Posters

- 2006-07-25:
  S. Krause, L. Berbil-Bautista, M. Bode, and R. Wiesendanger, *Thermal Switching Behavior of Superparamagnetic Nanoislands: SP-STM on Fe/W(110)*, 4$^{\text{th}}$ International Conference on Scanning Probe Spectroscopy (SPSt06) and 1$^{\text{st}}$ International Workshop on Spin-Polarized Scanning Tunneling Microscopy (SPSTM-1), Hamburg (Germany).

- 2007-01-04:
  S. Krause, L. Berbil-Bautista, M. Bode, and R. Wiesendanger, *Thickness-dependent Domain Structure of Ferromagnetic Dy(0001)/W(110) Studied by Spin-polarized STM*, 381$^{\text{st}}$ WE-Heraeus-Seminar "Spin-Polarized Currents in Magnetic Nanostructures", Bad Honnef (Germany).

Acknowledgements

I would like to take the opportunity to show recognition and appreciation to all the people who helped me in one way or another during the last years. In particular I would like to acknowledge the following people: